

RUPRECHT-KARLS-UNIVERSITÄT HEIDELBERG  
FAKULTÄT FÜR PHYSIK UND ASTRONOMIE  
MAX-PLANCK-INSTITUT FÜR KERNPHYSIK

# Ultra-Low Background Germanium Spectroscopy

Commissioning an experimental shielding for a future neutrino  
experiment

MASTER THESIS

**VERFASSER**  
**KONTAKT**

TOBIAS SCHIERHUBER  
HEINRICH-FUCHS-STRASSE 24  
69126 HEIDELBERG  
tobias.schierhuber@gmail.com

**MATRIKELNUMMER**  
**STUDIENGANG**  
**BETREUER**  
**DATUM DER ABGABE**

3032100  
MASTER (PHYSICS)  
PROF. DR. DR. h.c. MANFRED LINDER  
1. September 2017



## **Abstract**

This work was carried out during the assembly phase of the **CO**herent elastic **N**eutrino **nU**cleus **S**cattering (CONUS) experiment which is trying to detect the coherent elastic neutrino nucleus scattering process with a nuclear power plant as neutrino source. The experimental set-up has been initially tested in an underground laboratory at the Max-Planck-Institute for Nuclear Physics (MPIK) in Heidelberg. The goal for this thesis was the assembly and tuning of its muon-veto system as well as a general test of its shielding as a whole. Therefore the data acquisition unit has been set-up and measurements were carried out with a germanium detector to quantify the obtained energy spectra and veto efficiencies. With the testing phase almost completed, the CONUS experiment will start its detection process within 2017.

## **Zusammenfassung**

Diese Arbeit wurde während der Aufbau- und Testphase des **CO**herent elastic **N**eutrino **nU**cleus **S**cattering (CONUS) Experiments durchgeführt, dessen Ziel die Detektion kohärenter elastischer Neutrino-Kern Streuung ist. Der Aufbau dieses Experiments wurde zunächst im Untergrundlabor des Max-Planck Instituts für Kernphysik in Heidelberg getestet. Das Ziel der vorliegenden Arbeit sind Aufbau und Einstellung des benötigten Myonenveto-Systems sowie ein allgemeiner Test der Abschirmung, welche im CONUS Experiment Anwendung findet. In diesem Zusammenhang wurde ein System zur Datenerfassung eingerichtet und Messungen mit einem Germanium Testdetektor durchgeführt, um die gemessenen Energie Spektren sowie Myonenveto Effizienzen zu quantifizieren. Die Testphase des Experimentes ist fast abgeschlossen, sodass noch 2017 mit den Messungen zur Detektion von kohärenter elastischer Neutrino-Kern Streuung begonnen wird.

## **Acknowledgements**

I would like to thank my supervisor Manfred Lindner for the opportunity to contribute to the CONUS experiment as well as my co-supervisor Werner Maneschg. Furthermore I would like to thank Janina Hakenmüller, Herbert Strecker, Gerd Heusser and Reinhard Hofacker for help during the working phases of the thesis. Additionally I am grateful for the proof-reading of Janina Hakenmüller, Werner Maneschg, Karsten Mosny, Julia Ollesch, Moritz Platscher, Thomas Rink and Sebastian Thielen. And finally I would like to thank my mother and sister for their support over the entire time of my studies.

# Contents

|          |                                                        |           |
|----------|--------------------------------------------------------|-----------|
| <b>1</b> | <b>Introduction</b>                                    | <b>1</b>  |
| 1.1      | Low Background Gamma-Ray Spectroscopy . . . . .        | 2         |
| 1.1.1    | Detector Types . . . . .                               | 3         |
| 1.2      | Cosmic Radiation in Gamma-Ray Spectroscopy . . . . .   | 7         |
| 1.2.1    | Rejection of Cosmogenic Background . . . . .           | 7         |
| 1.2.2    | The GIOVE Setup . . . . .                              | 9         |
| <b>2</b> | <b>The CONUS Experiment</b>                            | <b>11</b> |
| 2.1      | Coherent Elastic Neutrino Nucleus Scattering . . . . . | 11        |
| 2.2      | Experimental Set-up . . . . .                          | 15        |
| 2.2.1    | Nuclear Power Plant . . . . .                          | 15        |
| 2.2.2    | CONUS Detectors . . . . .                              | 17        |
| 2.2.3    | CONUS Shielding . . . . .                              | 18        |
| 2.3      | Data Acquisition . . . . .                             | 20        |
| 2.3.1    | Web Interface . . . . .                                | 21        |
| 2.3.2    | Lynx SDK . . . . .                                     | 22        |
| 2.3.3    | Timed Listmode (TLIST) . . . . .                       | 22        |
| 2.3.4    | Synchronization . . . . .                              | 23        |
| <b>3</b> | <b>Muonveto System for CONUS</b>                       | <b>25</b> |
| 3.1      | Scintillator Plates . . . . .                          | 25        |
| 3.2      | Photomultiplier Tubes . . . . .                        | 26        |
| 3.3      | Background . . . . .                                   | 27        |
| 3.4      | Commissioning of the Muonveto system . . . . .         | 27        |
| 3.4.1    | Thresholds . . . . .                                   | 31        |
| 3.4.2    | Window Length . . . . .                                | 32        |
| 3.4.3    | Resulting Efficiency . . . . .                         | 32        |
| 3.5      | Dynamic Muonveto - DMV . . . . .                       | 34        |
| 3.5.1    | Pulse Form Analysis . . . . .                          | 36        |
| 3.5.2    | Energy Spectrum Analysis . . . . .                     | 38        |
| 3.6      | Results . . . . .                                      | 40        |
| <b>4</b> | <b>Commissioning of the CONUS Shield</b>               | <b>43</b> |
| 4.1      | CONRAD . . . . .                                       | 44        |
| 4.1.1    | High Voltage - Scan . . . . .                          | 44        |
| 4.1.2    | Active Volume . . . . .                                | 47        |
| 4.2      | Phase 1 . . . . .                                      | 50        |
| 4.2.1    | Goals . . . . .                                        | 50        |
| 4.2.2    | Measurement . . . . .                                  | 52        |

|          |                                                  |           |
|----------|--------------------------------------------------|-----------|
| 4.2.3    | Spectral Analysis . . . . .                      | 53        |
| 4.2.4    | Comparison with GIOVE . . . . .                  | 56        |
| 4.2.5    | Results . . . . .                                | 57        |
| 4.3      | Phase 2 . . . . .                                | 58        |
| 4.3.1    | Goals and Changes . . . . .                      | 58        |
| 4.3.2    | Measurements . . . . .                           | 59        |
| 4.3.3    | Spectral Analysis . . . . .                      | 60        |
| 4.3.4    | Results and Comparison with Phase 1 . . . . .    | 63        |
| <b>5</b> | <b>Conclusion and Outlook</b>                    | <b>65</b> |
| 5.1      | Muonveto System . . . . .                        | 65        |
| 5.2      | Commissioning of the CONUS Shield . . . . .      | 66        |
| 5.3      | Future of CONUS and Potential of CENNS . . . . . | 68        |
|          | <b>Bibliography</b>                              | <b>72</b> |
|          | <b>A Scintillator Plates</b>                     | <b>79</b> |
|          | <b>B Myonveto System for CONUS</b>               | <b>81</b> |
| B.1      | Thresholds . . . . .                             | 81        |
|          | <b>C Commissioning of the CONUS Shield</b>       | <b>85</b> |
| C.1      | HV - Scan . . . . .                              | 85        |
| C.2      | Phase 1 and 2 . . . . .                          | 86        |
|          | <b>D Lynx</b>                                    | <b>89</b> |
| D.1      | Stability Analysis . . . . .                     | 90        |
| D.2      | SDK Guide . . . . .                              | 91        |

# 1 Introduction

Today neutrinos are considered as one of the most important probes for the current standard model of particle physics and investigating their properties became a very active research field. They were postulated by Wolfgang Pauli more than 90 years ago, to maintain energy conservation in  $\beta$ -decays [1] and since its first detection in 1956 [2], several important discoveries have been made. One of them being the massiveness of neutrinos, which was discovered with the detection of neutrino oscillations [3, 4, 5]. The fact that neutrinos have a mass is not incorporated in the standard model of particle physics (SM) and is hence directly related to new physics beyond the standard model (BSM). Besides that there are still several unanswered questions about neutrino properties, which are currently under investigation. For instance experiments like: GERDA [6], MAJORANA [7], KamLAND-Zen [8] and EXO-200 [9] are trying to establish, whether neutrinos are Dirac or Majorana fermions by searching for neutrinoless double  $\beta$ -decay ( $0\nu\beta\beta$ ) a process which is only measurable if neutrinos are their own anti-particle and hence described by Majorana fermions. Further  $\beta$ -decay experiments like KATRIN [10], aim to accurately measure the neutrino's absolute mass, which is still unknown, since neutrino oscillations are only sensitive to their mass-squared difference. Their properties are not only relevant for small scale scattering processes regarding leptons and quarks, but also affect large scale properties like cosmological structure formation or the cosmological microwave and neutrino background. This underlines the significant role neutrino physics play in BSM investigations and why it gained more and more attraction in the last decades.

One important neutrino reaction channel, which attracted more and more attention in the last years is coherent neutrino nucleus scattering ( $\text{CE}\nu\text{NS}$ ). Although this interaction exhibits a large cross-section compared to other neutrino reaction channels, its detection requires advanced detector technologies and background suppression techniques. This originates from the very small momentum transfer and the corresponding small nuclear recoil, which is generally hard to detect in the energy region of interest. Only with the recent developments in detector design and manufacturing, these low energies can be measured. The detection of  $\text{CE}\nu\text{NS}$  is of special interest since it can not only be another confirmation of the standard model, but also provides another window for new BSM investigations. In precision measurements any deviation from the measured signal can be analysed in terms of new phenomena like non-standard neutrino interactions. Additionally, understanding and measuring  $\text{CE}\nu\text{NS}$  will provide information concerning processes inside supernovae (SN) which was also one of the first times  $\text{CE}\nu\text{NS}$  has been discussed [11]. This is of special importance as a core-collapse supernova emits 99 % of its gravitational binding energy in neutrinos of all flavours [12].

In August 2017, the COHERENT collaboration was able to observe  $\text{CE}\nu\text{NS}$  for the first time since its postulation in the 1970s [13] with a neutrino beam. This means exciting times lie ahead of us, with exploring a new window for BSM investigations and a rising number of experiments try to measure it with different technologies e.g. TEXONO [14], N $\nu$ GENT [15] and CONUS.

The COherent elastic Neutrino nUcleus Scattering (CONUS) experiment is a new experiment, which is utilizing germanium detectors to observe  $\text{CE}\nu\text{NS}$  with reactor neutrinos. Even though it has been detected by COHERENT, reactor-site experiments offer several advantages over the spallation experiments, like only having one neutrino flavor ( $\bar{\nu}_e$ ) present and having neutrino energies below 8 MeV, which means the neutrinos interact purely coherently. This is an amazing step for neutrino physics, since previous experiments which aim in neutrino detection, required a much higher mass (ton scale) where experiments measuring  $\text{CE}\nu\text{NS}$  use only kg sized devices to detect neutrinos.

This work was carried out in the scope of this experiment and is structured as follows. The rest of this chapter gives some basic information about low background gamma-ray spectroscopy as well as cosmic radiation and the second chapter introduces the CONUS experiment. One core aspect of this work is the commissioning and tuning of the muonveto system for the CONUS shield as well as trying to implement a further upgrade, which will be presented in chapter 3. Afterwards chapter 4 deals with the commissioning and characterization of the CONUS shield as a whole. During all steps software for starting and saving necessary measurements as well as for data analysis was developed, which is explained in the corresponding chapters. Due to the extensive work done with the Lynx, a small guide for writing a script controlling the Lynx is presented in Appendix D.2. This thesis concludes with a discussion of the results and an outlook om future experimental possibilities.

## 1.1 Low Background Gamma-Ray Spectroscopy

In many areas, gamma-ray spectroscopy is a very useful tool for energy spectra analysis. This is used in a variety of fields and is not limited to physical experiments, for instance it finds applications in geology or industry as well. Low background gamma-ray spectroscopy is an excellent method for material screening since it can detect faint traces of radioactive impurities. This in turn is important, because many low background experiments require a thorough material screening to keep background levels as low as possible. Furthermore, it is a widely applied tool for rare event physics experiments, for example neutrino experiments as well as dark matter searches [16, 17].



One problem, which has to be dealt with and which is key to this thesis, is the background for such experiments. There are many different origins of this unwanted radiation like:

- environmental radioactivity,
- radioimpurities in detector and shield material,
- radon (Rn) and its progenies,
- cosmic rays,
- neutrons from natural fission and neutron transfer reactions.

To exclude background events for such experiments, the detectors have to be shielded in various ways to minimize the influence from the sources mentioned above. This has to be kept in mind when designing an experiment and its shielding concept has to account for all possible background components.

### 1.1.1 Detector Types

At the heart of a radiation detector is the detector material, which has to enable an interaction with incoming (particle) radiation. This interaction must then result in an emission of electric charge, which can be collected and transformed into an electric signal [18]. It is usually characterized via its cross section  $\sigma$ , which depends on the material used,

$$\sigma = \frac{N_s}{F}. \quad (1.1)$$

With the simple version of the total cross section in (1.1), where  $F$  is the particle flux and  $N_s$  the number of measured particles, the interaction of radiation with a detector can be described [19]. In the following, two types of detector types shall be introduced briefly since both are important in the context of this thesis. For more details about detectors see [18] as well as [20].

#### Scintillation Detectors

The scintillation method to detect ionizing radiation is a well known and widely spread technique in nuclear and particle physics. It utilizes the ability of materials to emit light when interacting with radiation. These scintillation materials vary in their characteristics, which means that the detector material has to be chosen according to the desired application: while some materials have a very linear and high light output, they may have a slow response time [18, 20]. The energy deposited inside a scintillator can be described by the Bethe-Bloch formula [20]

$$-\frac{dE}{dx} = 2\pi N_a r_e^2 m_e c^2 \rho \cdot \frac{Z}{A} \frac{z^2}{\beta^2} \left[ \ln\left(\frac{2m_e \gamma^2 v^2 T_{max}}{I^2}\right) - 2\beta^2 \right]. \quad (1.2)$$

The deposited energy then results in a light emission process which can be described via an exponential function that has two components: A fast and slow (or prompt and delayed) one

$$N_0 = A \cdot \exp\left(\frac{-t}{\tau_f}\right) + B \cdot \exp\left(\frac{-t}{\tau_s}\right), \quad (1.3)$$

where the  $\tau$  represents the respective decay constant, and their magnitudes  $A$  and  $B$  depend on the material. These two components arise, when analysing the pulse form of the scintillation signal, one finds faster and slower component this is shown in figure 1.1.

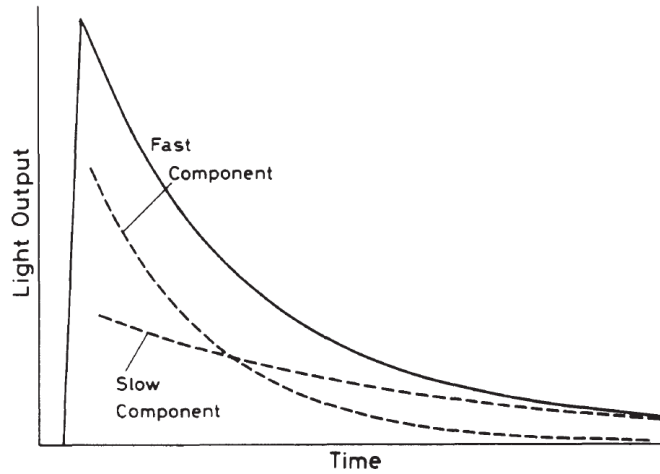


**Figure 1.1:** Analysis the light output of a scintillator in two components: fast and slow [20].

The two main groups of scintillator materials are: organic and inorganic. One widely spread type of organic scintillator is made out of plastic. They are very cheap in production and are therefore a good choice if large volume scintillation is needed. Furthermore, they offer a good and linear light output as well as fast response time. The photon rate can be described via:

$$N(t) = N_0 \cdot \mathcal{F}(\sigma, t) \cdot \exp\left(\frac{-t}{\tau}\right), \quad (1.4)$$

which is derived from (1.3), with  $\mathcal{F}(\sigma, t)$  being a Gaussian, depending on the specific plastic used. For building such a detector, further hardware is required, since the scintillation material only emits light as response to incoming radiation. This emitted light then has to be evaluated. Usually some kind of photomultiplier tube is used. A basic example for such a detector is shown in figure 1.2.

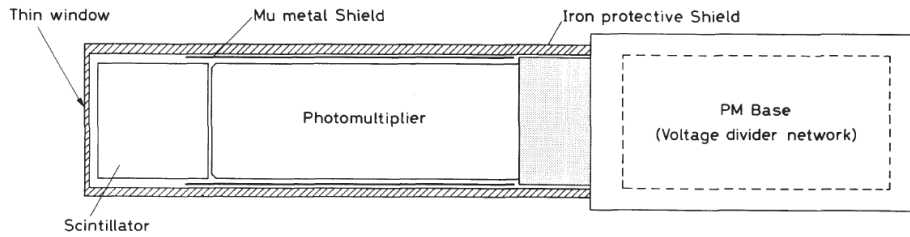


**Figure 1.2:** A basic scintillator set-up [20].

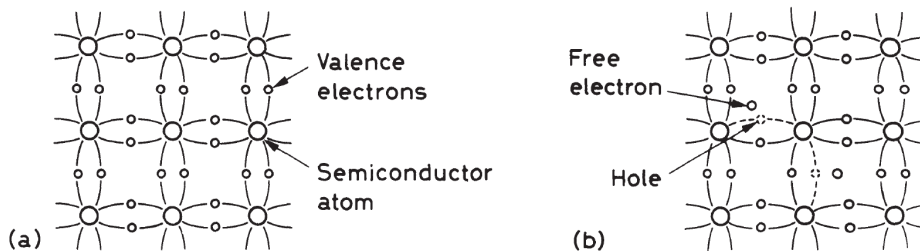


**Figure 1.3:** Left: The covalent bonding of silicon/germanium at 0 K, where all electrons are bound.

Right: Above 0 K holes arise in the valence band [20].

## Semiconductor Detectors

A semiconductor detector's good energy resolution is advantageous in many applications. Incoming radiation creates electron-hole pairs, which can be collected by an applied electric field. The required energy to create such a pair is much lower compared to other detectors, which is why semiconductor detectors have a superior resolution.

As shown in figure 1.3, at temperatures above 0 K holes arise inside the crystal, which results in a so-called leakage current. To prevent this current, semiconductor detectors have to be cooled because with decreasing temperature more electrons participate in the covalent bonding and close existing holes in the lattice. Due to their importance for this thesis germanium detectors are discussed in more detail. Germanium detectors need a high depletion depth, which describes the size of the depletion zone. The depletion zone is that volume of the crystal, from which free charges are collected from an applied electric field (later referred to as active volume). There are two strategies to ensure this: either the impurities<sup>1</sup> of the germanium have to be reduced or another material is introduced which balances the impurities with dopant atoms of the opposite type is required. An example for the latter are Ge(Li) detectors, where lithium is introduced into the germanium. The lithium introduces an ion drift, which counteracts the drift of impurities of

<sup>1</sup>Germanium impurities refers to any non germanium atoms inside a germanium crystal.

the germanium. The disadvantage of these kind of detectors is that they have to be cooled (usually with liquid nitrogen) all the time to prevent permanent damage to the detector.

Many improvements in producing very pure germanium have been made. These high purity germanium detectors (HPGe) became the standard germanium detectors for spectroscopy due to Ge(Li) detectors having to be cooled even when they are not being operated, which decreases their practicality. The production of these very pure germanium detectors requires a method called zone refining, which involves repeated melting and solidifying phases [19]. Once the HPGe is created, a variety of designs are possible. The used design depends on the application at hand; two examples are shown in figure 1.4. The left example has the advantage of a higher possible mass (up to 3 kg), whereas the right design can offer a better energy resolution. One reason is the size of the read out electrode, which is much smaller for the point contact design.

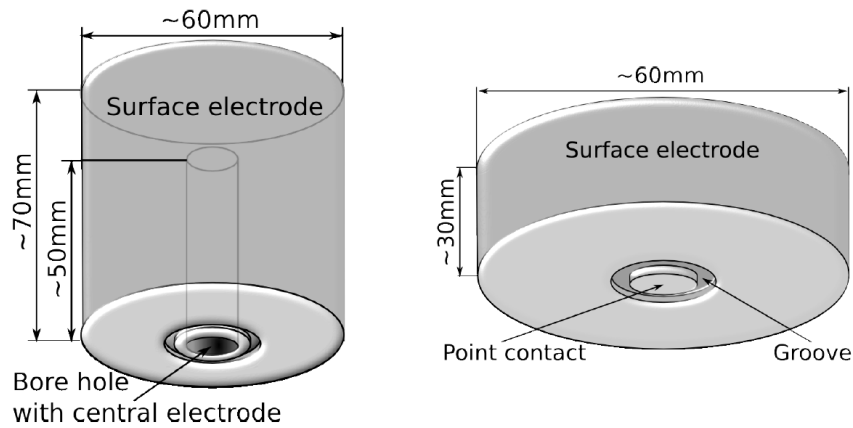


**Figure 1.4:** Left: An example for a semi-coaxial detector design.  
Right: An example for a point contact detector design [19].

## Quenching

One aspect of detectors is the so called quenching. This describes the fact that there is an energy loss between the recoil energy and the energy which is finally detected. This energy loss occurs in multi-particle interactions occurring during the charge transport from the interaction point to the read-out electrode. The Lindhrad theory describes this energy loss semi-empirically [21]. The exact amount of energy loss depends on various facts and cannot be determined analytically but only be simulated or measured. This makes detecting events with low recoil even harder.

## 1.2 Cosmic Radiation in Gamma-Ray Spectroscopy

Cosmic radiation is interacting with the earth's atmosphere, where secondary particle showers are created and travel towards the surface. These particle showers include: protons, neutrons, electrons, pions and muons. On their way, the amount of pions and protons is reduced by at least two orders of magnitudes compared to other particles like muons, neutrons and electrons. One important component of this reduction is regular decay via weak interactions, which create additional muons

$$\begin{aligned}\pi^+ &\rightarrow \mu^+ + \nu_\mu \\ \pi^- &\rightarrow \mu^- + \bar{\nu}_\mu.\end{aligned}\tag{1.5}$$

### 1.2.1 Rejection of Cosmogenic Background

To combat the background induced by the cosmic radiation, multiple steps are necessary. As previously mentioned, some of the incoming radiation is already suppressed by a trajectory through the Earth's atmosphere. Then detectors require a shielding which prevents further interactions of the cosmic radiation with the detector. Electrons and neutrons can be absorbed by introducing an overburden, meaning locating the experiment underground rather than on the Earth's surface. This overburden is usually compared to water, so the thickness is given in meters of water equivalent (w.e.). An appropriate overburden level of 50 m w.e. can provide a good shielding, since some cosmic components (mainly photons, protons and electrons) are absorbed by it. This is why almost all neutrino and dark matter experiments are underground. By shielding the detector with lead, the mentioned particles can be shielded even more effectively. Due to their high penetration depth given by figure 1.5, neutrons and muons require further shielding mechanisms. To shield effectively against neutrons an absorber material with a high neutron-capture cross section, like borated polyethylene or xenon is required. Because incoming muons can create additional neutrons via muon-capture of protons,

$$\mu^- + p \rightarrow n + \nu_\mu,\tag{1.6}$$

the neutron absorber material should be in between gamma radiation shield layers (e.g. lead) to effectively shield against these neutrons. If the shielding acquired by a neutron absorber is not sufficient, an active veto system that can detect neutrons is required [18].

The last component left, are muons. These particles are created via (1.5),(??). The reduction rate of muons with increasing depth is rather weak, compared to the previous mentioned background components. Therefore these particles can only be effectively shielded by having an overburden well beyond 1000 m w.e. or by utilizing an active veto system. These system are able to detect incoming muons (e.g. scintillator) and are used in anti-coincidence with the detector to not record the muon-induced events. An example of such a veto system will be described in more detail in chapter 3.

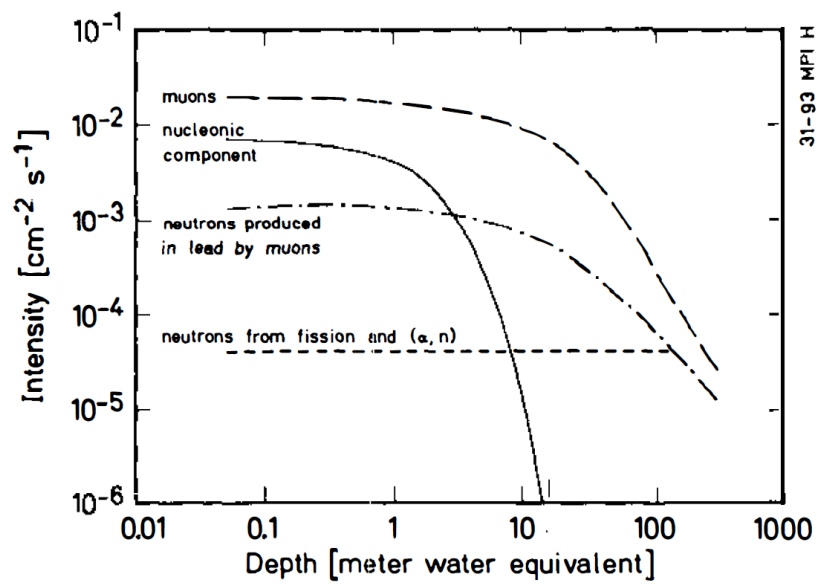


Figure 1.5: Reduction of cosmic radiation components in dependence of the penetration depth [17].

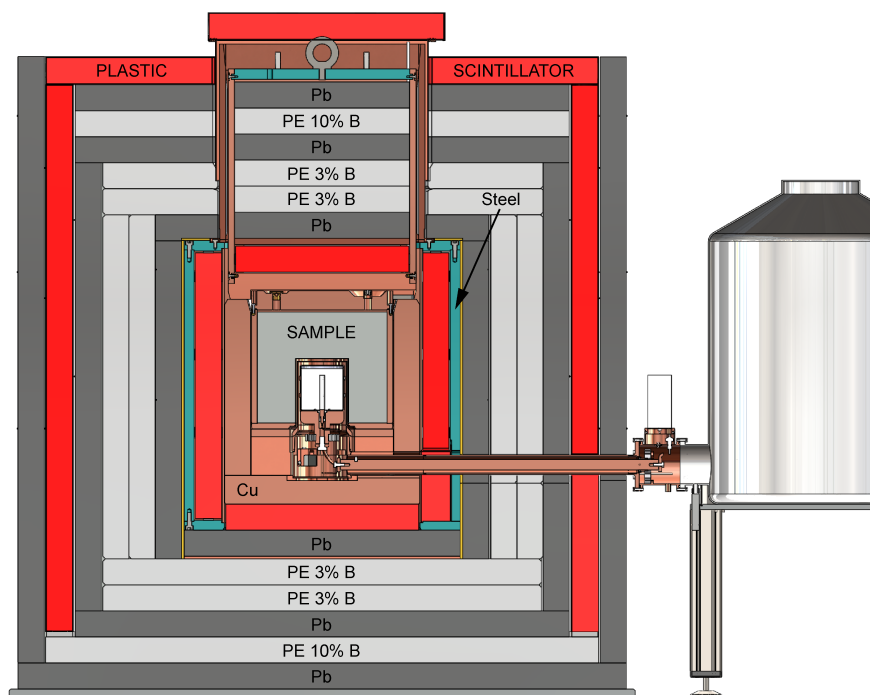
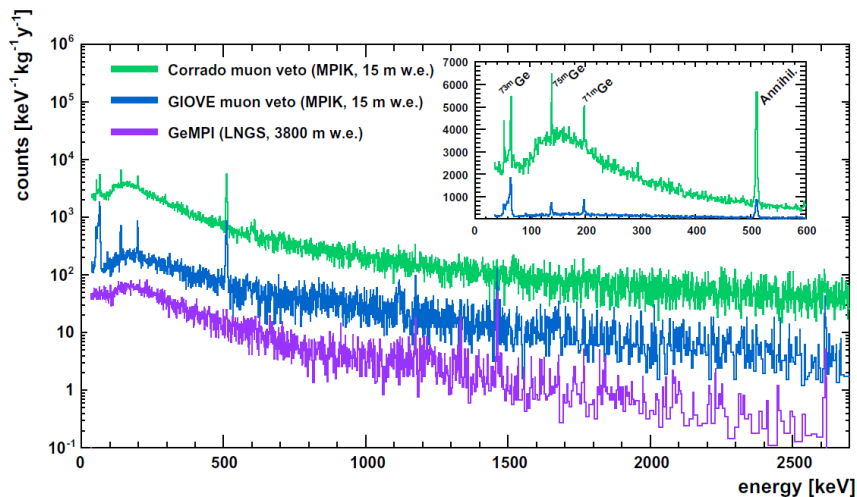


Figure 1.6: Shielding layers of the GIOVE set-up for material screening [17].

## 1.2.2 The GIOVE Setup

The GIOVE setup for material screening was developed at the MPIK Heidelberg by Gerd Heusser and is one of the first detectors which achieved a very high background suppression of cosmic radiation with a physical overhead of only  $\mathcal{O}(15 \text{ m})$  water equivalent. Through a very smart shielding concept, which utilizes all mentioned shielding options mentioned above, a virtual depth of several hundred meter w.e. could be achieved. To effectively shield against all outer influences, GIOVE uses multiple layers of lead, borated polyethylene plates, as well as a muonveto system utilizing plastic scintillator plates. Its onion-like shielding configuration is shown in figure 1.6. The used detector, is a coaxial high-purity Ge detector with an active mass of  $m_{\text{mactive}} = (1.8 \pm 0.1) \text{ kg}$ . The used muonveto system has an efficiency of  $\sim 99\%$  and a resulting deadtime of  $\sim 2\%$ .

Figure 1.7 compares the achieved background levels with two other set-ups. Mainly with the GeMPI measurement, which was done at the Laboratori Nazionali del Gran Sasso (LNGS). The experiment has an overhead of 3800 m w.e. and only a passive shielding. Through utilizing a muonveto system, the GIOVE set-up can achieve a suppression comparable to an overhead of several 100 m w.e.

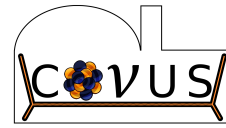


**Figure 1.7:** Comparison of GIOVE background energy spectra with two other detectors [17].





## 2 The CONUS Experiment



The goal for the CONUS experiment is the measurement of the **CO**herent elastic **N**eutrino **nU**cleus **S**cattering ( $CE\nu NS$ ). It was developed at the Max-Planck-Institute for Nuclear Physics (MPIK) in Heidelberg. The scientific team members of the CONUS experiment as of August 2017 are:

Christian Buck, Janina Hakemüller, Gerd Heusser, Reinhard Hofacker, Manfred Lindner, Werner Maneschg, Thomas Rink, Herbert Strecker, Tobias Schierhuber and Victoria Wagner from the **Max-Planck-Institut für Kernphysik, Heidelberg**

Kai Fülber and Roland Wink from **Preussen Elektra GmbH, Kernkraftwerk Brokdorf**

as well as Steffen Form, Benjamin Gramlich, Michael Reißfelder, Arnold Schwarz, Jonas Westerman from the **engineering and service team of the division Lindner at MPIK in Heidelberg!**

This chapter will give a brief introduction to the experiment and is based on the TAUP 2017 talk by Janina Hakenmüller [22], the Scientific Advisory Board 2017 talk by Thomas Rink [23], the presentation held by Werner Maneschg at the "The Future of Neutrino Physics" workshop [24] as well as the talk held by Manfred Lindner at the Strategie-Meeting of the Komitee für Astro.Teilchen.Physik (KAT), November 2016 [25]. For a more detailed explanation and introduction into this experiment see Lindner et al [26].

### 2.1 Coherent Elastic Neutrino Nucleus Scattering

Coherent elastic neutrino nucleus scattering is a weak natural current interaction (Z boson exchange), which was predicted by Freedman in 1974 [12] and was recently detected by COHERENT [13]. The detection of this last neutrino reaction channel was another confirmation of the standard model of particle physics. The special property of  $CE\nu NS$  is the coherent enhancement since the neutrino wave packet covers the whole target nucleus.

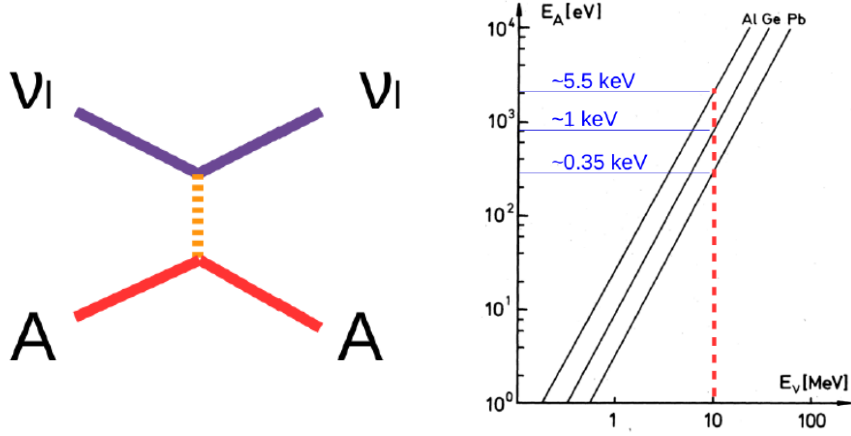


**Figure 2.1:** Left: The Feynman diagram for the coherent elastic neutrino nucleus scattering.

Right: Expected nuclear recoil energy for CE $\nu$ NS at a neutrino energy of 10 MeV for different target materials [27].

The interaction cross section in the standard model is given by [22]

$$\frac{d\sigma}{d\Omega}(E_\nu) = \frac{G_F^2}{16\pi^2} \cdot Q_W^2 \cdot E_\nu^2 \cdot (1 + \cos(\theta_W)) \cdot F^2(Q^2). \quad (2.1)$$

$$Q_W = N - Z \cdot (1 - 4 \cdot \sin^2(\theta_W)) \quad (2.2)$$

$$G_F = 1.1663786(6) \times 10^{-5} \frac{1}{GeV} \quad (2.3)$$

with Weinberg angle  $\theta_W$ , the neutron number  $N$ , as well as the weak charge of the nucleus  $Q_W$  (2.2) and the Fermi constant for 4-point interactions  $G_F$  (2.3). By doing a coordinate transformation from the solid angle  $\Omega$  to the nuclear recoil energy  $T$ , the cross section can be described the following way

$$d\Omega = d\phi \cdot d\cos(\theta) \quad (2.4)$$

$$\cos(\theta) = \frac{E_\nu + m_N}{E_\nu} \sqrt{\frac{T}{T + m_N}} \quad (2.5)$$

$$\frac{d\sigma}{dT}(T, E_\nu) \cong \frac{G_F^2}{8\pi} [Z \cdot (1 - 4 \cdot \sin^2(\theta_W)) - N]^2 \cdot \left[1 - \frac{T}{4E_\nu^2}\right] \cdot F^2(T), \quad (2.6)$$

where  $F$  is the nuclear form factor, which describes the difference to scattering off a point-like object. This correlation is shown in figure 2.2. For low-energy (<30 MeV) neutrinos, the nucleus to scatter on appears to be a point-like object since the corresponding momentum transfer is small; hence  $F$  can be approximated with unity. A rate can be calculate by integrating the cross section (2.1):

$$S = N \cdot \phi \cdot \int_{T_{threshold}}^{T_{MAX}} \frac{d\sigma}{dT} \cdot dT \quad (2.7)$$

where  $N$  is the number of targets and  $\phi$  is the particle flux.

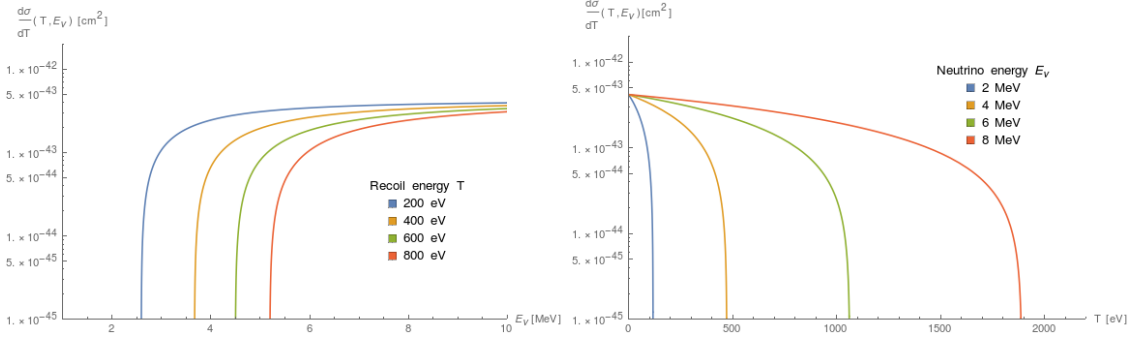


**Figure 2.2:** Left: The relation of the neutrino energy  $E_\nu$  and the differential cross section  $\sigma$  at different recoil energies  $T$ .  
 Right: The relation of the differential cross section and the recoil energy  $T$  for different neutrino energies ( Figure made by T. Rink)

Further, from equation (2.1) or (2.6) we can infer that the total cross section is proportional to the nucleus' neutron number (since  $\sin^2(\theta_W) \approx 0.24$  ).

$$\sigma \propto N^2 \quad (2.8)$$

From equation (2.5), one can deduce an expression for the maximal nuclear recoil energy, by setting  $\cos(\theta) = 1$ :

$$T_{nuc}^{MAX} = \frac{2E_\nu^2}{m_p \cdot A + 2E_\nu} \approx \frac{2E_\nu^2}{m_p \cdot A}. \quad (2.9)$$

$$\Rightarrow T \propto \frac{1}{N + Z} \quad (2.10)$$

Thus, the nuclear recoil energy  $T_{nuc}$ , is inversely proportional to the total mass of the target (see equation (2.10)). This leads to a push-pull situation, since the only observable of CE $\nu$ NS is the nuclear recoil energy  $T_{nuc}$ . Therefore medium-size targets are the most favourable for CE $\nu$ NS, since a too high neutron number results in a low recoil energy; a low neutron number leads to a low cross section  $\sigma$ . On the right side of figure 2.1, an example for expected nuclear recoil energies for different targets at a certain neutrino energy is shown.

The important condition for CE $\nu$ NS is coherence. To be fully coherent, the de Broglie wave length  $\lambda_{dB}$  has to be larger than the radius of the nucleus  $R_A$ . With (2.11)-(2.13) one receives the maximal energy at which a coherent interaction/enhancement is possible

$$\lambda_{dB} \geq R_A \quad (2.11)$$

$$R_A \simeq 1.25 \cdot \sqrt[3]{A} \quad (2.12)$$

$$E_\nu \leq \frac{1}{2R_A} \approx \frac{197}{2.5 \cdot \sqrt[3]{A}} [\text{MeV}]. \quad (2.13)$$

Using equation (2.13), the maximal energy for coherent interactions on several target nuclei can be calculated.

|    | $A$   | $R_A$ [fm] | $E_{\nu coh}$ [MeV] |
|----|-------|------------|---------------------|
| Ar | 39.9  | 4.0        | <b>26</b>           |
| Ge | 72.6  | 5.2        | <b>19</b>           |
| Xe | 131.3 | 6.3        | <b>15</b>           |

**Table 2.1:** Table with the coherence condition for the neutrino energy of a selected target sample.

As seen in table 2.1, for an Argon target, incoming neutrinos need an energy below 26 MeV to be able to interact fully coherently with the nucleus. Partial coherence is still possible, but the form factors decrease rapidly and therefore the cross section [28].

**Experimental Challenges** Besides the detection of the nuclear recoils itself, there are a few factors which make detecting CE $\nu$ NS still difficult today, i.e. one has to know the background and the neutrino source very well. In general one can distinguish the experiments, which try to measure CE $\nu$ NS by their neutrino source. The main sources are:

- $\pi$ -DAR
- Nuclear power plants
- Natural radioactivity

The two most promising ones are  $\pi$ -decay at rest (DAR) and reactor neutrinos to detect CE $\nu$ NS [24] because of high fluxes and manageable systematics. With a  $\pi$ -DAR experiment (like COHERENT) CE $\nu$ NS was detected for the first time in August 2017 [13]. Each source faces its own difficulties and all systematics have to be very well understood to produce a valid result.

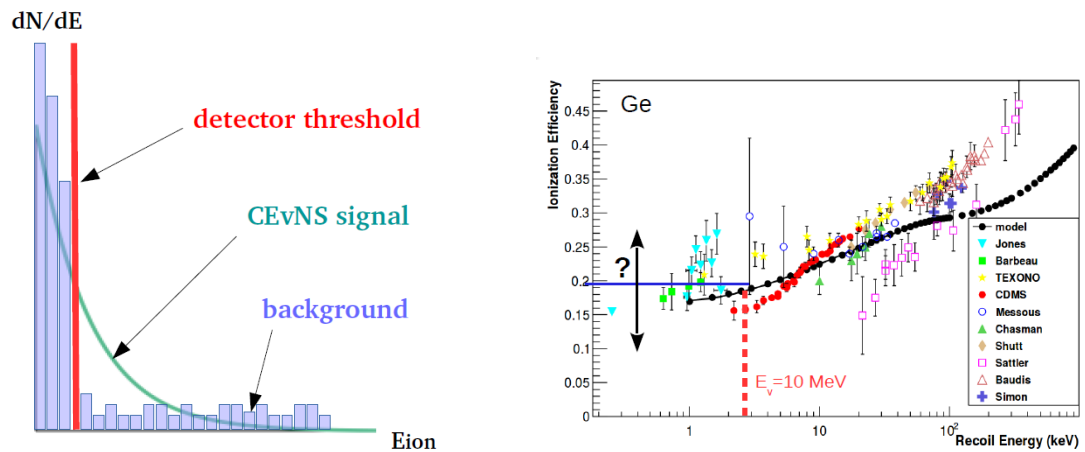


**Figure 2.3:** Left: Schematic description of a CE $\nu$ NS signal [22].

Right: Expected ratio of ionization energy vs. recoil energy for a Germanium detector [29].

One big problem is the energy loss within the detector through so called quenching (see section 1.1.1), which is one of biggest uncertainties in CE $\nu$ NS measurements. This work focuses on a reactor experiment, hence the challenges for this kind of experiment shall be briefly mentioned.

As described in section 1.1, a detector measures ionization energy which is related to the nuclear recoil energy of the struck nucleus. For Germanium detectors, there is an energy dissipation up to 80 % possible in detecting nuclear recoils. This means detectors need very low thresholds, in order to detect this low-energy interaction which is schematically shown on the left of figure 2.3. An example for germanium: an incoming 10 MeV neutrino creates a nuclear recoil energy  $E_{rec} = 2$  keV within the detector. By using a quenching factor of 0.2 (optimistic) the resulting ionisation signal  $E_{ion} = 400$  eV. The next important factor is the background, which also has to be very low in order to receive a good signal to noise ratio within a reasonable measuring time. Furthermore, a high neutrino flux is very beneficial, but usually comes at the cost of being located at the earth's surface. This is problematic since there is a lot of background on the surface as well, so the right balance has to be found.

## 2.2 Experimental Set-up

The previous section gave a brief introduction to the topic of CE $\nu$ NS and pointed out some problems with it as well. The CONUS experiment has to tackle three main issues in order of being able to detect CE $\nu$ NS, these will be covered in the following sections:

1. Neutrino Source
2. Low Energy Threshold
3. Background Suppression

### 2.2.1 Nuclear Power Plant

As neutrino source the commercial nuclear power plant in Brokdorf (Germany) was chosen. Reactor sites offer the highest neutrino flux on the earth, furthermore allows to build the experiment close to the reactor, shown in figure 2.5. It is owned and run by PreussenElektra GmbH and producing electricity since 1986. The annual electricity production of the pressurized water reactor is  $\sim 11$  billion kw/h [30]. It has a maximal thermal power output of 3.9 GW in its high duty cycle. During the experiments lifetime there will be reactor phases, where to reactor is refilled with fuel elements. This allows for a good background reduction, through a collection of background spectra. These are later subtracted from the energy spectra after an appropriate normalization. A calculation of the expected anti-neutrino spectrum is shown in figure 2.4.

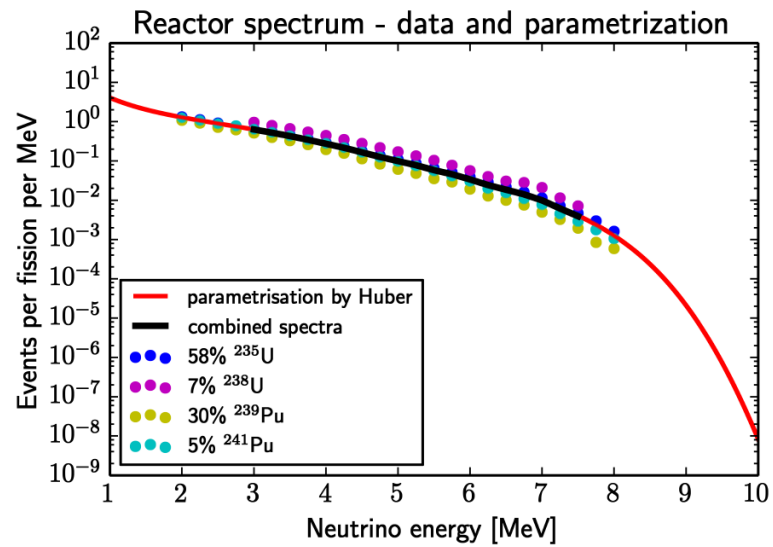


**Figure 2.4:** An expected anti-neutrino spectrum form a reactor source. The dots represent measured data and the line is a parametrization, from [31, 32].

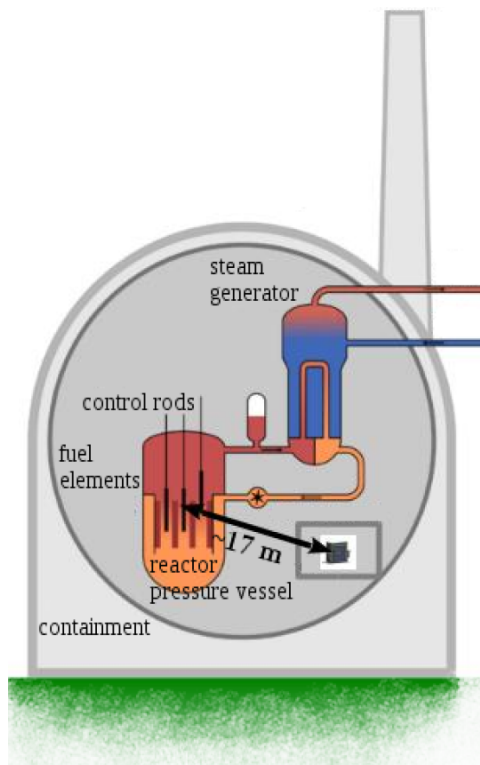


**Figure 2.5:** Left: Position for the CONUS experiment inside the nuclear power plant in Brokdorf [22]  
 Right: An outside view of the nuclear power plant owned by PreussenElektra GmbH [30].

At a distance from the reactor of  $\sim 17$  m (see left part of figure 2.5), the expected anti-neutrino flux is of  $\mathcal{O}(10^{13} s^{-1} \cdot cm^{-2})$ . With anti-neutrino energies up to 8 MeV we are in a purely coherent regime as shown in table 2.1. There are anti-neutrino with even higher energies, but they come with higher uncertainties since there are fewer events in the exponentially falling spectrum. The experiment is located inside the power plant in the containment area, which means in addition to high  $\bar{\nu}$  flux, there is an overburden of 10-45 m water equivalent [22], helping to reduce the cosmic radiation (described in section 1.2 of the introduction).

## 2.2.2 CONUS Detectors

The main attribute of the detectors used in the CONUS experiment, is a very low threshold. In preparation for the experiment, a feasibility study was performed to investigate the optimal figure of merit for CE $\nu$ NS detection. The used assumptions were:

- Background level:  $1 \frac{cts}{kg \cdot d \cdot keV}$  (typical background, reached by other experiments)
- $\bar{\nu}$ -flux:  $2.4 \cdot 10^{13} \frac{1}{s \cdot cm^2}$  (this corresponds to a 3 GW reactor at 15 m distance, neutrinos below 2 and above 8 MeV are neglected).

This study showed, that even with a detector mass of 1 kg, the experiment is capable of measuring a signal with satisfying accuracy.

| $E_{ion}^{Th}$ [keV] | qf=0.15 | qf=Lindhard | qf=0.2 | $(S/B)_{(qf = 0.15)}$ |
|----------------------|---------|-------------|--------|-----------------------|
| 0.30                 | 9       | 64          | 154    | 0.4                   |
| 0.24                 | 90      | 348         | 724    | 3.2                   |
| 0.18                 | 734     | 1654        | 3045   | 22                    |

**Table 2.2:** The results for the feasibility study performed by Lindner M., Maneschg W., Rink T., (2016); the signal rates are given in *cts/year*.

Using the above results, four high-purity point contact Ge detectors with a total target mass of  $\sim 4$  kg from the company CANBERRA are used for CONUS. To ensure the best possible results and in order to reduce the background as much as possible, all used internal parts for the detector were screened at the MPIK and the Laboratori Nazionali del Gran Sasso (LNGS). This ensures a minimal contamination due to radio impurities in the finished detectors. Additionally to the screening process, the detectors are and were stored underground during manufacturing, to avoid any activation from cosmic radiation. Due to the safety regulations inside the nuclear power plant, the detectors were fitted with a state-of-the-art cryo-cooling system, which has many upsides (e.g. controllable temperature, no refilling required) from common cooling with liquid nitrogen.

### 2.2.3 CONUS Shielding

The second important aspect for detecting the  $CE\nu NS$  signal, is a very good suppression of external backgrounds. Therefore the CONUS experiment uses a comprehensive shield, which has active as well as a passive components. The MPIK is experienced in developing effective shielding for shallow depths, which was already demonstrated in the GIOVE experiment (see section 1.2.2 for more details). With this knowledge the shield for the CONUS experiment was designed.

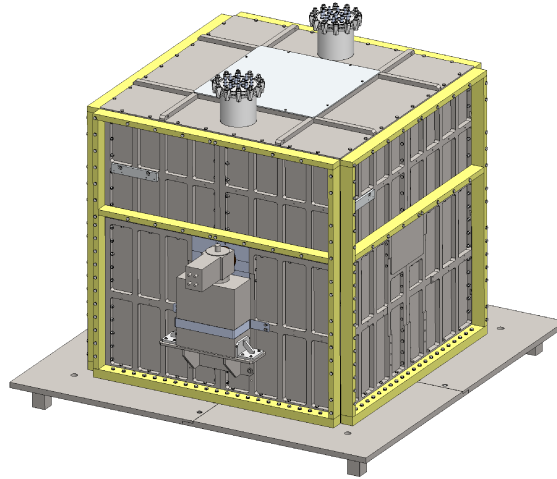


**Figure 2.6:** The outer shell of the CONUS experiment, designed at the MPIK. The Image was created by the construction department of the MPIK.

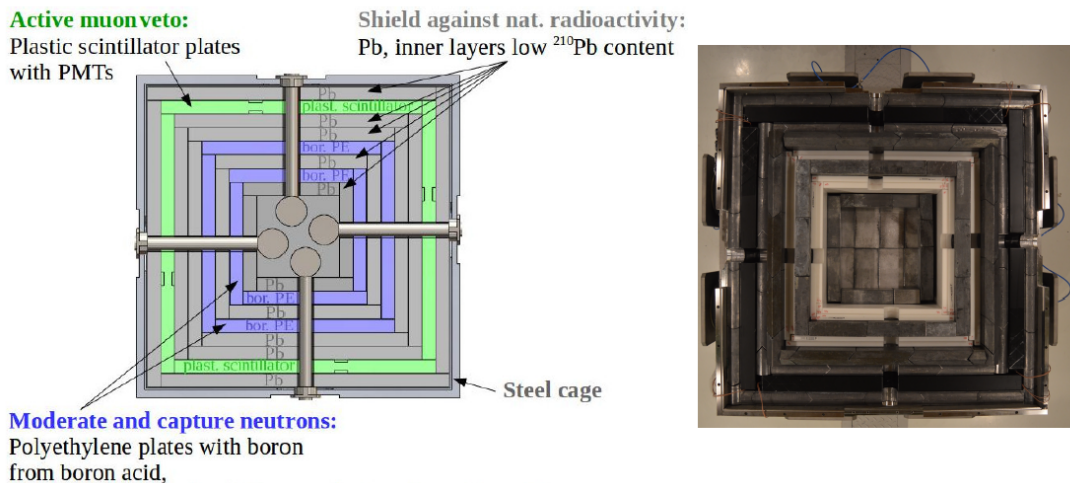


**Figure 2.7:** Left: The schematic view of the inner layers of the shield. Right: The same view onto the assembled shield in the low-level laboratory at MPIK in Heidelberg.



The whole experiment is located inside the commercial power plant described in 2.2.1, therefore it has to fulfil the safety regulations issued by German authorities. These state that the experimental set-up must not threaten the safety of the nuclear power plant. Furthermore, in case of an earthquake the CONUS shield has to stay intact and must not move within the room. These aspects in mind, the experiment shell was designed as given in Figure 2.6 which shows the construction drawing of the finished experiment, once it is assembled in Brokdorf<sup>1</sup>. The shell consists of a steel cage and encapsulates the inner layers of shielding materials. The shield has to deal with various aspects of underground components, which influence the resulting measurements. The actual radiation shield with its active and passive components is arranged in an onion-like structure inside the steel cage. One purpose of the steel cage, is to keep the structural integrity of the set-up intact in case of outside influence (e.g. an earthquake).

## Radon and airborne natural Radioactivity

The ambient air contains radon amongst other naturally decaying isotopes. To minimize the effect of Rn contamination, a second important function of the steel cage sealing the experimental set-up air tight. This means that once it is closed no more Rn can stream into the inner layers such that the contained Rn decays within a few days and the background starts reducing. This is important because inside the power plant N<sub>2</sub>-flushing the experiment is not possible due to safety regulations. The ambient radiation in the room itself is shielded by the lead.

## Cosmic Radiation and Neutrons

As described in section 1.2, the main components are neutrons and muons. Other components like electrons and protons can be shielded by having the experiment located underground and introducing an overburden of 10-45 m (w.e.). Moreover, they can be kept off effectively by introducing lead as shielding material. The neutrons still left from cosmic radiation, and the ones originating from the reactor itself can be counteracted by introducing boron-treated polyethylene plates (boron acid enriched in <sup>10</sup>B ≡ 3 % natural boron), which capture the neutrons (see section 1.2.1). Since the muons can penetrate all layers of lead and create new neutrons, two layers of polyethylene plates between the lead layers are introduced, which can be seen in figure 2.7. The previously listed components will be referred to as the passive components of the shield. The mentioned muons themselves have to be dealt with as well. Due to the low overhead of only 10-45 m, the rate of muons is only reduced slightly according to figure 1.5 and hence an active muonveto system is to be used. This system consists of nine scintillator plates which are located around the detectors, as shown in figure 2.7. More details about the muonveto system used for the CONUS experiment will be presented in chapter 3.

---

<sup>1</sup>For the initial construction a different cage system was used. This will only be used in the initial testing phase at the MPIK and the final version will use the version shown in figure 2.6.

## Radioimpurities in the used Materials

To avoid any contamination originating from impurities, all the used materials close to the detectors have been screened either at MPIK in Heidelberg, or the Laboratori Nazionali del Gran Sasso (LNGS). The lead, which is close to the detector, has to be very old, to be low on  $^{210}\text{Pb}$ , so it does not only suppress the bremsstrahlung continuum induced by muons (explained in detail in section 1.2), but also prevents inducing a continuum itself from its  $^{210}\text{Pb}$  content. All the previously mentioned aspects combined, result in a very solid suppression of any background components for the CONUS experiment.

## 2.3 Data Acquisition

A very important part of experiments is data acquisition. The main interest is, read-out, collection and transformation of the experimental data into a format, with which data analysis is possible. This usually means doing an analogue to digital conversion. The CONUS experiment uses low-background spectroscopy, hence this section will focus on the aspects important for it, rather than giving a very broad introduction to this extensive topic.

In the field of low-background gamma-ray spectroscopy, the data acquisition system has to perform more tasks than just transforming experimental data from an analogue to a digital format. The systems commonly used are not only able to transform the data into a variety of different formats but are able to do a pre-analysis as well. This means they can often start analysing the data while saving it. So the system can decide whether an event is physical or not. Another aspect is signal processing, so these systems are able to use different filters, amplifications and acquisition modes to accommodate a variety of experimental fields.

The CONUS experiment requires features (**bold** signifies high priority):

- **Pulse Reset amplifier signal**
- **Good energy resolution**
- **Anti-coincidence measurements**
- **Synchronization**
- Fast Sampling
- Pulse Shape Analysis

There were many possibilities for a DAQ system and the system which fulfilled most of the desired options is the Lynx DAQ from CANBERRA [33].

In the following, a few important aspects of the Lynx system will be presented. This system was developed by the company CANBERRA. It offers an easy plug & play solution. Furthermore it can accomplish a better energy resolution than most other comparable systems. The Lynx offers a variety of acquisition modes:

- PHA - Pulse Height Analysis
- MCS - Multi-Channel Spectrum
- TLIST - Timed List mode

In addition the Lynx system can measure data in 32768 channels with a sampling rate of up to 80 MHz. Initially the Lynx system was supposed to implement a pulse shape analysis interface, but this feature has not been implemented by CANBERRA so far. Another neat feature the Lynx offers, is a Digital Oscilloscope, which enables the user to monitor various data channels. For the CONUS experiment, the timed list mode offered many possibilities for later data analysis, hence it was chosen as the main data acquisition mode. Typically CANBERRA DAQ systems are controlled via their software GENIE2K, but the Lynx offers two more ways of communication.

### 2.3.1 Web Interface

The first method for communicating and controlling the Lynx is a web interface. This can be used with any browser, since it is implemented with Adobe Flash. Via this interface, all important settings can be viewed and changed. Furthermore the web interface offers the possibility to plot the data in real time. This is especially useful for in situ applications, a screenshot is shown in figure 2.8.

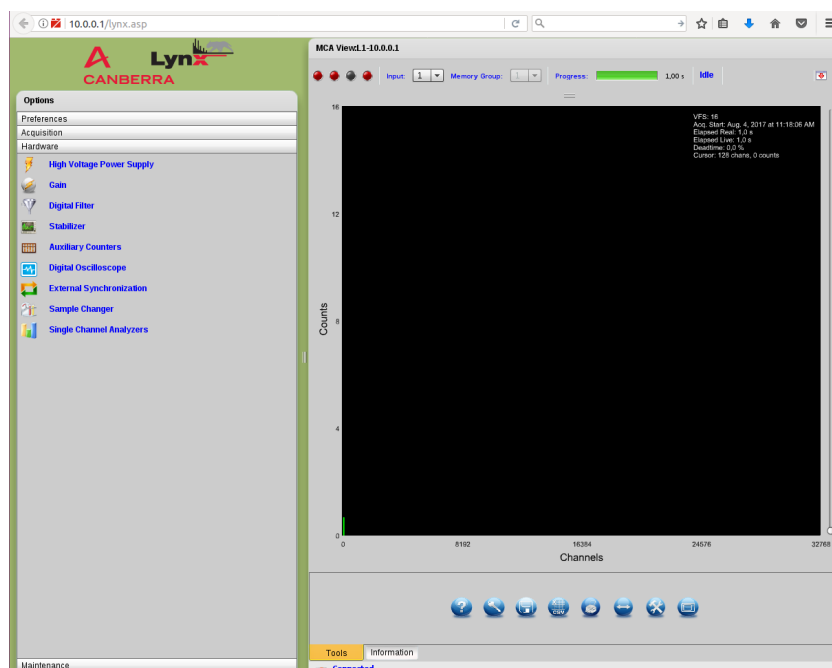


**Figure 2.8:** The web interface, which can be used to control the Lynx system.

Another positive aspect is that it does not require any set up steps. One just has to be connected to the Lynx system and no further installation of additional software

(apart from a browser) is required.

### 2.3.2 Lynx SDK

The second additional way of controlling and using the Lynx system is the Lynx SDK. The software package provided by CANBERRA offers the option to create a personally configured application, which is able to communicate with the Lynx system. The supported languages are:

- Python
- Java
- Dot.NET
- C++

Yet one has to keep in mind, that not all language supports offer the same set of functions. So one important example is the Digital Oscilloscope, which can only be accessed with C++ and Java. For all supported languages, simple examples are provided to test the basic functions. Furthermore the SDK has a communication library, which gives a short description of all available functions. With the SDK one can fully control the Lynx system, which includes starting and stopping a measurement, setting parameters as well as saving the recorded data. For a short introduction see D.2.

### 2.3.3 Timed Listmode (TLIST)

The used format for all the measurements done with the Lynx system will be in the TLIST format of the Lynx, which means all the events will be saved as a time stamped list. This method has a drawback, because only with the help of the Lynx SDK, data can actually be saved into a file. The creation of a time stamp is not straight forward, since the Lynx only saves the event channel, and the time when this occurs has to be reconstructed from internal registries. The following code example is written in Python and shows this reconstruction of the time stamp:

```
#get the recorded time for the current event, which does not
correspond the to actual event time
recTime=event.getTime()
#get the recorded channel of the current event
recEvent=event.getEvent()

#Verify whehter the event in the buffer is a valid event
if (0 == (recTime&ROLLOVERBIT)):
    #Now a valid event has been reocded
    Time = RolloverTime | (recTime & 0x7FFF)
else:
```

```

#The event is not valid, eg. an old event which has not been
  cleared,
#the registries get reset
LSBofTC = int(0)
MSBofTC = int(0)
LSBofTC |= (recTime & 0x7FFF) << 15
MSBofTC |= recEvent << 30
RolloverTime = MSBofTC | LSBofTC

#goto next event and skip saving
continue

#If the else-clause is not triggered, the Timestamp is
reconstructed
#and can be accessed via the variable Time

```

This means, only when the time of the event does not trigger the ROLLOVERBIT, an event is present and the timestamp for the event can be reconstructed via:  $\text{Time} = \text{RolloverTime} | (\text{recTime} \& 0x7FFF)$ .

The current measurement script<sup>2</sup> was set up such that each measurement file has two types of entries: events and status lines. Events have two components, the channel and time stamp of the event.

**#example event entry:**

```
35 2804557.4
```

**#example status line entry:**

```
Start 2017-07-27 12:57:58.320000 2709637 2719744 100 3463 0.003191
```

The status lines contains the following information:

- 2017-07-27 12:57:58.320000: the start time of the measurement (current system time)
- 2709637 2719744: the current live-time and real-time in  $\mu s$
- 100: the timebase used by the system in  $ns$
- 3463: the high voltage at the HV-output of the Lynx
- 0.003191: the dead-time calculated by the Lynx

### 2.3.4 Synchronization

One very important aspect for the final CONUS measurements is the synchronicity of the resulting TLIST data, because for the final physical data set of the CONUS

---

<sup>2</sup>Effective Date: August 2017

experiment four energy spectra are combined in anti-coincidence. The Lynx system offers such a feature, where multiple systems can be synchronized. Therefore one system has to be set to master, whereas the other system will be set to slave. The master has two options to choose from, but for the TLIST mode only one option is available. This mode has a fixed pulse frequency of 1 MHz. The master Lynx outputs a square signal which the slave systems use to synchronize. So the labelled *SYNC* connector of the Lynx acts as an in- or output depending on the synchronization setting. When setting up the synchronization it is useful to check the signal quality of your master Lynx, as shown in figure 2.9.

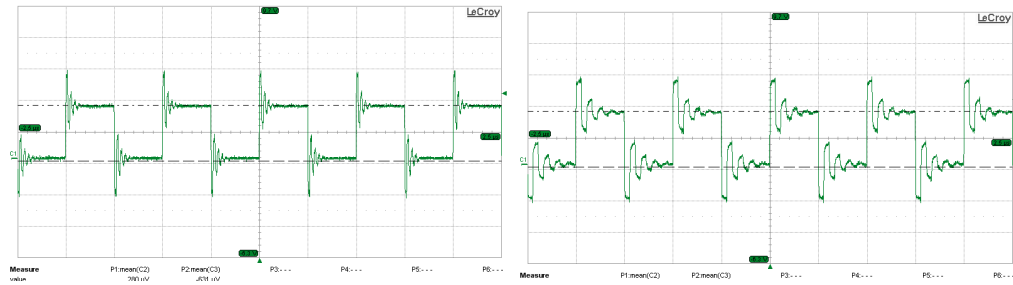


**Figure 2.9:** Difference between two synchronization pulses produced in MasterB mode for Lynx2 (left) and Lynx4 (right).

The figure shows the sync-signal which the Lynx outputs if it is set to master mode. One problem encountered during a simple test was that the bad signal quality of the sync-signal from Lynx4 made the slave Lynx time out, because the synchronization pulse was not recognized. Further information about the process of synchronization of the Lynx system is presented in section 3.5.

# 3 Muonveto System for CONUS

The CONUS experiment will be located at a rather shallow depth of 10-45 m water equivalent (w.e.)(see 2.2.1), therefore the cosmic radiation has a big influence on the background of the spectral energy data. This means a good suppression of this cosmic radiation is crucial. The focus of this chapter is on the muonveto system, so the active component of the shield, whereas the next chapter 4 will go into further detail about both components of the shield (active+passive), as well as testing it with detectors inside the CONUS shield. The goals for this chapter are:

1. Tune the muonveto system to reach a good background suppression
2. Try to further improve the muonveto system

To quantify the results for the tuning process, energy spectra with a germanium detector and with/without the muonveto system are measured and then the count rates are compared in order to calculate the suppression rate of the background signals. The spectra are recorded using a Lynx DAQ (see 2.3) and a semi-coaxial high-purity Ge detector (CONRAD). With these measurements the performance of the muonveto system can be quantified.

## 3.1 Scintillator Plates

The hardware for the myonveto system consists of 20 photomultiplier tubes (PMT) from the company HAMAMATSU (model R11265U-200), which detect the deposited light of the incoming particles. Theses PMTs are installed inside of nine plastic scintillator (scintillator material EJ-200) plates by Scionix Holland BV. The PMTs are installed in three different plate models, which are shown in figure 3.1. The plates were tested by Scionix before they were shipped to Heidelberg and the results of these tests are shown in the Appendix A. The plates received a short inspection on arrival, where the high voltage was supplied and an oscilloscope was used to check whether they work. These short tests were only to ensure the plates were not damaged during transport. The plates are covered with black non-transparent film, which is strengthened with black tape where the PMTs are installed. This outside film and tape ensure that there is no visible light hitting the scintillator material. This would result in a very strong background signal, which would render the signal from the PMT useless.

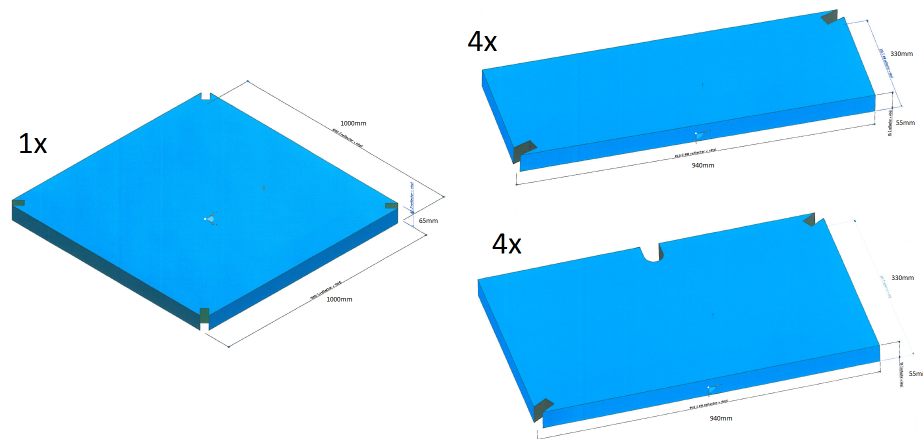


**Figure 3.1:** The technical drawings showing the three models of scintillator plates used and their dimensions as well as the quantity of each plate.

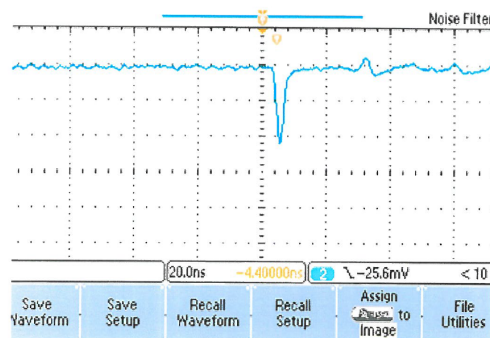


**Figure 3.2:** Response from one of the spare PMTs, performed by Reinhard Hofacker.

## 3.2 Photomultiplier Tubes

The total amount of ordered PMTs is 22, of which the 20 best were chosen and sent to Scionix to be installed into the scintillator plates. This very first exemption was done by Reinhard Hofacker at the MPIK. The remaining PMTs will be spares in case of a critical problem during the experiment. To make the scintillator plates more reliable in case of a PMT failure, each scintillator plate has two PMTs, the top plate even four, so a single broken PMT would not affect the background reduction drastically. The pre-tests of the individual PMTs were done at the MPIK, the PMTs were put into a Faradaybox and the signal response to single events were analysed with an oscilloscope. An example for oscilloscope screenshot is shown in figure 3.2. According to their strength, an appropriate position of the PMT inside the CONUS shield was chosen. The technical sheets of the PMTs are shown in the appendix A.



### 3.3 Background

For setting up the muonveto system, one has to keep in mind that the cosmic radiation induces two kinds of signals. There are the prompt events, i.e. states inside Germanium and any other material which emit radiation within a range of  $[\text{ns}, 200 \mu\text{s}]$  of the incident muon, so the prompt component. The second kind of signals are coming from excited states, which decay in a time range between a few milliseconds up to the second range. This means we generally have to deal with two kinds of signals, since the background is dominated by prompt events, one has to deal with them first. To filter out the prompt events, the data acquisition has to be stopped for a certain amount of time  $\mathcal{O}(100 \mu\text{s})$  after the incident muon. This is usually achieved by using an anti-coincidence measurement, which has to be supported by the used DAQ. To improve the efficiency of this method, there are several parameters (e.g. threshold and interruption length) which have to be fine tuned, this will be presented in the following section 3.4. The system, which interrupts the measurement for a fixed amount of time and prevents data from being taken, will be referred to as static muonveto system.

For the delayed events this task is more complex, since increasing the acquisition interruption for all the events, will result in a high dead time of the measurement. As an example, depending on the depth of an experiment, the muon rate might be as high as  $20000 \frac{\text{cts}}{\text{kg-day}}$  with a required length of four seconds to catch most of the delayed events, for every 24 hours of measurement only less than 2 hours of use-able data. This would not be feasible, plus the delayed events only make up a small percentage of the total signals. Therefore such a static muonveto system with a fixed window length of tens of microseconds can suppress the muon background very effectively. To further improve the static muonveto system, Werner Maneschg had the following idea: modifying the length of the measurement interruption according to the energy of the incident muon. As shown in 1.1.1, the energy deposited in the scintillator can be described via (1.2), which shows the energy a muon loses while travelling through the scintillator material. This depends amongst other things on the velocity of the muon  $\beta = v/c$  and the maximum recoil energy  $T_{MAX}$ . For more details about scintillators, see section 1.1.1.

The idea is that a higher energy can excite states with a longer decay time, more details to this system will be presented in section 3.5.

### 3.4 Commissioning of the Muonveto system

To start the commissioning phase, the entire shield for the CONUS experiment will be tested thoroughly at the MPIK, before the experiment will be set up at its final destination. Therefore, the shield for the CONUS project is first assembled inside the low-level laboratory (LLL) at the MPIK Heidelberg to test it, which is at a depth of 15 m (w.e.). The first part of the commissioning process was

testing the general function of the scintillator plates. This test was performed by supplying the required high voltage and then looking at the response of the PMTs on an oscilloscope. Except one plate, all the plates performed very well and showed a response peak of  $\mathcal{O}(-50\text{ mV})$  to incoming muons. The scintillator plate with the PMTs 1476 and 1493 did not perform as expected. The trace of PMT 1493 is shown in the left part of figure 3.3, the baseline of the PMT should be at stable voltage, but the signal from PMT 1493 shows a sine like superposition. The error was isolated by turning off the light in the laboratory where the test took place, the baseline improved a lot, and is shown in the right side of figure 3.3. This light leakage is not a big issue, because the steel cage around the shield is non-transparent. Figure 3.4 above shows two images taken during the commission phase of the CONUS shield. The exact position of the plates and PMTs is shown in figure 3.6. The individual PMTs are then combined via a logical OR using a discriminator built by Sebastian Hummel from the electronic department of the MPIK. These discriminators are mounted in a NIM rack and three discriminator slots are needed, in order to combine all PMT signals. The output of the discriminator is a TTL pulse with a selectable length between 128 ns and 650  $\mu\text{s}$ . The cable diagram for the discriminators are shown in the appendix in figure A.1. Furthermore the NIM rack shown in figure 3.5 holds the high voltage supply for the PMTs as well. One aspect concerning the PMT signal combination: an incoming muon might trigger more than one scintillator plate, depending on its incoming angle. Considering they travel at a relativistic velocity, if they trigger two scintillator plates, they are triggered almost simultaneously. The same applies for the PMTs of a single plate, triggering the same muon. Hence the overlap of logic signals is negligible.

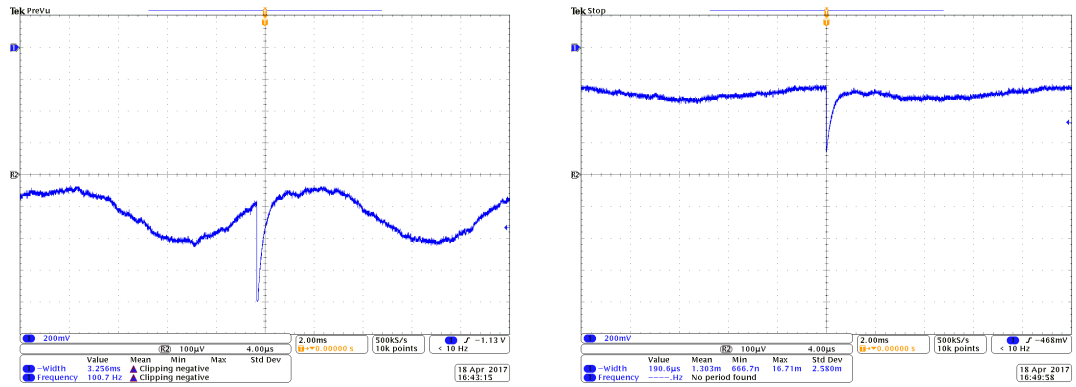


**Figure 3.3:** Left: The trace from PMT 1493 shows signs of light pollution. Right: The response of the same PMT with the lights in the laboratory turned off.

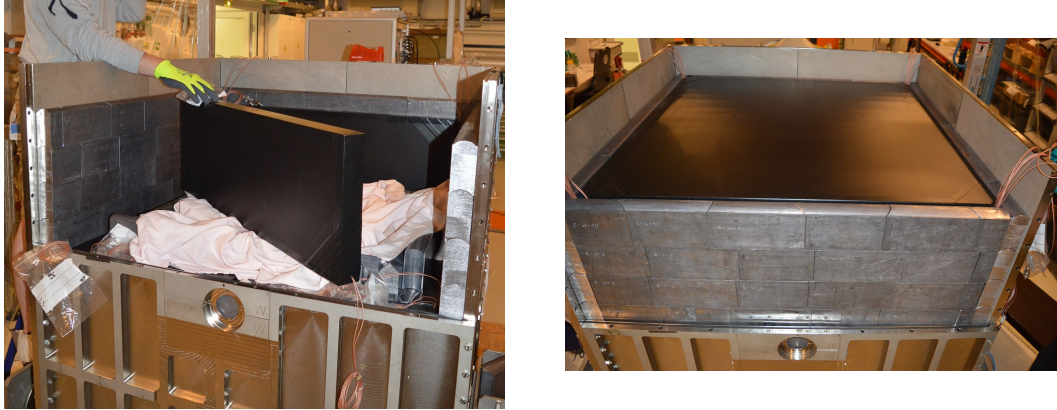


**Figure 3.4:** Left: Image taken during the commissioning phase, with a upper side scintillator plate.  
Right: The top plate at its position within the shield.

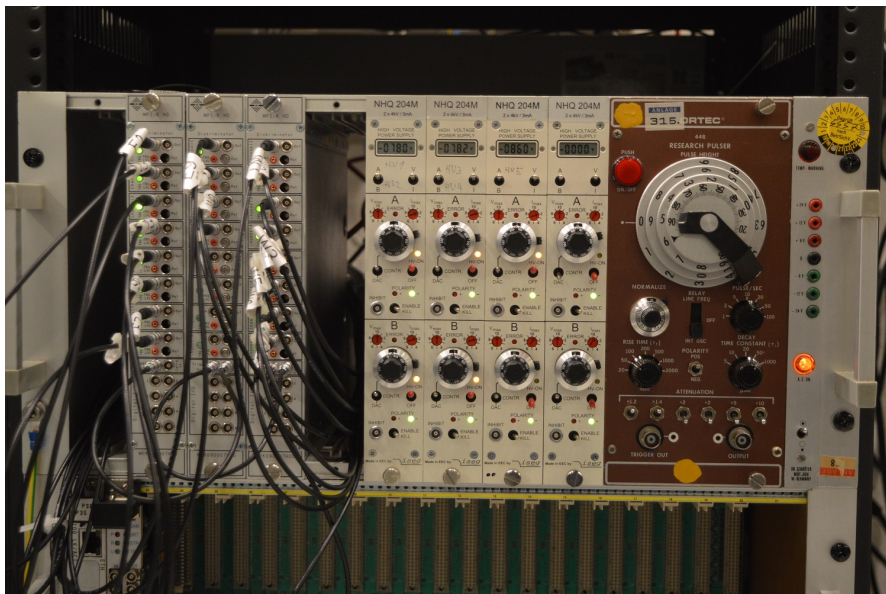


**Figure 3.5:** The used modules for the commissioning phase of the CONUS experiment. From the left: three discriminator slots, four ISEQ NHQ204M high voltage modules and an ORTEC Research Pulser.

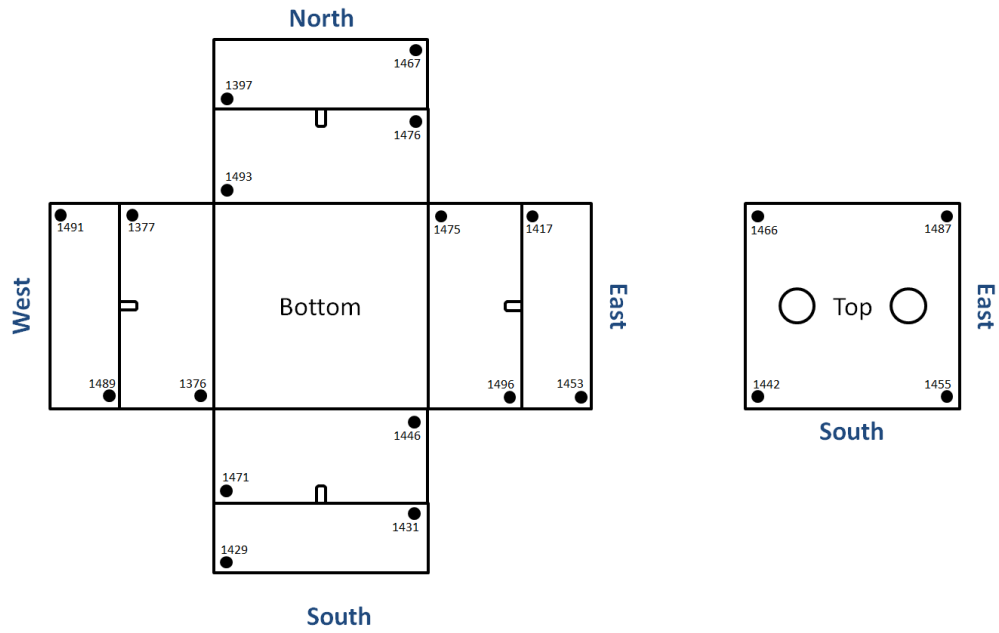


**Figure 3.6:** The exact position of the scintillator plates inside the shield, as well as the PMT position. The cardinal direction are in the relation to the final position of the CONUS experiment in the nuclear power plant.

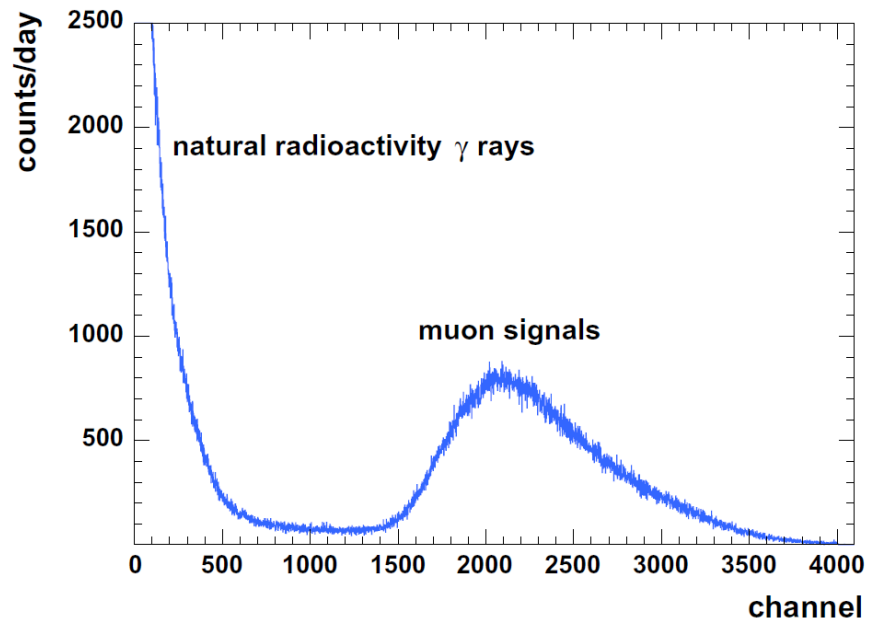


**Figure 3.7:** An example PMT energy spectrum, which shows the components effecting it. Taken form [17].

### 3.4.1 Thresholds

The first task was setting the thresholds for each PMT. The threshold is the voltage, at which the discriminator recognizes the input signal as a muon signal. This depends on the strength of the individual PMT, hence the set-up process has to be done for each PMT individually. The PMT spectrum has two main components, the natural radioactivity and the muon component. The separation of the two components shown in figure 3.7 is not always easy, since there sometimes is an overlap and not a clear separation as in the example shown. One way of determining the threshold would be using two plates and measuring the spectrum with one scintillator and use the second one as an anti-coincidence source, this method was used in [34] for the scintillator plates of the GIOVE set-up. Since the scintillator plates for CONUS were installed in the shield immediately to not stall the commissioning phase. This meant that this method was applicable for all the plates. Therefore, the tuning process was done differently. The idea is to find the rough shape of the PMT energy spectrum by looking at the count rate of the incoming PMT signals. This means measuring the count rate at different threshold settings and comparing the rates. For this task a HAMEG Counter unit was used with the TTL signal provided by the discriminator, figure 3.8 shows the schematic set-up. After a few iterations of the thresholds, the best settings that were found achieved a reduction rate close to the GIOVE value, table B.1 shows the used thresholds for the individual PMTs. The best suppression values were reached after testing different settings, because for low amplitude PMTs the threshold is close to the noise level. Having the threshold below the noise level, the suppression rate increases rapidly and leads to un-physical results.

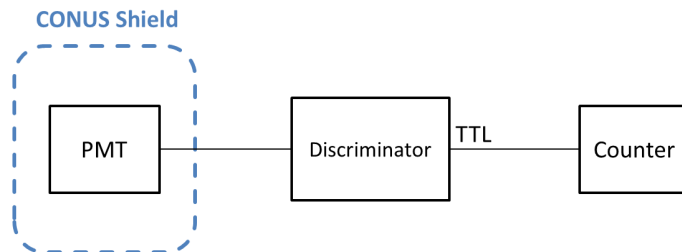


**Figure 3.8:** The wiring diagram for the count rates measurement of a PMT in order to set the threshold.

With this set up, the count rates in a 30 second window were recorded for different threshold voltages. To estimate an error for the count rate, one setting was measured ten times in a row. This led to an estimated relative error of  $\sim 3\%$ . The results were then plotted and an example is shown in figure 3.9, this was repeated for all the PMTs and the remaining plots are shown in appendix B.1. From the plots produced, a threshold setting for the PMT was deduced.

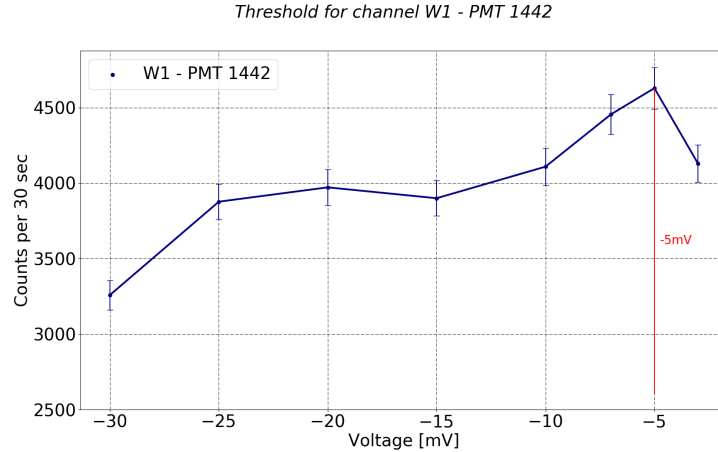


**Figure 3.9:** An example threshold measurement for PMT 1442. The selected threshold setting is indicated by the red line.

### 3.4.2 Window Length

The window length is the amount of time for which the data acquisition is stopped after an incoming muon in the scintillator plate. This refers to section 3.3, where the difference between prompt and delayed events is explained. For the first iteration of the muonveto system, it will only reduce prompt events, which means a fixed length is used to stop the data acquisition. The problem concerning the window length is the so called *deadtime*  $DT$ . This is the amount of time from the total measurement time where no data is taken. It is usually given in percent. It should be as low as possible and a realistic value is around  $\mathcal{O}(1\%)$ . The duration of a measurement has two components: the real-time and the live-time. The real-time refers to the time difference between the start and the end of a measurement, whereas the live-time is the data acquisition duration. These two values can be used to calculate the deadtime of a system according to :

$$DT = \frac{\text{real-time} - \text{live-time}}{\text{real-time}} \quad (3.1)$$

The initial window length was  $82 \mu\text{s}$ , which is deduced from the GIOVE muonveto system, where a similar value is used. For GIOVE this window length leads to a deadtime of roughly 2%. For the CONUS set-up, which uses a different DAQ system (Lynx), the  $82 \mu\text{s}$  lead to a deadtime of roughly 0.1%. Thus the window length was increased to  $164 \mu\text{s}$ , which led to a deadtime of the system of  $\sim 0.3\%$ . The higher value for the window length was used, because it is a good balance between keeping the deadtime low and catch more prompt events due to the longer window.

### 3.4.3 Resulting Efficiency

The thresholds as well as the window length described above were used and lead to the following measurement results. To quantify the thresholds, energy spectra

with and without the muonveto system active were recorded and a reduction rate was calculated from the count rates in various energy ranges. To minimize the influence of statistical errors, the measurements were at least 48 hours long. The reduction rate refers to the amount of removed muon-induced signals from the energy spectrum of the detector. The goal was to reach a reduction rate close to the reduction reached with the GIOVE muonveto system, of up to 99% of the muon background removed from the measured energy spectrum. The best settings led to the green spectrum in Figure 3.10, which shows the energy spectra of the background radiation present in the low-level laboratory (LLL) at the MPIK. The grey spectrum is recorded without the muonveto system active, whereas the green spectrum is recorded with the muonveto system active, using the best thresholds. The separated energy spectra are shown in appendix figures B.3 B.4. The measurement with muonveto started on the 30<sup>th</sup> of June 2017, the measurement without muonveto started on the 5<sup>th</sup> of July 2017. From these two spectra, the reduction rate of muon events in certain energy ranges was calculated according to (3.2) and is shown in table 3.1. Furthermore the following gain and shaping settings were used to obtain the resulting spectra:

- Fine Gain: 1.0
- Coarse Gain: 2.82
- Rise Time: 6.0
- Flat-top Time: 0.8

$$R_R = 100\% - \frac{CR_{\text{with veto}}}{CR_{\text{without veto}}} \quad (3.2)$$

The coarse gain setting only offers fixed values from the Lynx system and for this measurement, it was set to show the spectrum in the energy range from 0 - 2700 keV. As for the shaping times, the Lynx uses a trapezoidal filter which can be stretched via the flat-top time, or set to a Gaussian shape by setting the flat-top time to zero. The shaping times shown here are the optimum shaping times for the Ge detector CONRAD, which led to the best resolution.

| Energy Range<br>[keV] | Count rates:<br>muonveto OFF | Count rates:<br>muonveto ON | Reduction $R_R$<br>[%] |
|-----------------------|------------------------------|-----------------------------|------------------------|
| 45 - 50               | $101 \pm 3$                  | $2.85 \pm 0.69$             | 97.2                   |
| 45 - 100              | $1130 \pm 11$                | $65.32 \pm 3.31$            | 94.2                   |
| 100 - 500             | $9842 \pm 32$                | $288.08 \pm 6.95$           | 97.1                   |
| 520 - 2620            | $8635 \pm 30$                | $99.15 \pm 4.08$            | 98.9                   |
| 2620 - 2700           | $98 \pm 3$                   | $0.84 \pm 0.38$             | 99.1                   |
| 45 - 2700             | $20\,537 \pm 46$             | $464.61 \pm 8.82$           | 97.7                   |

Count rates in  $\left[\frac{\text{cts}}{\text{kg}\cdot\text{day}}\right]$

Measurement with Muonveto OFF: 05/07/2017, duration: 110h

Measurement with Muonveto ON: 30/06/2017, duration: 65h

**Table 3.1:** Reduction rates in various energy ranges of the energy spectrum recorded with the Ge detector CONRAD.

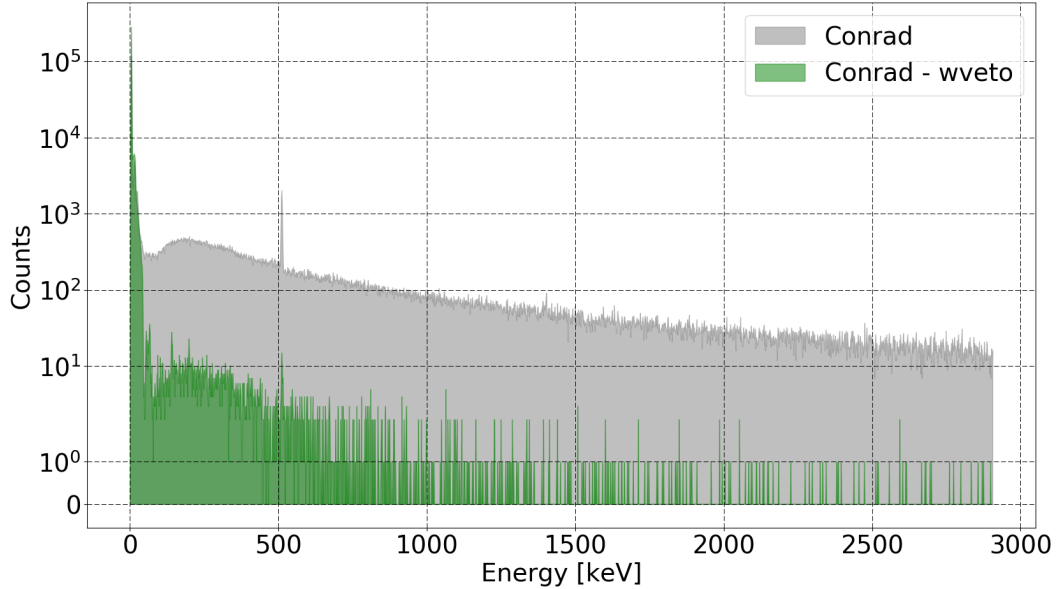


**Figure 3.10:** An overlay of the two energy spectra with the Ge detector CONRAD: (green) for the measurement from 30/06/2017, with the muonveto system ON; (grey) for the measurement from 05/07/2017, with the muonveto system OFF.

### 3.5 Dynamic Muonveto - DMV

So far, the implemented muonveto system is a static one, in the sense that the length of the data acquisition interruption has a fixed length. The idea behind a dynamic muonveto system is that a certain class of muons with a specific energy are mainly responsible for the generation of secondary neutrons. These in turn are responsible for a delayed neutron induced isomeric excitation of germanium nuclei. Therefore the excited states vary based on the deposited energy and depending on the excited state itself, the corresponding decay time of the respective state. One example is the neutron capture of  $\text{Ge}^{71}$ , the resulting  $\text{Ge}^{71\text{m}}$  is a metastable isomer and transitions back to  $\text{Ge}^{71}$ , emitting a gamma-ray with an energy of 198.4 keV and a delay of roughly 20.4 ms [35]. More information about the muon induced background is given in section 1.2. This means, if one is able to relate the energy of an incoming muon to the measured energy from the scintillator, one could vary the window length of the data acquisition stop. An example of these states in germanium are shown and analysed in section 4.2.3. The influence of these states could be reduced, if the neutron-inducing muons triggering these states can be identified and the data acquisition could be interrupted accordingly. To demonstrate another aspect with a static muonveto system, figure 3.11 shows an example where the difference between incoming muons and their deposited energy can be seen. This figure is a screenshot from the internal digital oscilloscope (DSO) of the Lynx.



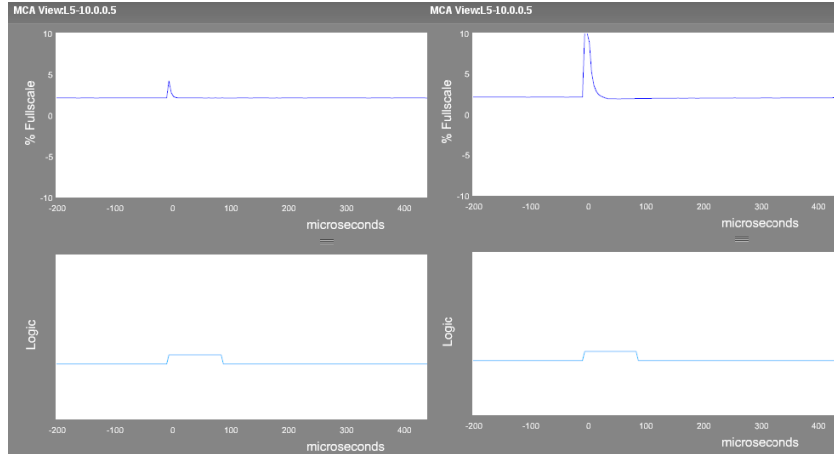


**Figure 3.11:** The incoming signal from a PMT on the two top graphs and the corresponding anti-coincidence window on the bottom plots.

The two top plots in figure 3.11 show the converted PMT signal and the two bottom plots show the TTL signal which interrupts the measurement. The signal form shown in the plot is an energy representative of the incoming PMT signal. One cannot directly derive a deposited energy from it, since the actual PMT signal cannot be accessed. But it illustrates the fact that a static muonveto system does not discriminate between those two events. If one assumes that the right example in the figure is a muon with a high energy and thus having a high energy deposition per path length according to (1.2) and the left example a very low energetic muon, the window lengths could be modified and still "catch" the events in the Ge produced by both muons. To remove the events created by the two muons shown in the figure, the window length for the measurement interruption of the left example could then be reduced and still account for the muon-induced event, whereas for the right example, the window length would have to be increased in order to "catch" the resulting Ge signal which is produced by the muon. This method would increase the efficiency of the system, since the low energy muons which only produce "fast" decaying states, would receive a short window length and the very high energetic muons would receive a longer data acquisition stop, additionally this could decrease the deadtime of the system. As described in section 1.2, one has to be careful, because the deposited energy does not directly correspond to the muon energy  $E_\nu$ , since it depends on the distance travelled of the muon within the scintillator  $dx$  from equation (1.2). Furthermore, it is important how the Lynx handles input signals which saturate. Therefore trying to find a calibration between the PMT signal strength and the converted Lynx signal is important, since it is not obvious how the Lynx handles incoming signals which are outside the optimum amplitude range. Before the details of the individual peaks are analysed, a proof of concept has to be done. With the Lynx system as DAQ, two ways to implement a dynamic veto were identified within this work and shall be investigated in the following. The ideal solution would be a pulse-shape analysis (PSA) of the PMT signal, which the Lynx was supposed to support. As

of August 2017, the Lynx does not support PSA. However, the Lynx does have an internal oscilloscope, which was already used for figure 3.11. So the first approach is to read out and use this function as an alternative way to analyse the PMT signals, which is presented in section 3.5.1. Furthermore, a second approach will be presented in section 3.5.2, where the PMT energy spectrum is recorded as a timed list.

### **3.5.1 Pulse Form Analysis**

There are three aspects which have to be addressed during this principal proof: writing speed, pulse form and saturation level. The latter means how the Lynx deals with pulses which saturate the input, since it is important to understand, which of the incoming muons have a high energy. The main issue at first is obtaining a rough pulse shape from the Lynx. As previously mentioned, when releasing the Lynx DAQ, CANBERRA intended a pulse-shape analysis for it, but as of August 2017, this has not been implemented. But for this analysis, only the information about the pulse height is needed, therefore a workaround might be possible with the internal digital signal oscilloscope (DSO) of the Lynx. The Lynx SDK does not support this function in Python, therefore Java was used to obtain the values for this part. To access the Lynx DSO data, the following code example is used:

```
lynx.getDsoData().getSamples().get(X).getAnalog().get(0);
```

Here `lynx` represents an instance of the Lynx DAQ (more details about the Lynx SDK see Appendix D.2), and `X` is the index of the  $X^{\text{th}}$  element of the analogue trace, which has a none modifiable length of 256 values. This means, the saved pulse form has a fixed resolution, which directly depends on the timebase the Lynx uses to save them. Thus with a simple loop, all elements of the trace can be accessed. Starting from the Python script, which was created to start and save all the measurements for this thesis, a Java version was implemented, which additionally saves DSO data for each occurring event. As a first test, the writing speed of the DSO data was analysed. Therefore only one PMT signal is used; however, for the full system a combination of all 20 would be needed. For this first test, the PMT1442 is used as an input source. The Lynx was set up such that the recorded energy spectrum of the PMT was similar to the example shown in figure 3.7. Therefore the following settings were used:

- Fine Gain: 1.0
- Coarse Gain: 16.0
- Rise Time: 1.0
- Flat-top Time: 0.8

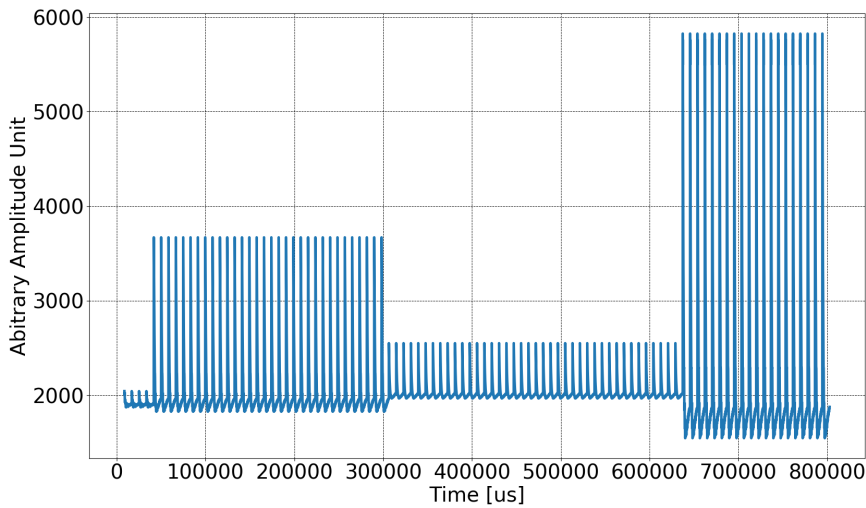


**Figure 3.12:** The analogue trace of the incoming PMT signal, received from the Lynx DSO.

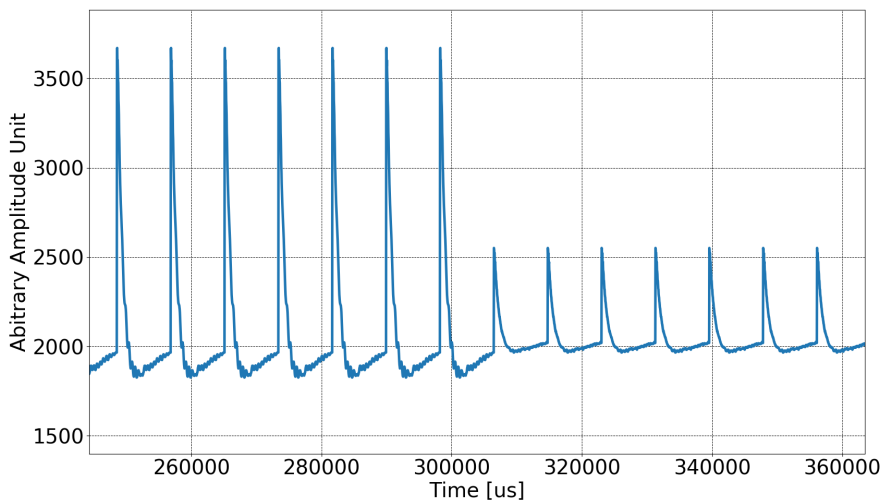


**Figure 3.13:** The analogue trace of the incoming PMT signal, received from the Lynx DSO further zoomed than 3.12.

The analogue trace for the PMT signal is shown in figure 3.12, each peak which is in the graph corresponds to the content of the DSO memory once the Lynx recognizes an event and writes it to the TLIST. This means that the trace is only updated every 20 - 40 events for this particular example measurement. The event rate at the input is roughly 100 Hz, so it takes the DSO somewhere between 200 ms and 400 ms to update its content, and the information for all the events in between is lost. This rate is too low, since for a full system, the signal from all 20 PMTs must be combined to achieve the best reduction possible. When looking at figure 3.13, one can see that the peaks can be discriminated by their amplitude pretty

easily. Therefore the system in general might still be viable, but with the current speed of the DSO it cannot be realized.

### 3.5.2 Energy Spectrum Analysis

The second approach proposed to implement a dynamic muonveto system is to analyse the energy spectrum of a PMT, select muon events above a certain threshold and cut the Germanium data according to those events. For this approach, the analysed data is the TLIST which is recorded. To test the general viability of this approach, two sets of data are taken. First, an energy spectrum is recorded in anti-coincidence with only one PMT as muonveto system. Afterwards, an energy spectrum is recorded without anti-coincidence, and the signal of the PMT is measured simultaneously with a second Lynx DAQ as the energy spectrum is recorded. This method is shown in figure 3.14.

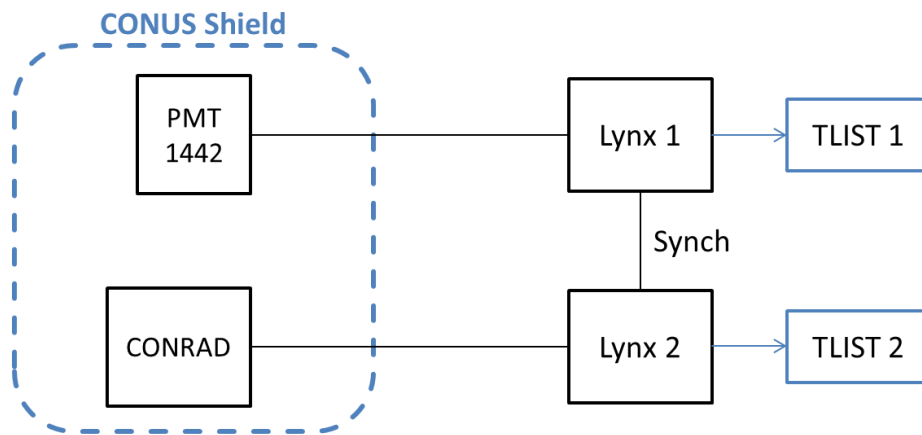


**Figure 3.14:** The schematic configuration for the performed measurement for section 3.5.2.

The important aspect for this measurement is synchronising the time stamps of events in the two data sets, because the energy spectra will be modified according to the PMT signal, which only results in a correct spectrum if the timestamps of the two TLIST are synchronised. In case of non-synchronicity, the spectral shape will be modified which should be visible in the resulting spectrum since the cut would be a random cut resulting in a random data loss. More importantly, the timestamps will not match and events originating from a muon cannot be linked to the corresponding PMT event. Therefore the Lynx system offers an external synchronisation where two or more Lynx can be synchronized. One of the Lynx is set to master-mode, this Lynx then provides a signal which a slave-mode Lynx uses to synchronize itself to it. One has to be careful, since not all synchronization signals have a well defined shape and might not be recognized as a proper synchronization signal from a slave Lynx, see figure 2.9. Once the Lynx have been set up properly, the measurements can be started together. To do this, the slave Lynx has to start its measurement first, since it will not start recording data,

until a valid synchronization signal is available from the master-Lynx. The only problem is, that once the master-Lynx enables the setting, a synchronization signal is produced. Ideally, this would only be the case once the acquisition starts. Therefore the measurement script for the master-Lynx has to enable the external synchronisation together with starting the measurement. As a first test, a static window length of  $164\ \mu\text{s}$  is used to recreate the same data set, as when using the PMT signal for an anti-coincidence measurement. The flow-diagram for the search algorithm is shown in figure 3.16. The first iteration of the search algorithm loops over all PMT events. If they are in a certain energy range, it takes the time stamp `TS_PMT` and creates a time range, using a fixed length of  $164\ \mu\text{s}$ . Then it checks the `TLIST_CONRAD`, whether it has any events within this list, if it does, they are removed. Then the remaining elements of the `TLIST_CONRAD` are plotted as an energy spectrum. Figure 3.15 shows an energy spectrum for the PMT1442, as well as an example selection of muon events based on figure 3.7. This spectrum can then be compared to the reference energy spectrum recorded with PMT1442 in anti-coincidence.

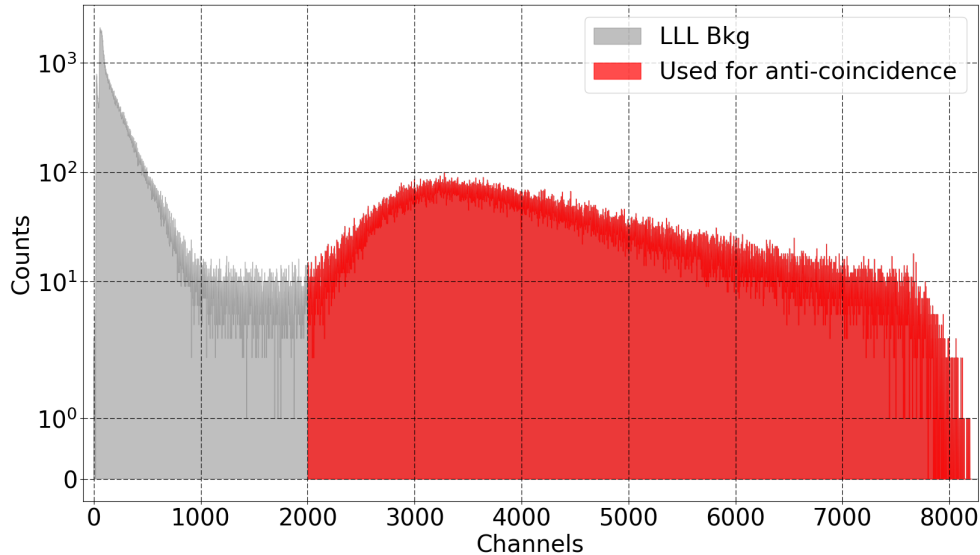


**Figure 3.15:** An energy spectrum of PMT1442 taken in the low-level laboratory at the MPIK Heidelberg. The red area represents the muon events which shall be removed.

Due to the starting procedure, there is a difference in starting times of the `TLIST` files, for the PMT and `CONRAD` energy spectra. Since the acquisition should start at the same time, the actual time stamps for the events should not have an offset. Since they start at 0, this difference in start times should not affect the further analysis. Due to complications with the synchronisation of the Lynx systems, repeated results for this measurement show no correlation of the PMT events and the detector events. So only by increasing the window length, a similar count rate as the reference spectrum can be achieved. This is only a *random removal of events*, rather than a systematic reduction of events induced by muons. This

means the synchronization of TLIST data is more problematic. After repeatedly reaching out to CANBERRA and the limited access to the internal procedures of the Lynx, a concrete solution was not found as of writing this thesis.

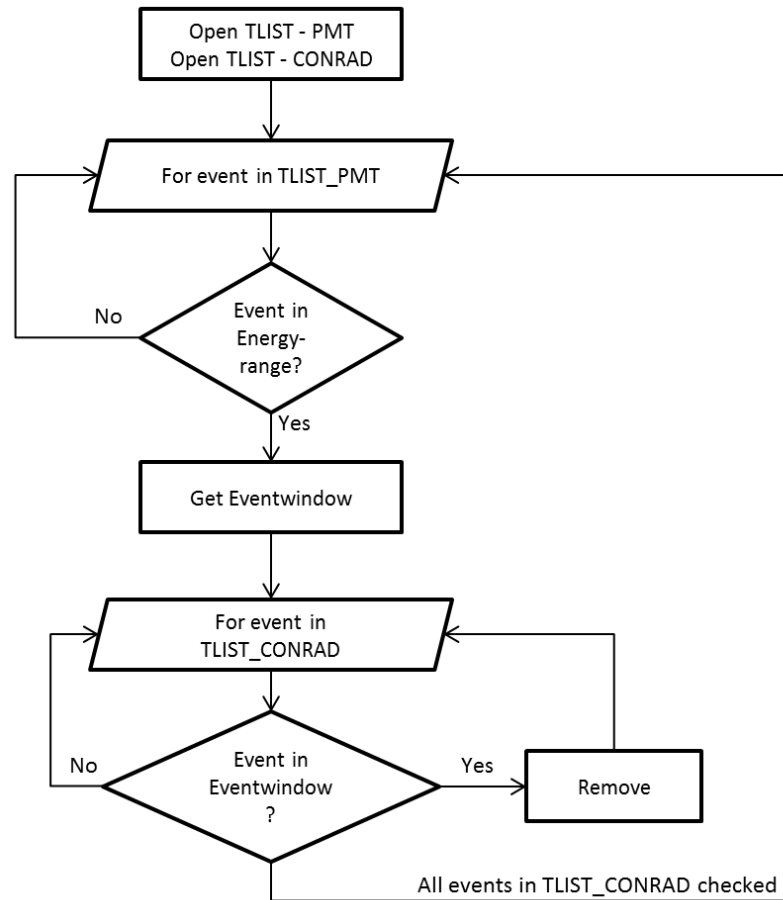


**Figure 3.16:** The flow-diagram for the script, which compares the two TLIST measured with the configuration shown in figure 3.14.

## 3.6 Results

The initial tuning of the static muonveto system was successful and the desired suppression values could be reached. The final values still got room for improvement later on. In the high energy range (above 500 keV), the suppression rate is as good as the suppression rate by the well tuned GIOVE set-up which uses a similar muonveto system. In energy range below 500 keV, the reduction rate  $R_R$  is almost 5% lower than above. There are multiple reasons which could affect the results, for one the suppression for GIOVE itself is different, because CONUS has lead in the innermost layer, whereas GIOVE uses Copper, although it is not yet apparent how this difference influences the veto efficiency. Furthermore, the lead layer in the CONUS shield might have a slight  $\text{Pb}^{210}$  impurity, which leads to a beta-spectrum which peaks at about 170 keV [16]. This would then result in a

beta spectrum originating from the lead layers inside the shield, which increases the measured count rates and decrease  $R_R$ .

## DMV

The implementation of a dynamic muonveto system was not successful. Furthermore, during the implementation problems arose, which not only affected the DMV, but rather the whole data acquisition for the experiment with the current DAQ, because for the actual data acquisition at the nuclear power plant, four detectors have the synchronized. In the context of this thesis, it was found, that for the chosen acquisition mode (TLIST), this is more difficult than initially expected. Since the guide for the Lynx did not mention any specifics about the synchronization. Both methods for implementing the DMV had troubles with the current DAQ. The favoured method of analysing the PMT pulses directly could not be implemented due to the absence of a pulse shape analysis support of the Lynx. The internal oscilloscope function of the Lynx was tested as a possible alternative, but apart from the internal transformation which is done with all incoming signals by the Lynx, the update speed of the DSO is too slow in order to be viable as a pulse shape analysis tool. The second approach, using two synchronized TLIST files to do an off-line muon rejection, only led to further problems, since during the implementation process, the synchronization was tested and all tests did not show a satisfying synchronization. Therefore, more work for the synchronization is required. One possible set-up for testing the synchronization is shown in figure 3.17, where two Lynx are connected to the same pulser. A measurement has to be started, as described in section 3.5.2. Then the Lynx should theoretically be synchronized and the time stamps should be within  $1 \mu s$  of each other.

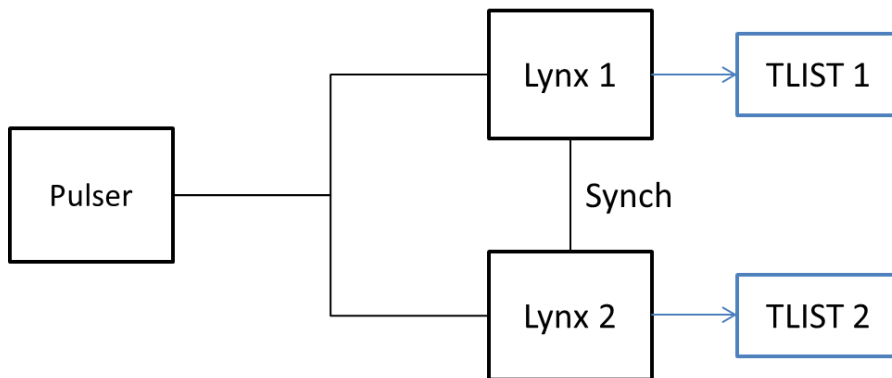


**Figure 3.17:** The schematic for a synchronization test.

The results should be more informative about how the time stamps are offset. Further feedback from the development department of CANBERRA will be very important as well.





## 4 Commissioning of the CONUS Shield

Shielding the experiment is indispensable for the results significance, therefore it is crucial to test the quality and radiopurity of the shielding materials before their final set-up close to the nuclear power plant. Furthermore, the safety regulation require the shield to be constructed in such a way, that it will not cause any structural damages to the environment around the reactor's core. The commissioning process will be split into multiple phases, starting with the initial construction of the shield and first long term measurements with one detector. Afterwards the shield will be opened and another detector will be set-up in the shield. During the third and last phase of the commissioning, one of the CONUS detectors shall be activated with a neutron source to further study its characteristics. Furthermore, the neutron suppression capabilities of the shield shall be measured. Not only will this thesis focus on the first two commissioning phases, since the second phase has not concluded as of writing this thesis. But also focus only on the measurements done with the CONRAD detector. Because the details about this experiment have not been published yet, therefore all information about the tests and measurements done with any of the CONUS detectors remain classified.

### Test Location - MPIK

The test location of the CONUS experiment is the low-level laboratory (LLL) at MPIK Heidelberg. The conditions concerning cosmic radiation are comparable to the location at the reactor site, since both locations exhibit an overburden similar to 15 m w.e. Therefore the results achieved will be a good guideline for what can be expected later on. Currently the LLL houses three more detectors, the previously mentioned GIOVE, as well as BRUNO and CORRADO. All those Ge detectors are mainly used for material screening. Furthermore the LLL is an underground storing area, for sensitive parts which shall be secured from activation via cosmic radiation.

## 4.1 CONRAD

For the first phase of the commissioning, the high-purity semi-coaxial Ge detector CONRAD will be used to make the first measurements. One reason being, that CONRAD is of similar size to GIOVE, therefore the spectra can be compared. The used diode for the detector was made by ORTEC and was previously used for the low background dark matter experiment GENIUS-TF[36]. In this section the utilized detector shall be characterized, therefore a high voltage scan was conducted, as well as measurements to calculate the active volume. This will be presented in the following.

### 4.1.1 High Voltage - Scan

One important characteristic of a detector is its depletion voltage, which is a limit for its supply voltage. The detector should be operated above this depletion voltage, because then the electric field inside the detector becomes homogeneous. This means that the charge collection of the detector becomes stable and the peak position/peak count rate of a measurement does not vary by increasing the voltage any more. Therefore the depletion voltage of a detector is important to know, since the supply voltage should be well above it. But it should not be too high as well, since this may damage the detector in the long run. More information on this topic is presented in section 1.1.1. To determine the depletion voltage of a detector, a high voltage scan has to be done. This means the detector is operated with different supply voltages and spectra of a certain energy peak are measured. This shows the behaviour of the detector in regards to the supplied high voltage. Two parameters were analysed: the peak count rate and the peak position, with a  $\text{Co}^{60}$  source. To do so, multiple measurements were done with increasing voltage, starting at 589V up to 3439V in steps of 50V. The values are off, because the high voltage unit of the Lynx, has a slight offset, the used unit has an offset of 11V. The measurements lasted for 900s at each voltage point. There were two methods used to fit the data, since the peak shape is not Gaussian, especially at the lower voltages (below 1800V). The first fit method is using a rather standard peak fit function  $f_{PF}$ , which consists of three parts: a Gauss peak form and two underground components, a linear component and a step-like function.

$$f_{PF} = A \cdot \left[ \frac{\exp\left(\frac{-(x-x_0)^2}{2 \cdot \sigma^2}\right)}{\sqrt{2\pi}\sigma} \right] + B \cdot \left[ \frac{1}{1 + \exp\left(\frac{2 \cdot (x-x_0)}{\sigma}\right)} \right] + C \cdot x \quad (4.1)$$

The second fit function used, is a combination of (4.1) with a Lorentz curve. Figure 4.1 illustrates both fit functions.

$$f_{LO} = A \cdot \frac{\Gamma}{(x - x_0)^2 + \Gamma^2} \quad (4.2)$$

$$f_{PFLO} = f_{LO}|(x < x_s) + f_{PF}|(x \geq x_s) \quad (4.3)$$

The performed data fits demonstrate an inherent problem, as the reason for the existing tails is not obvious. One possible explanation could be pile-up events.

These are events, which occur in very quick succession to each other and the system is not able to distinguish between the two events. Then either the system only registers one event and adds the amplitudes, or is able to resolve the two events, but the energy reconstruction does not work properly.

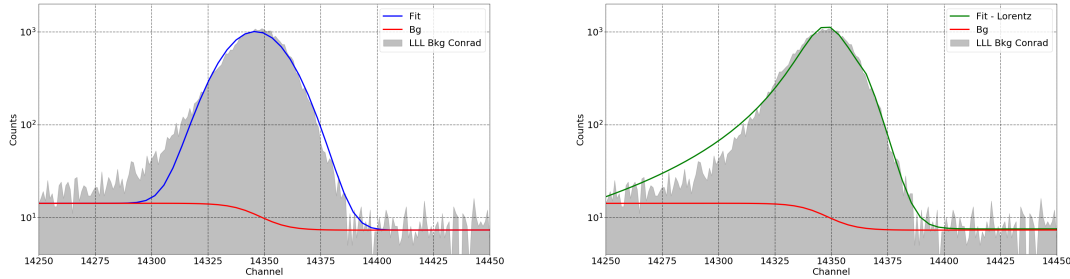


**Figure 4.1:** Left: An exemplary energy spectrum containing the 1.173 MeV line from  $\text{Co}^{60}$ , which is fitted with  $f_{PF}$ . Right: The same energy spectrum this time  $f_{PFLO}$  was used to fit the data.

This leads to events, which are in the wrong energy channel and could explain the tail. Another reason could be slow-pulses, which are events occurring in the dead-layer of the detector and whose charge is decreased by the diffusion process into the active-layer. More details on this topic is presented in section 1.1.1. The used fit routines have troubles with these non Gauss shapes and therefore is not very stable fitting all spectra correctly, which leads to missing data points. To improve the fits for the low voltage peaks, further components for the fit function are needed to replicate the non Gauss shape. This is an issue for the low voltage range of the HV scan, whereas starting at  $\sim 1800\text{V}$ , the fit is working as intended and can replicate the measured data reasonably well. This kind of fit is performed for all recorded energy spectra and afterwards the peak-position as well as the integral peak count rate is then plotted and fitted in figures 4.2 and 4.3. The individual data points for the peak position and the peak count rate, were fitted with an exponential decay function

$$a(U) = A_{MAX} \cdot \left(1 - \exp^{-\frac{U}{T}}\right) \quad (4.4)$$

Where:  $U$  is the high voltage at the detector and  $A_{MAX}$  and  $T$  are the two fit parameters. Then, the plateau part of the plot was fitted with a linear function. The intersection of the linear plateau fit and the exponential fit  $a(U)$ , is the determined depletion voltage. The error on the voltage is calculated from the statistical error from the exponential fit. The expected behaviour is, that above a certain depletion voltage, the measured energy spectra become stable concerning the peak position as well as the count rate, because the energy field inside the crystal becomes homogeneous and the charges are collected at a constant rate. This behaviour can be seen for both cases in figures 4.2 and 4.3. The resulting depletion voltages of the individual measurements are given in table 4.1.

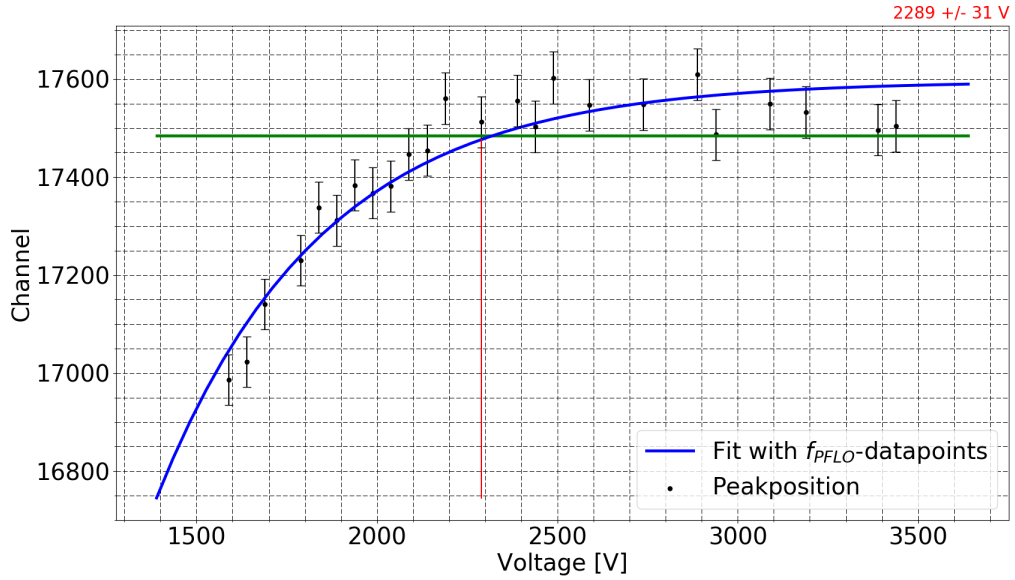


**Figure 4.2:** The peak position for the 1.173 MeV line of  $\text{Co}^{60}$ . The individual data points have been fitted with  $f_{PFLO}$ , the corresponding plot with  $f_{PF}$  is shown in the appendix in figure C.2.

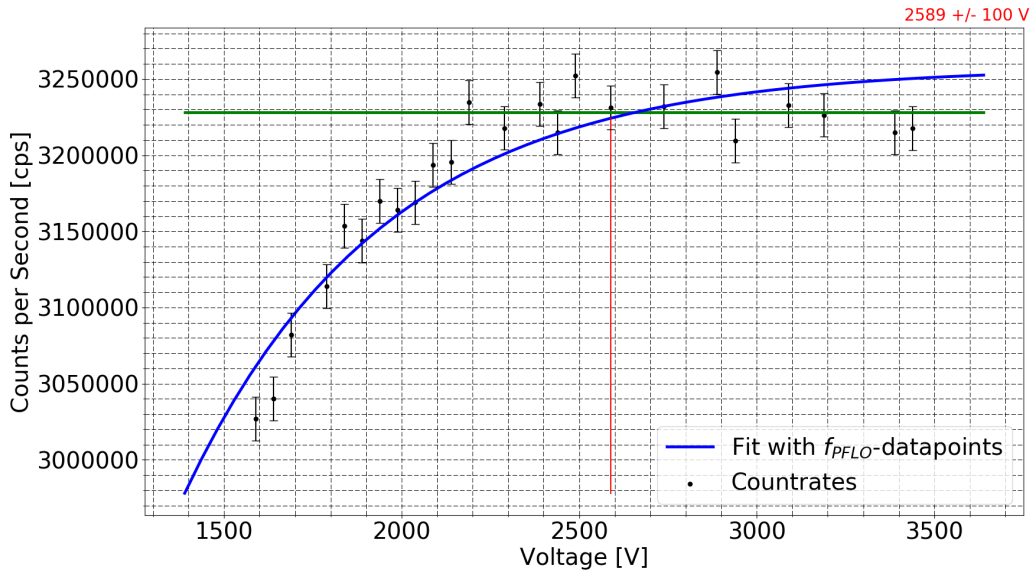


**Figure 4.3:** The peak count rate for the 1.173 MeV line of  $\text{Co}^{60}$ . The individual data points have been fitted with  $f_{PFLO}$ , the corresponding plot with  $f_{PF}$  is shown in the appendix in figure C.1.

| Measurement                  | Saturation Voltage [V] |
|------------------------------|------------------------|
| peak position - $f_{PFLO}$   | $2289 \pm 31$          |
| peak count rate - $f_{PFLO}$ | $2589 \pm 100$         |
| peak position - $f_{PF}$     | $2639 \pm 324$         |
| peak count rate - $f_{PF}$   | $3489 \pm 525$         |

**Table 4.1:** Estimated depletion voltages for the high voltage scan with the Ge detector CONRAD.

The mean received depletion voltages from the  $f_{PFLO}$ -data is  $2439 \pm 66$  V, which is in agreement with the previous depletion voltage of 2000V, whereas the voltages received from the  $f_{PF}$ -data do not agree well with the previous value, which might be due to a problem with the fit itself. So the current supply voltage of 3500V is well in agreement with the newly determined depletion voltage.

### 4.1.2 Active Volume

The active volume of a detector is the volume inside the diode from which incoming charge depositions are collected with an efficiency  $\mathcal{E}=1$ . This is an individual key feature of every detector, since total count rates are usually normalized to the active detector mass. With time the active volume of a Ge detector shrinks, due to the Lithium diffusion of the wrap-around deadlayer, this diffusion process is even further enhanced, if the detector is stored at room temperature. The active volume, influences the behaviour of the detector. The active volume for CONRAD has not been measured for several years, so this thesis gave the opportunity to update the active volume of CONRAD, starting from the crystal mass of 2.2 kg. The active volume of CONRAD was determined by taking spectra of different radiation sources at well defined distances to the crystal inside the cryostat. This is to be compared with Monte-Carlo simulations of certain active volumes. The Monte-Carlo simulations (MCS) were performed by Janina Hakenmüller, and for the measurements  $\text{Co}^{60}$  as well as  $\text{Am}^{241}$  was used as a radiation source. Both were placed at different heights (using thin plastic containers of well defined height), right next to the cryostat inside the inner most layer of the lead shield. There were four measurements taken in total, three different positions with  $\text{Co}^{60}$  and a fourth position with  $\text{Am}^{241}$ . For the  $\text{Co}^{60}$  measurements, the total counts per day of two peaks (1173.228 keV and 1332.492 keV [37] respectively) were compared to the MCS. For the  $\text{Am}^{241}$  measurement the ratio of the peaks located at 59.5409 keV, 98.97 keV and 102.98 keV were compared with the results of the MCS. The last two lines lie very close together and are evaluated as one line, since the MCS lacks the resolution to resolve the two lines separately. CONRAD cannot separate the two lines as well, the measured spectrum is shown in figure 4.4.

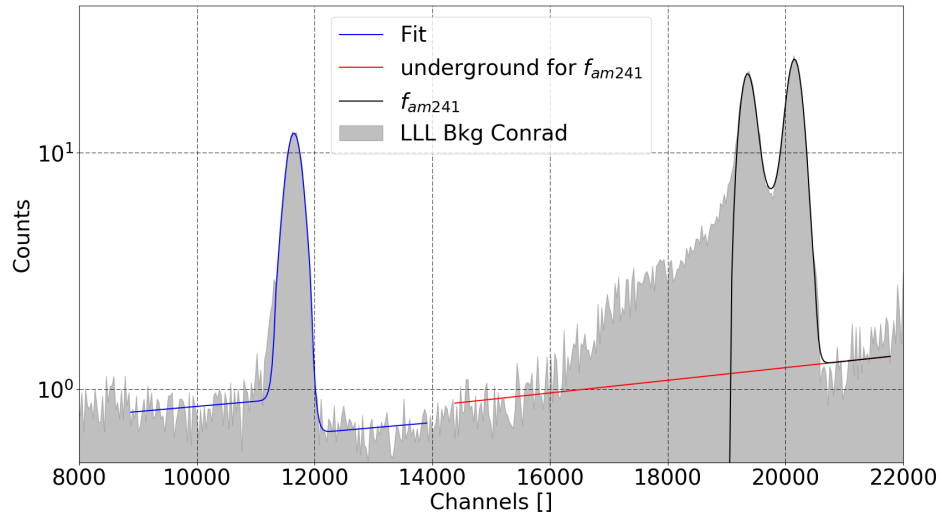


**Figure 4.4:** The Am<sup>241</sup> peak with its fit function.

This meant, for the fit for the 98 and 102 keV lines, a combination of the fit functions  $f_{PF}$  and  $f_{PFLO}$  was used:

$$f_{am241} = f_{PF} + f_{PFLO} \quad (4.5)$$

The measured values for the four different positions are shown in table 4.2. The measurement and evaluation of the spectral line was done by yours truly, and the MCS as well as the comparison was done by Janina Hakenmüller. Figure 4.6 shows the comparison with the MCS, where the received values from the CONRAD measurements are plotted together with the MCS results; the lines correspond to different active volumes.

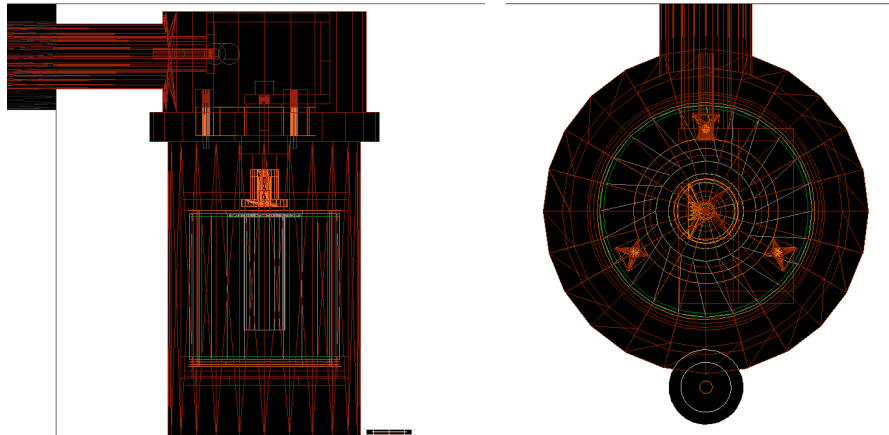


**Figure 4.5:** Left: The geometric sketch of the radiation source in relation to detector, which is used by the MCS.  
 Right: Areal perspective of the geometry used by the MCS (by J.Hakenmüller).

| Position Number | Count rates:                                        |                                                                  |
|-----------------|-----------------------------------------------------|------------------------------------------------------------------|
|                 | Co <sup>60</sup> - 1.173 MeV [ $\frac{cts}{day}$ ]  | Co <sup>60</sup> - 1.332 MeV [ $\frac{cts}{day}$ ]               |
| 1               | 1 345 876 ± 5669                                    | 1 284 067 ± 5538                                                 |
| 2               | 4 363 971 ± 10 186                                  | 4 104 699 ± 9879                                                 |
| 3               | 3 446 058 ± 9036                                    | 3 264 286 ± 8794                                                 |
|                 | Am <sup>241</sup> - 59.54 keV [ $\frac{cts}{day}$ ] | Am <sup>241</sup> - 98.97 keV + 102.98 keV [ $\frac{cts}{day}$ ] |
| 4               | 6266 ± 548                                          | 10 063 ± 694                                                     |

**Table 4.2:** The peak count rates for the four different positions, recorded with the Ge detector CONRAD.

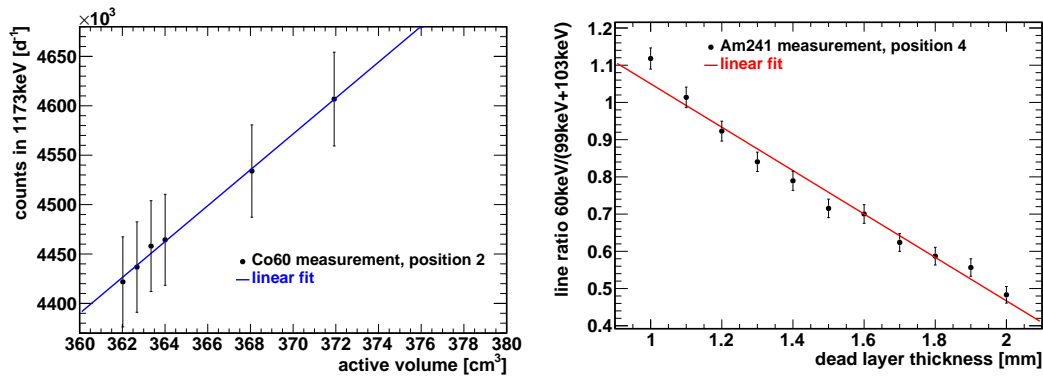


**Figure 4.6:** Left: The comparison between the MCS and the values from table 4.2, for the Co<sup>60</sup> - 1.173 MeV peak.  
Right: The comparison between the MCS and the values from table 4.2, for the Am<sup>241</sup> peak ratio.(by J.Hakenmüller)

The results of the comparison between the taken energy spectra and the MCS and the resulting active volume is shown in the following table 4.3. So the current value decreased from 2.2 kg down to 1.9 kg (79%). The last measurement of the active volume was several years ago, during this time CONRAD has been stored without cooling, which increases the Lithium diffusion, as mentioned in the beginning of this section. This might be responsible for the decrease of the active volume. So for all the following measurements, which are normalized to the active mass: 1.9 kg is used.

Dead-Layer:  $1.7 \pm 0.1$  mm from all sides

| Position Number | 1.173 MeV<br>Active Volume [ $cm^3$ ] | 1.332 MeV<br>Active Volume [ $cm^3$ ] |
|-----------------|---------------------------------------|---------------------------------------|
| 1               | 339.486                               | 342.567                               |
| 2               | 358.571                               | 359.508                               |
| 3               | 370.567                               | 371.686                               |

mean:  $357 cm^3$ ,  
which corresponds to  $1.94 \pm 0.2$  kg (79%) of natural germanium

**Table 4.3:** The estimated active volume for the Ge detector CONRAD.(by J.Hakenmüller)

## Phase 0

To ensure an effortless construction at the reactor site, a test of all the involved parts is done. The commission process started with the shields construction. The lead in use has various degrees of purity, the further inside the lead is, the more pure it has to be in order to prevent a high background especially due to  $Pb^{210}$ . Ideally one would want to use only very pure lead, but pure and old lead is hard to come by in large quantities, since new sources such as old water pipes, sunken shiploads or similar sources for lead are rarely found[16]. To prevent further impurities, the surface of each used lead brick was cleaned using iso-propanol. This cleaning process was especially important for all bricks, which had to be cut in order to fit into the shield. The whole cleaning and construction process was carried out by several members of the CONUS collaboration. After that, different measurement phases were initiated, which will be described in the sections 4.2 - 5.2.

## 4.2 Phase 1

The first phase started on the June 1<sup>st</sup>, when the shield was completed and lasted until 17/07/2017. During this time only the CONRAD detector was incorporated into the CONUS shield and the measurements started once the cage was sealed air tight.

### 4.2.1 Goals

The main objective during this first phase, was setting up the muonveto system and obtaining a first impression about the radiopurity of the CONUS shield, in terms of the achievable background levels, assuming a low contribution from the CONRAD detector itself. The commission and tuning of the muonveto system is described in detail in chapter 3.



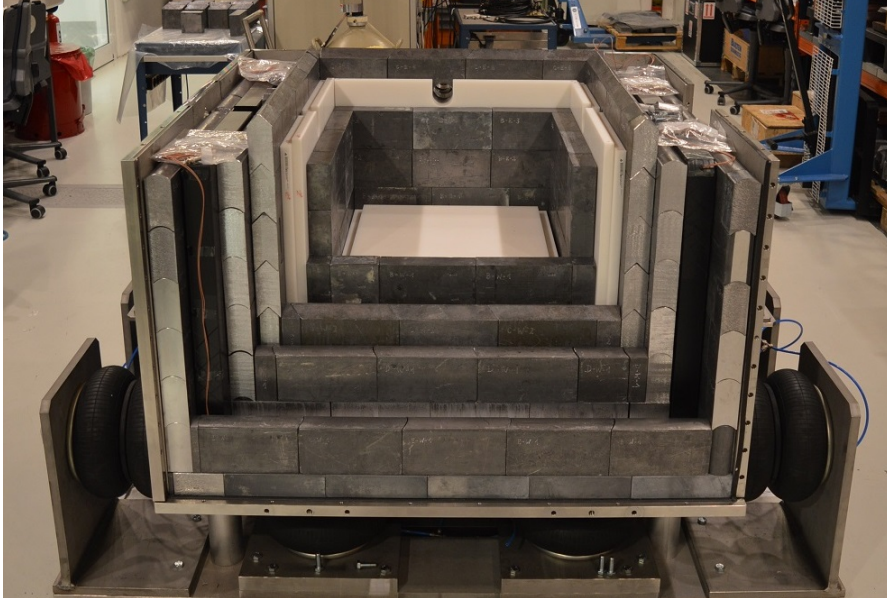


**Figure 4.7:** Image taken during the initial construction of the CONUS shield.

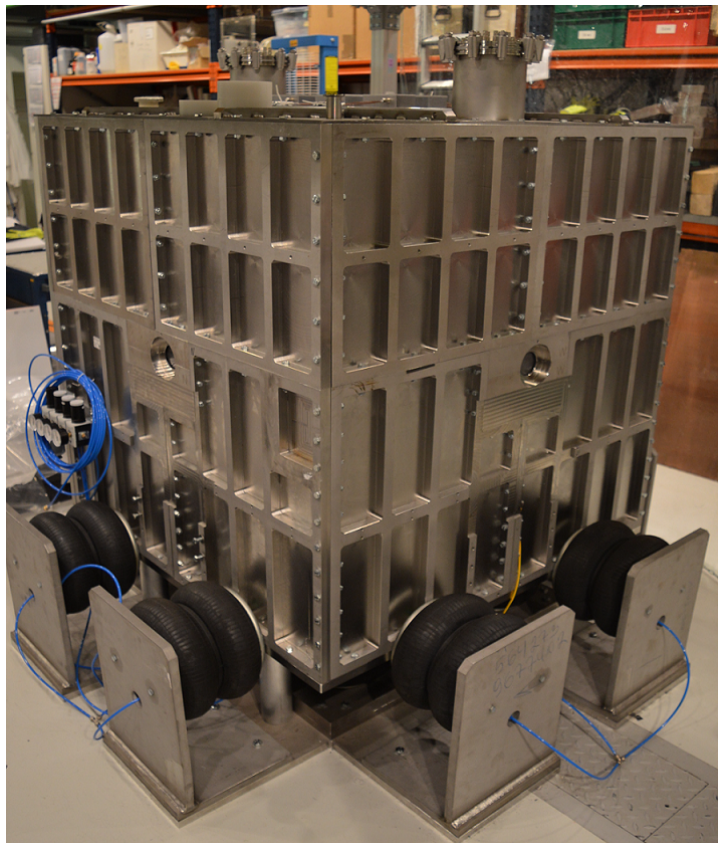


**Figure 4.8:** Image taken once the shield and cage was fully set up.

## 4.2.2 Measurement

During this time, various measurements were done, from which most were to set up the required measurement parameters, e.g. all the measurements for the muonveto set-up in chapter 3. Furthermore, the CONUS cage has to option to be flushed with  $N_2$ , to reduce radon and its daughter nuclides inside the detector chamber. At the beginning, this flushing system produced a lot of microphony, since the air-flow speed was too high and directly hit the cryostat of CONRAD. This system cannot be used later at the reactor site, but for the testing phase it helped speed up the measurement cycle. Because without the flushing one would have to wait for a couple days for all the Radon to decay. Once the muonveto system was tuned, the first longer measurements were conducted.

All the evaluation in this work, was done with Python<sup>1</sup>, where new scripts were created for calibrating, fitting and displaying energy spectra, as well as Lynx controlling scripts. Python was chosen, because its simplicity and direct support of the Lynx SDK. Moreover, it works platform independent, which makes collaboration work easier.

| <b>CONRAD</b>        |                             |                         |                       |
|----------------------|-----------------------------|-------------------------|-----------------------|
|                      | <b>Initial Duration [s]</b> | <b>Removed Time [s]</b> | <b>Final Time [s]</b> |
| <i>With Veto:</i>    |                             |                         |                       |
| 30.06.2017           | 234483                      | 0                       | <b>234483</b>         |
| 03.07.2017           | 78050                       | 0                       | <b>78050</b>          |
| 04.07.2017           | 7804                        | 0                       | <b>7804</b>           |
| 05.07.2017           | 396390                      | 7200                    | <b>389190</b>         |
| 10.07.2017           | 324620                      | 72000                   | <b>252620</b>         |
|                      |                             |                         | <b><u>962147</u></b>  |
| <i>Without Veto:</i> |                             |                         |                       |
| 04.07.2017           | 12778                       | 0                       | <b>12778</b>          |
| 04.07.2017           | 8762                        | 0                       | <b>8762</b>           |
| 05.07.2017           | 396400                      | 7200                    | <b>389200</b>         |
| 10.07.2017           | 324616                      | 28800                   | <b>295816</b>         |
|                      |                             |                         | <b><u>706556</u></b>  |

**Table 4.4:** Summary of the data files, which were used to create the final data set for Phase 1.

The measurements done with the Lynx, are saved as a time stamped list (TLIST), see section 2.3.3 for more details. The background data was combined, by just appending TLIST files for all the available background measurements. For the energy spectrum reconstruction, the time stamps can be ignored, hence the difference in

<sup>1</sup>Python Version 2.7.13

start times is not an issue. Prior to appending the TLIST files, one advantage of the TLIST format came into effect. This format makes an analysis for certain time frames possible. Therefore all the measurements were split into two hour frames, and the spectral data was inspected for irregularities. If a time frame was identified which contained a significantly different amount of events, the time window in question, was compared with work going on in the low-level laboratory during that time. If a logical explanation can be found, e.g. refilling of the dewar, work on the shield itself or heavy duty work in the laboratory these time frames were removed for the final analysis. Table 4.4 contains all the individual background measurements (with and without muon veto), which were combined for a final data product for phase 1. A more detailed list is presented in Appendix C.2, where a table is provided containing all the removed time windows. This kind of analysis can be done very easily with the TLIST format which is used throughout this thesis. Because one can easily create a subset of the whole measurement, by setting constraints for the time stamps of the events. For the final data product, two measurements had to be removed, because of an offset in the energy scale, due to a change in attenuation. With this final data set, the achieved background level evaluated; corresponding energy spectra are displayed in figure 4.9 and 4.10 with and without active muonveto respectively. For the final dataset, the mean deadtime over the whole duration is 0.26%.

### 4.2.3 Spectral Analysis

The result from the final data-set for phase 1 is summarized in the following two plots, containing the energy spectra with and without the active muonveto system. The used calibration is shown in figure C.3 where four peaks have been used to fit a polynomial of second order.

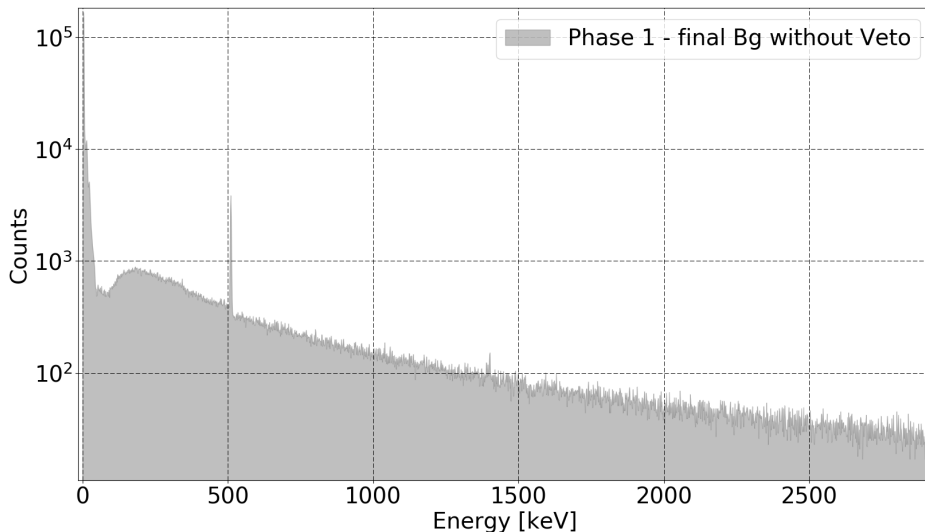


**Figure 4.9:** The energy spectrum containing all the files listed in table 4.4, with the deactivated muonveto.

The spectral count rate for certain energy ranges, is shown together with the final reduction rates in table 4.5. Both spectra do not show a high concentration of any impurities. Any other lines which could be present, are overlain by the muon-induced background. Figure 4.10 shows more details, because almost all the cosmic muon background has been removed by the muonveto. Prominently a small line at  $\sim 2615$  keV can be seen, which is due to a small impurity of  $\text{TI}^{208}$ . The corresponding rate is roughly  $(0.48 \pm 0.12) [\frac{cts}{kg \cdot day}]$  (estimated by counting the events). Additionally, lines from neutron captures in germanium are visible within the spectrum at 53,67, 140 and 198 keV respectively.

| Energy Range<br>[keV] | Count rates:<br>muonveto OFF $[\frac{cts}{kg \cdot day}]$ | Count rates:<br>muonveto ON $[\frac{cts}{kg \cdot day}]$ | Reduction $R_R$<br>[%] |
|-----------------------|-----------------------------------------------------------|----------------------------------------------------------|------------------------|
| 45 - 50               | $121.51 \pm 2.80$                                         | $3.40 \pm 0.40$                                          | 97.2                   |
| 45 - 100              | $1331.02 \pm 9.26$                                        | $72.62 \pm 1.85$                                         | 94.5                   |
| 100 - 500             | $11\,390.91 \pm 27.08$                                    | $330.54 \pm 3.95$                                        | 97.1                   |
| 520 - 2620            | $9972.23 \pm 25.33$                                       | $116.41 \pm 2.35$                                        | 98.8                   |
| 2620 - 2700           | $116.81 \pm 2.74$                                         | $0.71 \pm 0.18$                                          | 99.4                   |
| 45 - 2700             | $23\,765.49 \pm 39.11$                                    | $532.14 \pm 5.02$                                        | 97.8                   |
| 511                   | $[\frac{cts}{day}]$<br>$1174.48 \pm 23.96$                | $[\frac{cts}{day}]$<br>$11.90 \pm 1.03$                  | 99.0                   |

**Table 4.5:** The resulting background levels and reduction rates; recorded with the Ge detector CONRAD inside the CONUS shield.

### Germanium Lines

In the low energy range of the spectrum, multiple lines induced by neutron capture in the germanium are visible. These lines are created by muons in the innermost lead layer via (1.6). Due to their respective decay being much longer than the used window length of  $164 \mu\text{s}$ , the muonveto cannot remove them from the spectrum. The visible isotopes are shown in figure 4.11, the line strength was only be estimated by counting the events within the marked area. The resulting rates are given in table 4.6. The line strengths are in agreement with values measured with the similar GIOVE detector, except for the  $\text{Ge}^{71\text{m}}$  line intensity, which seems to be too high. This might be due to the approximate nature of the line strength estimation. Due to resolution issues, line intensities for the sum of two  $\text{Ge}^{73\text{m}}$  is compared, rather than the individual line strengths.

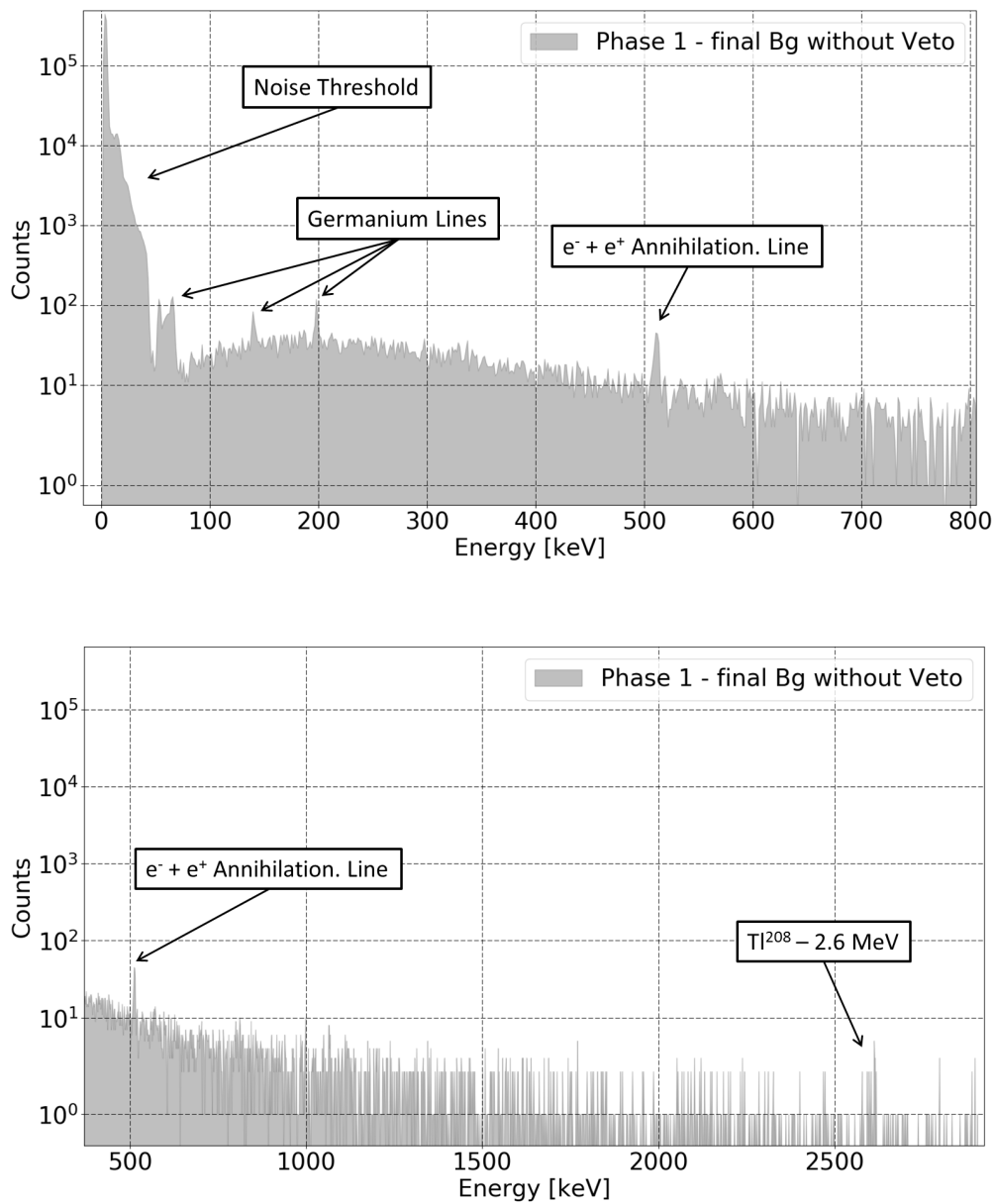


**Figure 4.10:** The energy spectrum containing all the files listed in table 4.4, with an active muonveto system. For better resolution it is split into two parts. The whole spectrum is shown in figure C.5.

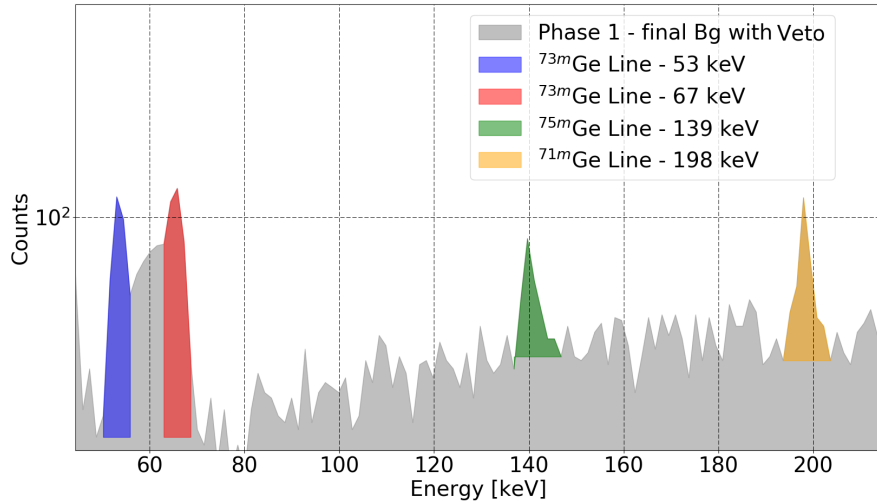


**Figure 4.11:** The energy spectrum with the marked germanium lines.

| Isotope/Isomer               | Energy<br>[keV] | Count rates:<br>CONRAD [ $\frac{cts}{day}$ ] | Count rates:<br>GIOVE [ $\frac{cts}{day}$ ] |
|------------------------------|-----------------|----------------------------------------------|---------------------------------------------|
| $Ge^{72}(n,\gamma) Ge^{73m}$ | 53.53           | $24.17 \pm 3.21$                             | $6.9 \pm 0.7$                               |
| $Ge^{72}(n,\gamma) Ge^{73m}$ | 66.59           | $31.98 \pm 3.08$                             | $51.4 \pm 5.7$                              |
| $Ge^{74}(n,\gamma) Ge^{75m}$ | 139.88          | $10.96 \pm 1.55$                             | $8.8 \pm 1.1$                               |
| $Ge^{70}(n,\gamma) Ge^{71m}$ | 198.3           | $17.34 \pm 2.47$                             | $9.5 \pm 0.8$                               |

**Table 4.6:** The measured Germanium lines with CONRAD, which are induced by cosmic radiation and the values obtained with GIOVE (Measurement ID: 0040)

#### 4.2.4 Comparison with GIOVE

As a further viability test, the background count rates received in this first phase of commissioning will be compared to values measured by GIOVE in the low-level laboratory. The two set-ups share many similarities (e.g. the onion like shield, similar muonveto system), hence the count rates should be comparable. The physical separation in the room is about 2 m and the overburden is not perfectly symmetric, but these should just be small effects. Due to the difference in the inner most layers of the passive radiation shield, the low energy suppression is different for CONUS. Since the CONUS shield has lead as innermost layer, where GIOVE uses copper, this means the bremsstrahlung suppression is different for the two set-ups. Where lead produces more bremsstrahlung due to the  $Z^2$  proportionality of the bremsstrahlung, but the self shielding goes with  $Z^5$ , so the lead offers a better shielding at low energies. Which is reflected in the lower count rates in the energy range below 500 keV for the spectra without muon veto (see tables 4.5 and 4.7). The difference in veto efficiencies for the same energy range cannot yet be

explained. One possible explanation could be a contamination with  $\text{Pb}^{210}$ .

| Energy Range<br>[keV] | Count rates:<br>muonveto OFF                                      | Count rates:<br>muonveto ON                                    | Reduction $R_R$<br>[%] |
|-----------------------|-------------------------------------------------------------------|----------------------------------------------------------------|------------------------|
| 40 - 50               | $429.07 \pm 5.89$                                                 | $4.26 \pm 0.31$                                                | 99.0                   |
| 40 - 100              | $5444.17 \pm 20.97$                                               | $84.70 \pm 1.37$                                               | 98.4                   |
| 100 - 500             | $15\,466.60 \pm 35.37$                                            | $138.39 \pm 1.75$                                              | 99.1                   |
| 520 - 2620            | $9290.87 \pm 27.42$                                               | $109.46 \pm 1.55$                                              | 98.8                   |
| 2620 - 2700           | $109.13 \pm 2.97$                                                 | $0.57 \pm 0.11$                                                | 99.5                   |
| 40 - 2700             | $31\,128.40 \pm 50.18$                                            | $347.58 \pm 2.77$                                              | 98.9                   |
| 511                   | $\left[\frac{\text{cts}}{\text{day}}\right]$<br>$1112.9 \pm 17.1$ | $\left[\frac{\text{cts}}{\text{day}}\right]$<br>$19.3 \pm 3.1$ | 98.3                   |

**Table 4.7:** GIOVE count rate (in  $\left[\frac{\text{cts}}{\text{kg}\cdot\text{day}}\right]$  if not stated otherwise) measured with an empty sample chamber (Measurement ID: 0080 (no muonveto) and 0040 (with muonveto)).

| Energy Range<br>[keV] | GIOVE<br>Reduction [%] | CONRAD<br>Reduction [%] | Difference<br>[%] |
|-----------------------|------------------------|-------------------------|-------------------|
| 45 - 50               | 99.0                   | 97.2                    | -1.8              |
| 45 - 100              | 98.4                   | 94.5                    | -3.9              |
| 100 - 500             | 99.1                   | 97.1                    | -2.0              |
| 520 - 2620            | 98.8                   | 98.8                    | 0.0               |
| 2620 - 2700           | 99.5                   | 99.4                    | -0.1              |
| 45 - 2700             | 98.9                   | 97.8                    | -1.1              |
| 511                   | 98.3                   | 99.0                    | +0.7              |

**Table 4.8:** Reduction rates in various energy ranges of CONRAD and GIOVE.

## 4.2.5 Results

Phase 1 of the CONUS experiment has been successful: the muonveto system was set up and the first background measurements were taken. The final count rates are presented in table 4.5 as well the obtained spectra are shown in figures 4.9 and 4.10. The obtained background reduction values due to the muonveto system within specification and close to the values obtained with the GIOVE set-up. For the following phases the muonveto system is optimize able. In general the count rates are comparable to the values measured with GIOVE in the same room, only the energy 100-500 keV is different for both set-ups. A possible reason for this can be a still persisting  $\text{Pb}^{210}$  contamination in a few lead bricks used in the innermost layer of the passive shield. The lead bricks for the innermost layer were created from old and pure lead, but for three lead bricks, excess material

had to be remelted which could have resulted in their contamination. This would create a beta-continuum which peaks at about 170 keV and be an explanation for the difference in count rates.

## 4.3 Phase 2

The second phase of the CONUS experiment started on the 17<sup>th</sup> of July and is not yet concluded as of writing this thesis<sup>2</sup>.

### 4.3.1 Goals and Changes

There are two main goals for the second phase: testing new lead bricks in the context of  $\text{Pb}^{210}$  contamination in the innermost layer of the shield, commissioning one of the new CONUS detectors, as well as a neutron source measurement with  $\text{Cf}^{252}$ . The latter is planned in order to analysis the detectros's behaviour near its threshold, by activating the Ge and observing the decay of its isotopes.

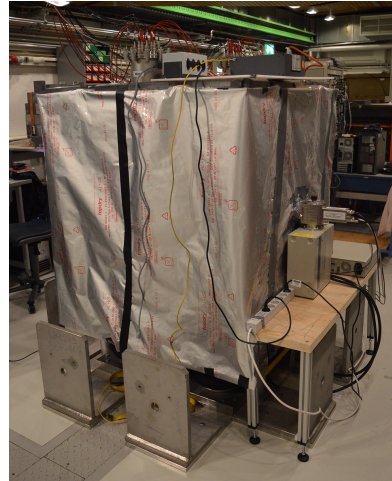
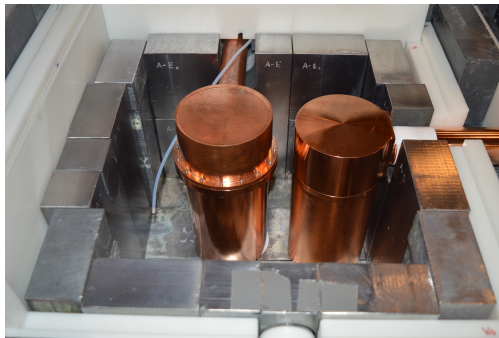


**Figure 4.12:** Left: View into the innermost layer of the CONUS shield with two detectors CONRAD (left) and one CONUS detector (right).

Right: An outside view onto the CONUS shield without the steel cage, instead foil was used as light and radon protection.

For this phase the shield of the CONUS experiments has to be partly dismantled in order to insert one of the CONUS detector into it. For phase 2 not only a second detector was put into the shield, but the steel cage had to be removed due to necessary construction work. Therefore the experiment temporarily lost its shield against inflowing air. To prevent airborne radon from streaming into the shield, it was wrapped with multiple layers of foil. The outermost layer is non-transparent to prevent light triggering the scintillator plates. This could lead to problems for

<sup>2</sup>August 31<sup>st</sup> 2017



the muonveto system since ambient light can induce a strong offset of the PMT signal. This would render the threshold settings useless and the muonveto system would not work correctly any more. The new outside layer is shown on the right side of figure 4.12.

### 4.3.2 Measurements

The main difference to phase 1 is the missing steel cage as well as several different lead bricks in the innermost layer of the shield and an additional detector. The main problem is radon contamination, because the foil wrap around the lead layers cannot fully prevent a radon contamination. Therefore an additional N<sub>2</sub>-flush is used to create a small excess pressure which guarantees air flow out of the shield. Since phase 2 of commissioning is not yet finished as of writing this thesis, only preliminary results are presented. The performed background measurements with CONRAD are listed in table 4.9 which will be used for a spectral analysis. The measurements were taken during the summer break, which meant there was barely any work performed inside the low-level laboratory and the measurements conducted were not influenced by microphony like it phase 1. In between the conducted background measurements, short synchronization tests were conducted to further test different methods for section 3.5.2.

Furthermore, some test measurements with the CONUS detector were conducted to analyse its energy range and general performance. Later on, background measurements were started.

| <b>CONRAD</b>        |                             |                         |                       |
|----------------------|-----------------------------|-------------------------|-----------------------|
|                      | <b>Initial Duration [s]</b> | <b>Removed Time [s]</b> | <b>Final Time [s]</b> |
| <i>With Veto:</i>    |                             |                         |                       |
| 28.07.2017           | 233523                      | 0                       | <b>233523</b>         |
| 04.08.2017           | 415905                      | 0                       | <b>415905</b>         |
| 10.08.2017           | 498873                      | 0                       | <b>498873</b>         |
| 16.08.2017           | 106639                      | 0                       | <b>106639</b>         |
| 18.08.2017           | 260012                      | 0                       | <b>260012</b>         |
| 22.08.2017           | 54211                       | 0                       | <b>54211</b>          |
| 24.08.2017           | 81121                       | 0                       | <b>81121</b>          |
|                      |                             |                         | <b><u>1560284</u></b> |
| <i>Without Veto:</i> |                             |                         |                       |
| 31.07.2017           | 68592                       | 0                       | <b>68592</b>          |
| 01.08.2017           | 227390                      | 0                       | <b>227390</b>         |
| 21.08.2017           | 54104                       | 0                       | <b>54104</b>          |
|                      |                             |                         | <b><u>350086</u></b>  |

**Table 4.9:** Summary of the data files, which were used to create a preliminary data set for phase 2.

### 4.3.3 Spectral Analysis

Since this measurement phase is not yet concluded, the last measurement which is included in this analysis was started on the 24<sup>th</sup> of August. All the used measurements are shown in table 4.9. With these a combined measurement was created, all files used the calibration shown in figure C.4. Like in phase 1, the spectral count rates are calculated and shown in table 4.10. Although a lot of effort was put into creating a substitute shield for the missing steel cage, the spectrum in contaminated with spectral lines mainly induced by airborne radiation. The spectrum without an active muonveto in figure 4.13, is almost identical to the background spectrum from phase 1, since the background induced by cosmic radiation is much more dominant, than the one induced by natural radioactivity. Because of airborne radon contamination and potentially other new background components, several gamma-lines are visible, which was not the case in phase 1. The more prominent lines have been marked in the plots of figure 4.14 (in the overlap area, lines were only marked in one of the two plots). Most of these lines can be attributed to the decay chains of  $\text{Th}^{232}$ ,  $\text{U}^{238}$  and  $\text{R}^{222}$  which are present in the air in the laboratory. In addition  $\text{K}^{40}$  and  $\text{Bi}^{207}$  can be seen in the spectrum, which might hint towards a new contamination.

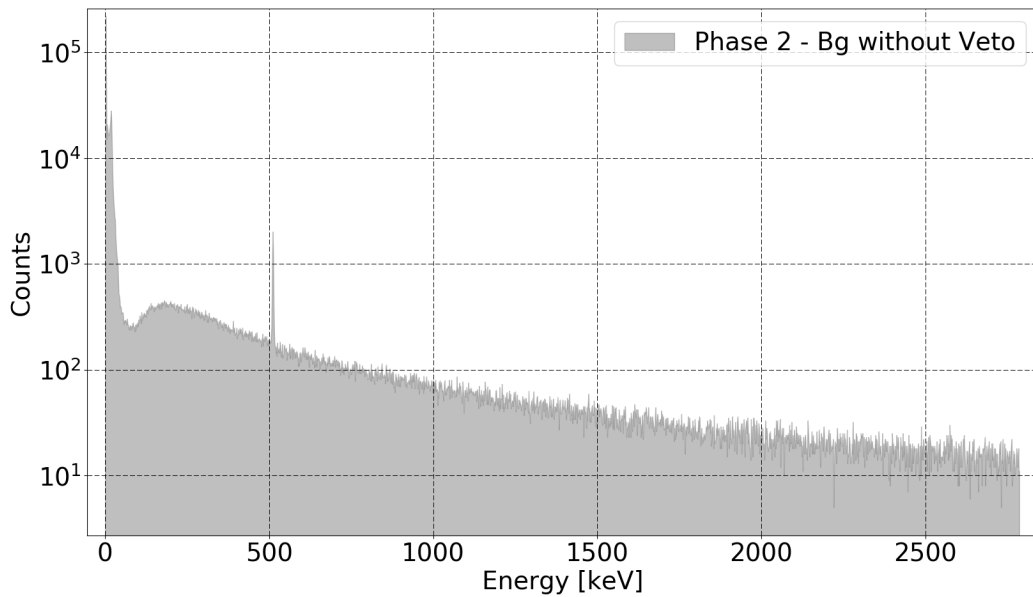


**Figure 4.13:** The energy spectrum containing all the files listed in table 4.9. Measurements were performed with deactivated muonveto.

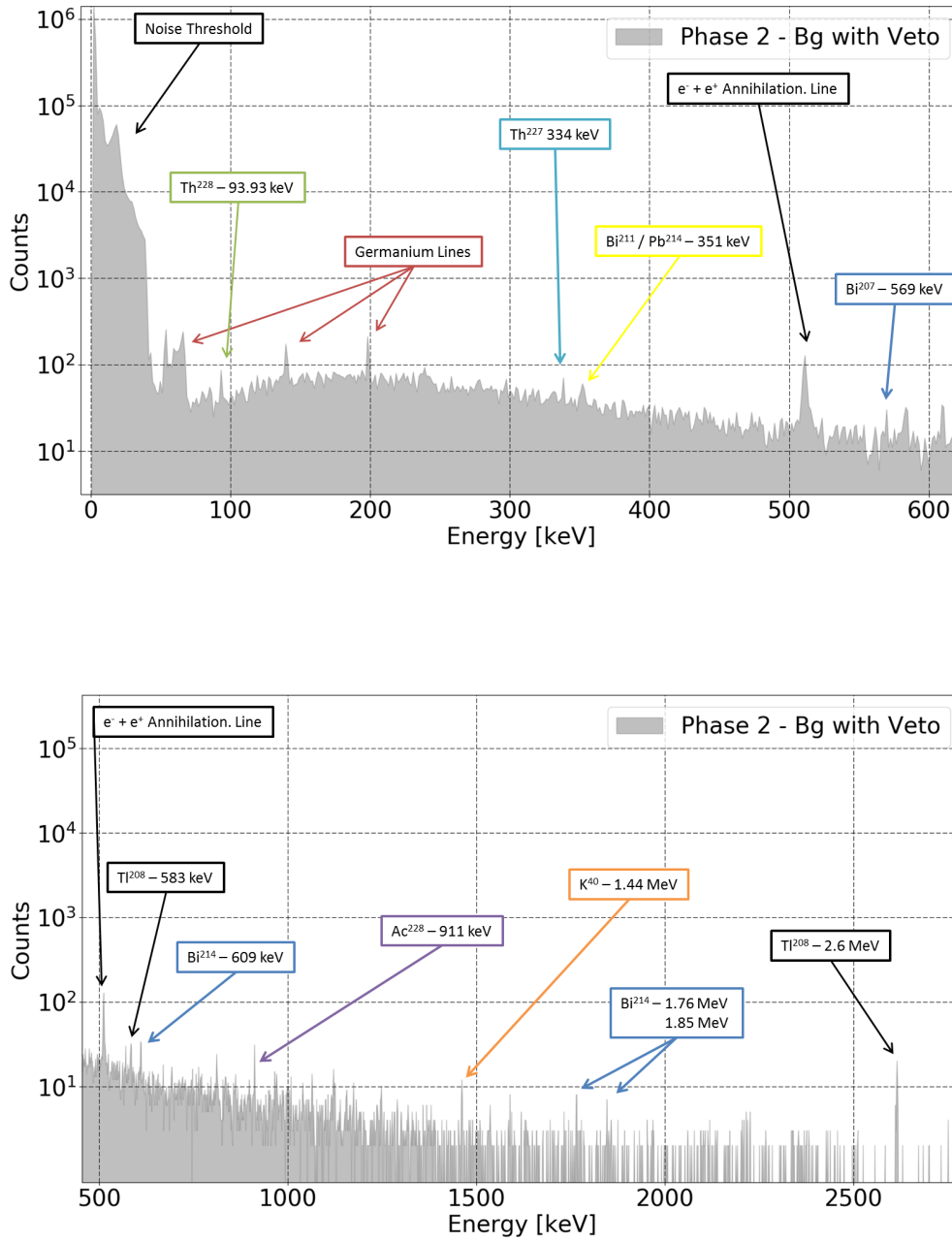


**Figure 4.14:** The energy spectrum containing all the files listed in table 4.9. Measurements were performed with activated muonveto. For better resolution it is split into two parts. The whole spectrum is shown in figure C.6.

| Energy Range<br>[keV] | Count rates:                                |                                            | Reduction $R_R$<br>[%] |
|-----------------------|---------------------------------------------|--------------------------------------------|------------------------|
|                       | muonveto OFF [ $\frac{cts}{kg \cdot day}$ ] | muonveto ON [ $\frac{cts}{kg \cdot day}$ ] |                        |
| 45 - 50               | $185.88 \pm 4.91$                           | $5.65 \pm 0.40$                            | 97.0                   |
| 45 - 100              | $1488.70 \pm 13.91$                         | $84.18 \pm 1.52$                           | 94.3                   |
| 100 - 500             | $11\,673.43 \pm 38.94$                      | $381.50 \pm 3.24$                          | 96.7                   |
| 520 - 2620            | $9827.66 \pm 35.73$                         | $152.82 \pm 2.05$                          | 98.4                   |
| 2620 - 2700           | $114.70 \pm 3.86$                           | $0.61 \pm 0.13$                            | 99.5                   |
| 45 - 2700             | $24\,057.76 \pm 55.90$                      | $634.34 \pm 4.18$                          | 97.3                   |
| 511                   | $1130.83 \pm 16.71$                         | $12.69 \pm 0.82$                           | 98.9                   |

**Table 4.10:** Preliminary background levels and the corresponding reduction rates for the phase 2; recorded with the Ge detector CONRAD inside the CONUS shield.

## Germanium Lines

Like in previous phase, the activated germanium lines can be observed well. Since they are not affected by the changes made. The approximate count rates of the individual lines are shown in table 4.11. The values obtained from phase 2 are in agreement with the values obtained with GIOVE (see table 4.6). The used analysis method is the same as in phase 1.

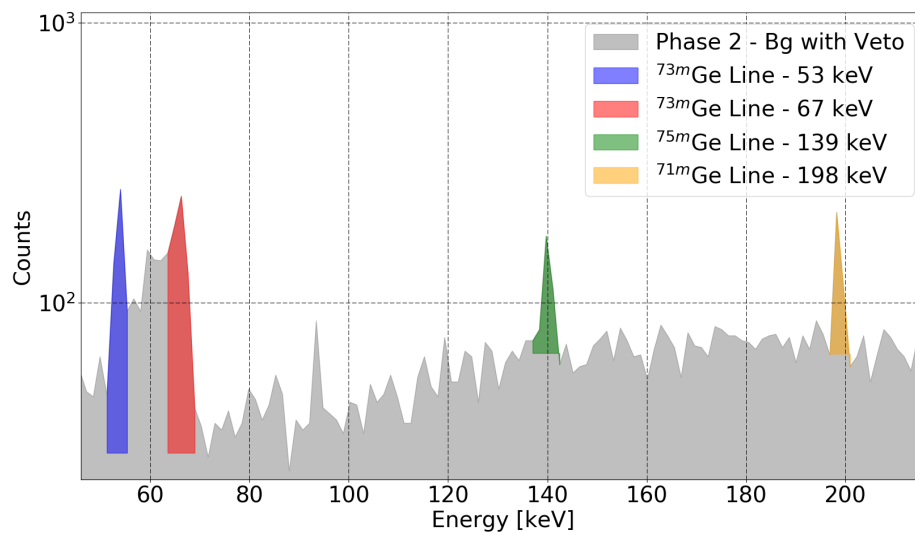


**Figure 4.15:** The energy spectrum for phase 2 with the marked germanium lines.

| Isotope/Isomer                                    | Energy<br>[keV] | Count rates:<br>[ $\frac{cts}{day}$ ] |
|---------------------------------------------------|-----------------|---------------------------------------|
| Ge <sup>72</sup> (n, $\gamma$ ) Ge <sup>73m</sup> | 53.53           | 21.78 $\pm$ 4.03                      |
| Ge <sup>72</sup> (n, $\gamma$ ) Ge <sup>73m</sup> | 66.59           | 31.51 $\pm$ 3.45                      |
| Ge <sup>74</sup> (n, $\gamma$ ) Ge <sup>75m</sup> | 139.88          | 8.82 $\pm$ 2.12                       |
| Ge <sup>70</sup> (n, $\gamma$ ) Ge <sup>71m</sup> | 198.3           | 9.74 $\pm$ 3.17                       |

**Table 4.11:** Cosmic radiation induced Germanium lines measured with CONRAD.

#### 4.3.4 Results and Comparison with Phase 1

Since phase 2 is not yet concluded, only preliminary results can be discussed. Due to the difference of the outermost part of the shield being absent, the spectra show clear differences. Due to the contamination with airborne radioactivity which streamed inside the CONUS shield, many spectral lines appear in the energy spectrum shown in figure 4.14. So lines can be explained by the missing steal cage which results in ambient air flowing into the shielding where radon settles on the surface of the cryostats of the detectors and decays. Radon is present in many elements (e.g. the cement) from where it can diffuse into the ambient air which is especially a problem for poorly ventilated room like the low-level laboratory. This can explain some of the seen spectral lines but lines like the K<sup>40</sup> mean there is a new contamination inside the shield. The Bi<sup>207</sup> line can not be easily explained since it usually not found in the environment. Although, when comparing the individual measurement from the beginning of phase 2 and the last measurement used of phase 2, a decrease in line strength is evident as shown in figure 4.16 which indicates a slightly decreased contribution from airborne contaminations. This means the final measurements of phase 2 a less contaminated spectrum is possible. This final measurement can then be analysed into further detail concerning the changed lead bricks, the second detector inside the shield and the contaminations from K<sup>40</sup> and Bi<sup>207</sup>. Since the sum of all the induced spectral lines makes an exact analysis difficult.

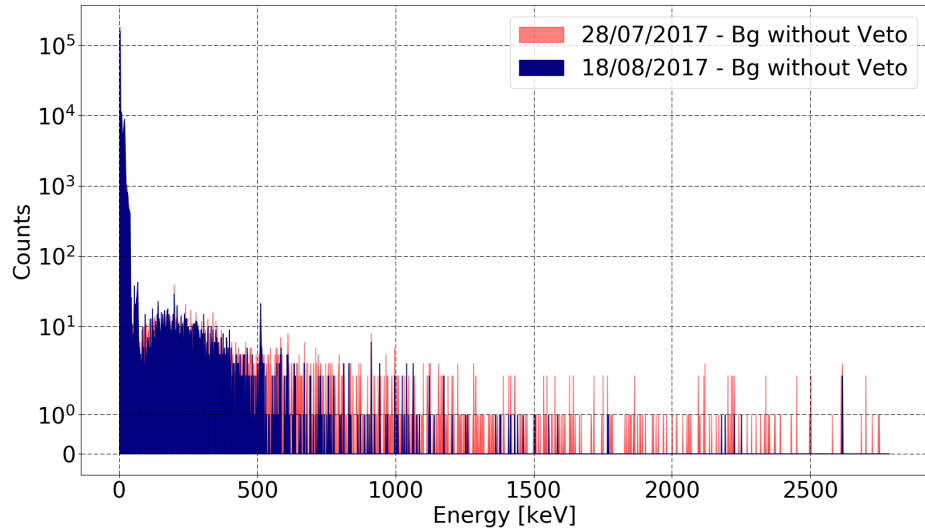


**Figure 4.16:** The compared energy spectra from the beginning and middle of phase 2.

The count rate comparison of tables 4.5 and 4.10 indicates an increase in count rates for the spectrum without muon veto below 500 keV, whereas the count rates above are comparable. The same is true for the count rates in the spectrum with muon veto system active, since the reduction rate  $R_R$  did not change significantly. Hence, the efficiency of the muon veto did not change from phase 1 to phase 2. The main reason for the higher count rates are the abundance of progenitors from the natural decays. This problem was not evident for phase 1 with an air tight steel cage. Since the preliminary data product is too contaminated with products from natural decays, the effect of the new lead bricks cannot be determined at this point. Furthermore, as previously mentioned, all results for the new CONUS detector will not be discussed within the scope of this thesis. Last but not least, due to problems with obtaining a suitable  $\text{Cf}^{252}$  source, this measurement has not yet started.

# 5 Conclusion and Outlook

The goal of this thesis was to perform various steps required to test the shielding of the CONUS experiment. By also participating in the whole commissioning process, the set-up could be brought into its final testing phase. In the following all performed steps and their outcome shall be summarized.

## 5.1 Muonveto System

The first aspect of the set-up process was installing the muonveto system for the CONUS experiment. A muonveto system is required because the coherent elastic neutrino nucleus scattering (CE $\nu$ NS) signal remains covered by background events in the measured spectra without an active suppression of the cosmic induced background (see section 1.2). With the experience from previous detector constructions (see section 1.2.2) the shield for the CONUS experiment was designed at MPIK. The veto system is utilizing plastic scintillator plates to detect the incoming muons. The energy deposited in the scintillator material according to (1.2) results in light emission which is detected with 20 photomultiplier tubes. These scintillator plates are located around the detectors such that they provide a good coverage from incoming muons. They follow a  $\cos^2$ -distribution, which means most of the muons will hit the shield from above [16]. After the shield's commissioning, the muonveto was tuned for optimal thresholds and window lengths (see sections 3.4.1 and 3.4.2). The obtained setting is 164  $\mu$ s for the window length and the thresholds are given in table B.1.

The results above achieved a reduction of 97.7% in an energy range from 45-2700 keV and are already very promising, but still have potential for further improvements. The goal was to reach reduction values comparable to the GIOVE set-up (see section 1.2.2), which is located in the same laboratory and uses a similar muonveto. The achieved values match the GIOVE values above 500 keV (see table 4.8), but below 500 keV the veto efficiency is considerably lower than the GIOVE reduction. One explanation are Pb<sup>210</sup> impurities in the innermost lead layers, which introduce a  $\beta$ -spectrum with its maximum at 170 keV [16]. Further reasons for this problem are currently under investigation.

The second aspect was the suggested potential upgrade of the current muonveto system (see section 3.5) by introducing a pulse shape analysis. By analysing the shape of muon-induced signals, background components with longer decay times can be removed and a background level with less unwanted spectral lines can be achieved. During the performed work, two methods relying on the used DAQ (Lynx) were considered. The ideal implementation of the upgrade, is doing a pulse

shape analysis of the PMT signals, which the Lynx does not support. The available option for the upgrade implementation, was to test the internal digital oscilloscope function, which unfortunately does not work fast enough to be a viable analysing tool for the PMT signals. The second tested approach, where by recording synchronized spectra timestamps of each incident event, an offline muonveto system could be implemented. By analysing the spectral components in detail and applying corresponding time cuts for the germanium energy data, the muon efficiency can in principle be improved. Due to problems, with the synchronisation and the used acquisition mode, this could not be tested in detail. Since the Lynx is a plug and play system, it does not offer much support for individual solutions and hence frequent contact with the development team of the Lynx was required. Therefore software scripts for all the measurements were developed and thoroughly tested, which was a very time consuming task. Furthermore, the initial set-up process of the data acquisition for the measurements (e.g. finding the best settings) had to be done and demanded multiple iterations and tests.

The tested methods have the potential to improve the background reduction from muons even more, but the technical implementation still is problematic and could not be fully implemented in the scope of this thesis. One step to implement the needed functionality, would be working together with the Lynx development team and implement the appropriate functionalities for the Lynx. Otherwise, different options for DAQ systems have to be investigated and a possible change of systems has to be considered.

## **5.2 Commissioning of the CONUS Shield**

The CONUS shield was tested in two measurement phases so far, with a third phase still to come. The first part was the assembly of the whole shielding during which many steps were taken to prevent contaminations due to material impurities. All materials very close to or in the detector have been screened at MPIK as well as the Laboratori Nazionali del Gran Sasso (LNGS). Furthermore, the individual components, like the lead bricks have been cleaned thoroughly with isopropanol to remove impurities from its surface, which could introduce additional background. The shield was designed to suppress various background components (see 1.1): The outermost steel shell prevents radon contamination and the inner layers shield against the ambient natural radiation as well as background induced by cosmic radiation. To shield against neutrons, absorber material (borated polyethylene plates) is inserted in between the lead layers. This is due to the fact that there are not only neutrons from outside sources, but the incident muons can create additional neutrons within the lead via (1.6). Hence two layers of neutron absorbers are used. The last important aspect for the CONUS shield is the age of the innermost lead layer since lead contains an unstable isotope  $\text{Pb}^{210}$ , which has a half-life time of approximately 22 years. This isotope decays and creates additional beta background, which cannot be removed. A technically easy method is using very old lead, where the  $\text{Pb}^{210}$  has already decayed. The final onion-like structure of the shield can be seen in figure 2.7. Initially a semi-coaxial high pu-



rity Ge detector (CONRAD) was used for the first phase of measurements inside the CONUS shield. To characterize CONRAD its active volume/mass was measured, since this value is needed for a correct normalization of spectral count rates. This showed (see section 4.2), that the active mass decreased from 2.2 kg down to 1.94 kg, which corresponds to a current active volume of 79 %. This decrease is attributed to lithium (in the dead layer) drifting further into the detector. Furthermore, a high voltage scan was conducted to verify the used supply voltage. To ensure optimal operating performance of a germanium detector, its supply voltage must be well above its depletion voltage. The measured value for the depletion voltage of CONRAD is  $2439 \pm 66$  V, which is well below the current supply voltage of 3500 V and thus in agreement with the used value.

Afterwards measurements to quantify the achieved background levels were conducted in two phases. During the first phase only one detector (CONRAD) was inside the CONUS shield. The results of the first phase are shown in table 4.5 and should be comparable to the achievable background levels at the nuclear power plant in Brokdorf, where the final location of CONUS will be. The spectrum does not show any unexpected spectral lines, but the obtained veto efficiency in the low energy range ( $< 500$  keV) is lower than expected. One reason is the previously mentioned  $\text{Pb}^{210}$  contamination. To investigate this problem, during the second phase of measurements several different lead bricks will be used in the innermost layer to see whether a difference can be observed. The second phase is still in progress as of writing this thesis. Therefore only preliminary results can be discussed. For this phase, a few changes were made. First of all, the outer steel cage had to be removed for further construction tests, which meant the shield is no longer airtight. An additional detector (the first CONUS detector) was inserted into the shield together with CONRAD. The results and measurements with this second detector however, are not discussed in the scope of this thesis, since details about the detectors properties have not been published yet. On an interim basis, the shield was covered with foil, as well as a stronger  $\text{N}_2$  - flush was implemented in order to prevent ambient air to stream into the shield (shown in figure 4.12). The background energy spectra obtained during the second phase (see table 4.10) were contaminated with a lot of isotopes from natural radioactivity, because radon was able to stream into the shield. This contamination made a further analysis of  $\text{Pb}^{210}$  impossible at this point. With the final data set of phase 2, the reason for the lower muonveto efficiency might be identified. Conclusively, at the end of phase 2 a measurement with a  $\text{Cf}^{252}$  source is planned, which will give important information about the behaviour of the CONUS detector near its threshold.

### Phase 3

As the last step for the commissioning phase, a third measurement phase is planned. The goal is to measure the neutron suppression which can be achieved with the CONUS shield. Therefore the Metrology Institute of Germany (PTB Braunschweig) will supply an accurate neutron detector, which will be inserted into the CONUS shield and the neutron suppression will be measured. This will

be vital information since the neutron flux from the reactor in Brokdorf will be higher than the neutron rate observed in the low-level laboratory at MPIK.

### 5.3 Future of CONUS and Potential of CENNS

Once the commissioning phase and all the tests are completed and all test are completed, the experiment has to be moved and assembled at the reactor site in Brokdorf. The current schedule sets the start of data acquisition still within 2017. Furthermore, the introduced upgrade for the muonveto might be realized, if a task-force with CANBERRA can be established for this specific problem or a different data acquisition unit will be used for later stages of the experiment. The main goal for CONUS is the detection of the coherent elastic neutrino nucleus scattering as a proof of principle. If successful, the germanium technology in principle supports an up-scaling to higher detector masses so that precision measurements can be done and MPIK has has a history with germanium and low-background experiments (e.g. GALLEX [38], GERDA [6], Heidelberg-Moscow collaboration [39]). These precision measurements of  $CE\nu NS$  will be vital for improving the knowledge we have about the standard model (SM) and beyond it e.g. by providing precision measurements of the Weinberg angle  $\theta_W$ . Deviations from the SM predictions can also be interpreted in term of non-standard neutrino interactions. An upscaled version of CONUS could compete with DUNE in this context [40]. Measurements of the cross section will help to understand processes inside supernovae better by providing accurate measurements of the  $CE\nu NS$  cross section [41].

*So long, and thanks for all the fish.*

# Bibliography

- [1] W. Pauli, “Dear radioactive ladies and gentlemen,” *Phys. Today*, vol. 31N9, p. 27, 1978.
- [2] F. Reines and C. L. Cowan, “The neutrino,” *Nature*, vol. 178, pp. 446–449, 1956.
- [3] Q. R. Ahmad *et al.*, “Direct evidence for neutrino flavor transformation from neutral current interactions in the Sudbury Neutrino Observatory,” *Phys. Rev. Lett.*, vol. 89, p. 011301, 2002.
- [4] T. Kajita, E. Kearns, and M. Shiozawa, “Establishing atmospheric neutrino oscillations with super-kamiokande,” *Nuclear Physics B*, vol. 908, pp. 14 – 29, 2016. Neutrino Oscillations: Celebrating the Nobel Prize in Physics 2015.
- [5] B. Pontecorvo, “Mesonium and anti-mesonium,” *Sov. Phys. JETP*, vol. 6, p. 429, 1957. [*Zh. Eksp. Teor. Fiz.*33,549(1957)].
- [6] V. D’Andrea *et al.*, “First Results of Gerda Phase II,” *PoS*, vol. NOW2016, p. 098, 2017.
- [7] N. Abgrall *et al.*, “The Majorana Demonstrator Neutrinoless Double-Beta Decay Experiment,” *Adv. High Energy Phys.*, vol. 2014, p. 365432, 2014.
- [8] J. Ouellet, “Results and Status from KamLAND-Zen,” *PoS*, vol. ICHEP2016, p. 492, 2016.
- [9] C. Licciardi, “Recent Results and Status of EXO-200 and the nEXO Experiment,” *PoS*, vol. ICHEP2016, p. 494, 2016.
- [10] A. Osipowicz *et al.*, “KATRIN: A Next generation tritium beta decay experiment with sub-eV sensitivity for the electron neutrino mass. Letter of intent,” 2001.
- [11] J. R. Wilson, “Coherent Neutrino Scattering and Stellar Collapse,” *Phys. Rev. Lett.*, vol. 32, pp. 849–852, 1974.
- [12] D. Z. Freedman, “Coherent neutrino nucleus scattering as a probe of the weak neutral current,” *Phys. Rev.*, vol. D9, pp. 1389–1392, 1974.
- [13] D. Akimov *et al.*, “Observation of coherent elastic neutrino-nucleus scattering,” *Science*, 2017.

- [14] S. Kerman, V. Sharma, M. Deniz, H. T. Wong, J. W. Chen, H. B. Li, S. T. Lin, C. P. Liu, and Q. Yue, “Coherency in Neutrino-Nucleus Elastic Scattering,” *Phys. Rev.*, vol. D93, no. 11, p. 113006, 2016.
- [15] V. Belov *et al.*, “The GeN experiment at the Kalinin Nuclear Power Plant,” *JINST*, vol. 10, no. 12, p. P12011, 2015.
- [16] G. Heusser, “Low-radioactivity background techniques,” *Annual Review of Nuclear and Particle Science*, vol. 45, no. 1, pp. 543–590, 1995.
- [17] G. Heusser, M. Weber, J. Hakenmüller, M. Laubenstein, M. Lindner, W. Maneschg, H. Simgen, D. Stolzenburg, and H. Strecker, “GIOVE - A new detector setup for high sensitivity germanium spectroscopy at shallow depth,” *Eur. Phys. J.*, vol. C75, no. 11, p. 531, 2015.
- [18] G. F. Knoll, *Radiation detection and measurement*. Hoboken, NJ: Wiley, 2nd ed. ed., 1989.
- [19] M. Salathe, “Study on modified point contact germanium detectors for low background applications.” Dissertation, 2015. Dissertation at MPIK Heidelberg, 2015.
- [20] W. R. Leo, *Techniques for nuclear and particle physics experiments*. Berlin ; Heidelberg [u.a.]: Springer, 2., rev. ed. ed., 1994.
- [21] J. Lindhard and M. Scharff, “Energy Dissipation by Ions in the keV Region,” *Phys. Rev.*, vol. 124, pp. 128–130, 1961.
- [22] J. Hakenmüller, “The conus experiment - coherent elastic neutrino nucleus scattering.” Conference Talk, 2017. Held at TAUP Sudbury, July 27th 2017.
- [23] T. Rink, “Coherent elastic neutrino nucleus scattering - first detection and future potential.” Talk, 2017. Held at Scientific Advisory Board at MPIK Heidelberg, April 5th 2017.
- [24] W. Maneschg, “Coherent neutrino scattering.” Talk, 2017. The Future of Neutrino Physics <https://www.mpi-hd.mpg.de/neutrinos/>, at the MPIK Heidelberg, February 2017.
- [25] M. Lindner, “Suche nach anderen seltenen Ereignissen.” Talk, 2016. Strategiemeeting of the Komitee Für Astroteilchenphysik (KAT) [http://www.astroteilchenphysik.de/Sitzungen\\_&\\_Veranstaltungen\\_files/KAT-Strategietreffen\\_Nov\\_2016.html](http://www.astroteilchenphysik.de/Sitzungen_&_Veranstaltungen_files/KAT-Strategietreffen_Nov_2016.html), Physikzentrum Bad Honnef, November 2016.
- [26] L. et al., “The CONUS Experiment,” in prep.
- [27] A. Drukier and L. Stodolsky, “Principles and applications of a neutral-current detector for neutrino physics and astronomy,” *Phys. Rev. D*, vol. 30, pp. 2295–2309, Dec 1984.

- 
- [28] M. Thomson, *Modern particle physics*. Cambridge [u.a.]: Cambridge University Press, 2013.
- [29] D. Barker and D. M. Mei, “Germanium Detector Response to Nuclear Recoils in Searching for Dark Matter,” *Astropart. Phys.*, vol. 38, pp. 1–6, 2012.
- [30] P. GmbH, “Brokdorf nuclear power plant.” <https://www.preussenelektra.de/pe-internet/Kraftwerk-Brokdorf-266.htm>, 2017. Site checked on the 30th of August 2017.
- [31] N. Haag, A. Gütlein, M. Hofmann, L. Oberauer, W. Potzel, K. Schreckenbach, and F. M. Wagner, “Experimental determination of the antineutrino spectrum of the fission products of  $^{238}\text{U}$ ,” *Phys. Rev. Lett.*, vol. 112, p. 122501, Mar 2014.
- [32] P. Huber, “Determination of antineutrino spectra from nuclear reactors,” *Phys. Rev. C*, vol. 84, p. 024617, Aug 2011.
- [33] M. T. (Canberra, “Lynx - Digital Signal Analyzer.” [http://www.canberra.com/products/radiochemistry\\_lab/pdf/Lynx-SS-C38658.pdf](http://www.canberra.com/products/radiochemistry_lab/pdf/Lynx-SS-C38658.pdf). Site checked on the 30th of August 2017.
- [34] D. Stolzenburg, “Charakterisierung von plastikszintillatoren für das myonveto eines neuen gamma-spektrometers (giove).” Bachelor Thesis, 2011. Bachelor Thesis at MPIK Heidelberg, 2011.
- [35] Audi, G. and Bersillon, O. and Blachot, J. and Wapstra, A. H., “The NUBASE evaluation of nuclear and decay properties,” *Nuclear Physics A*, vol. 729, pp. 3–128, Dec. 2003.
- [36] H. V. Klapdor-Kleingrothaus, L. Baudis, A. Dietz, G. Heusser, B. Majorovits, and H. Strecker, “GENIUS-TF: A Test facility for the GENIUS project,” *Nucl. Instrum. Meth.*, vol. A481, pp. 149–159, 2002.
- [37] L.-L. CEA, LIST, “Table of radionuclides.” [http://www.nucleide.org/DDEP\\_WG/DDEPdata.htm](http://www.nucleide.org/DDEP_WG/DDEPdata.htm), 2017. Site checked on the 5th of August 2017.
- [38] T. A. Kirsten, “GALLEX solar neutrino results and status of GNO,” *Nucl. Phys. Proc. Suppl.*, vol. 77, pp. 26–34, 1999.
- [39] A. M. Bakalyarov, A. Ya. Balysh, S. T. Belyaev, V. I. Lebedev, and S. V. Zhukov, “Results of the experiment on investigation of Germanium-76 double beta decay: Experimental data of Heidelberg-Moscow collaboration November 1995 - August 2001,” *Phys. Part. Nucl. Lett.*, vol. 2, pp. 77–81, 2005. [Pisma Fiz. Elem. Chast. Atom. Yadra2005,no.2,21(2005)].
- [40] M. Lindner, W. Rodejohann, and X.-J. Xu, “Coherent Neutrino-Nucleus Scattering and new Neutrino Interactions,” *JHEP*, vol. 03, p. 097, 2017.
- [41] K. Scholberg, “Cross Section Measurements for Supernova Neutrinos,” *JPS Conf. Proc.*, vol. 12, p. 010035, 2016.

- [42] S. Holland, "Scinitillator material properties." <https://www.scionix.nl/frame>, 2017. Site checked on the 30th of August 2017.
- [43] H. Photonics, "Pmt specification sheet." [https://www.hamamatsu.com/resources/pdf/etd/R11265U\\_H11934\\_TPMH1336E.pdf](https://www.hamamatsu.com/resources/pdf/etd/R11265U_H11934_TPMH1336E.pdf), 2017. Site checked on the 30th of August 2017.

# List of Tables

|      |                                                                                                                                                                                         |    |
|------|-----------------------------------------------------------------------------------------------------------------------------------------------------------------------------------------|----|
| 2.1  | Table with the coherence condition for the neutrino energy of a selected target sample. . . . .                                                                                         | 14 |
| 2.2  | The results for the feasibility study performed by Lindner M., Maneschg W., Rink T., (2016); the signal rates are given in <i>cts/year</i> . . . . .                                    | 17 |
| 3.1  | Reduction rates in various energy ranges of the energy spectrum recorded with the Ge detector CONRAD. . . . .                                                                           | 33 |
| 4.1  | Estimated depletion voltages for the high voltage scan with the Ge detector CONRAD. . . . .                                                                                             | 47 |
| 4.2  | The peak count rates for the four different positions, recorded with the Ge detector CONRAD. . . . .                                                                                    | 49 |
| 4.3  | The estimated active volume for the Ge detector CONRAD.(by J.Hakenmüller) . . . . .                                                                                                     | 50 |
| 4.4  | Summary of the data files, which were used to create the final data set for Phase 1. . . . .                                                                                            | 52 |
| 4.5  | The resulting background levels ands reduction rates; recorded with the Ge detector CONRAD inside the CONUS shield. . . . .                                                             | 54 |
| 4.6  | The measured Germanium lines with CONRAD, which are induced by cosmic radiation and the values obtained with GIOVE (Measurement ID: 0040) . . . . .                                     | 56 |
| 4.7  | GIOVE count rate (in $[\frac{cts}{kg \cdot day}]$ if not stated otherwise) measured with an empty sample chamber (Measurement ID: 0080 (no muonveto) and 0040 (with muonveto)). . . . . | 57 |
| 4.8  | Reduction rates in various energy ranges of CONRAD and GIOVE. . . . .                                                                                                                   | 57 |
| 4.9  | Summary of the data files, which were used to create a preliminary data set for phase 2. . . . .                                                                                        | 59 |
| 4.10 | Preliminary background levels and the corresponding reduction rates for the phase 2; recorded with the Ge detector CONRAD inside the CONUS shield. . . . .                              | 62 |
| 4.11 | Cosmic radiation induced Germanium lines measured with CONRAD. . . . .                                                                                                                  | 63 |
| A.1  | The manufacturer's specifications for the used scintillator material [42]. . . . .                                                                                                      | 79 |
| B.1  | The used thresholds for the individual PMTs which were measured and set on the 30.06.2017. . . . .                                                                                      | 81 |
| C.1  | The detailed list of the unused time windows for the final dataset of phase 1. . . . .                                                                                                  | 86 |

# List of Figures

|     |                                                                                                                                                                                                                                                                                      |    |
|-----|--------------------------------------------------------------------------------------------------------------------------------------------------------------------------------------------------------------------------------------------------------------------------------------|----|
| 1.1 | Analysis the light output of a scintillator in two components: fast and slow [20]. . . . .                                                                                                                                                                                           | 4  |
| 1.2 | A basic scintillator set-up [20]. . . . .                                                                                                                                                                                                                                            | 5  |
| 1.3 | Left: The covalent bonding of silicon/germanium at 0 K, where all electrons are bound. Right: Above 0 K holes arise in the valence band [20]. . . . .                                                                                                                                | 5  |
| 1.4 | Left: An example for a semi-coaxial detector design. Right: An example for a point contact detector design [19]. . . . .                                                                                                                                                             | 6  |
| 1.5 | Reduction of cosmic radiation components in dependence of the penetration depth [17]. . . . .                                                                                                                                                                                        | 8  |
| 1.6 | Shielding layers of the GIOVE set-up for material screening [17]. . . . .                                                                                                                                                                                                            | 8  |
| 1.7 | Comparison of GIOVE background energy spectra with two other detectors [17]. . . . .                                                                                                                                                                                                 | 9  |
| 2.1 | Left: The Feynman diagram for the coherent elastic neutrino nucleus scattering. Right: Expected nuclear recoil energy for CE $\nu$ NS at a neutrino energy of 10 MeV for different target materials [27]. . . . .                                                                    | 12 |
| 2.2 | Left: The relation of the neutrino energy $E_\nu$ and the differential cross section $\sigma$ at different recoil energies $T$ . Right: The relation of the differential cross section and the recoil energy $T$ for different neutrino energies ( Figure made by T. Rink) . . . . . | 13 |
| 2.3 | Left: Schematic description of a CE $\nu$ NS signal [22]. Right: Expected ratio of ionization energy vs. recoil energy for a Germanium detector [29]. . . . .                                                                                                                        | 14 |
| 2.4 | An expected anti-neutrino spectrum form a reactor source. The dots represent measured data and the line is a parametrization, from [31, 32]. . . . .                                                                                                                                 | 16 |
| 2.5 | Left: Position for the CONUS experiment inside the nuclear power plant in Brokdorf [22] Right: An outside view of the nuclear power plant owned by PreussenElektra GmbH [30]. . . . .                                                                                                | 16 |
| 2.6 | The outer shell of the CONUS experiment, designed at the MPIK. The Image was created by the construction department of the MPIK.                                                                                                                                                     | 18 |
| 2.7 | Left: The schematic view of the inner layers of the shield. Right: The same view onto the assembled shield in the low-level laboratory at MPIK in Heidelberg. . . . .                                                                                                                | 18 |
| 2.8 | The web interface, which can be used to control the Lynx system. . . . .                                                                                                                                                                                                             | 21 |
| 2.9 | Difference between two synchronization pulses produced in MasterB mode for Lynx2 (left) and Lynx4 (right). . . . .                                                                                                                                                                   | 24 |



|      |                                                                                                                                                                                                                               |    |
|------|-------------------------------------------------------------------------------------------------------------------------------------------------------------------------------------------------------------------------------|----|
| 3.1  | The technical drawings showing the three models of scintillator plates used and their dimensions as well as the quantity of each plate. . . . .                                                                               | 26 |
| 3.2  | Response from one of the spare PMTs, performed by Reinhard Hofacker. . . . .                                                                                                                                                  | 26 |
| 3.3  | Left: The trace from PMT 1493 shows signs of light pollution. Right: The response of the same PMT with the lights in the laboratory turned off. . . . .                                                                       | 28 |
| 3.4  | Left: Image taken during the commissioning phase, with a upper side scintillator plate. Right: The top plate at its position within the shield. . . . .                                                                       | 29 |
| 3.5  | The used modules for the commissioning phase of the CONUS experiment. From the left: three discriminator slots, four ISEQ NHQ204M high voltage modules and an ORTEC Research Pulser. . . . .                                  | 29 |
| 3.6  | The exact position of the scintillator plates inside the shield, as well as the PMT position. The cardinal direction are in the relation to the final position of the CONUS experiment in the nuclear power plant. . . . .    | 30 |
| 3.7  | An example PMT energy spectrum, which shows the components effecting it. Taken form [17]. . . . .                                                                                                                             | 30 |
| 3.8  | The wiring diagram for the count rates measurement of a PMT in order to set the threshold. . . . .                                                                                                                            | 31 |
| 3.9  | An example threshold measurement for PMT 1442. The selected threshold setting is indicated by the red line. . . . .                                                                                                           | 32 |
| 3.10 | An overlay of the two energy spectra with the Ge detector CONRAD: (green) for the measurement from 30/06/2017, with the muonveto system ON; (grey) for the measurement from 05/07/2017, with the muonveto system OFF. . . . . | 34 |
| 3.11 | The incoming signal from a PMT on the two top graphs and the corresponding anti-coincidence window on the bottom plots. . . . .                                                                                               | 35 |
| 3.12 | The analogue trace of the incoming PMT signal, received from the Lynx DSO. . . . .                                                                                                                                            | 37 |
| 3.13 | The analogue trace of the incoming PMT signal, received from the Lynx DSO further zoomed than 3.12. . . . .                                                                                                                   | 37 |
| 3.14 | The schematic configuration for the performed measurement for section 3.5.2. . . . .                                                                                                                                          | 38 |
| 3.15 | An energy spectrum of PMT1442 taken in the low-level laboratory at the MPIK Heidelberg. The red area represents the muon events which shall be removed. . . . .                                                               | 39 |
| 3.16 | The flow-diagram for the script, which compares the two TLIST measured with the configuration shown in figure 3.14. . . . .                                                                                                   | 40 |
| 3.17 | The schematic for a synchronization test. . . . .                                                                                                                                                                             | 41 |
| 4.1  | Left: An exemplary energy spectrum containing the 1.173 MeV line from $\text{Co}^{60}$ , which is fitted with $f_{PF}$ . Right: The same energy spectrum this time $f_{PFLO}$ was used to fit the data. . . . .               | 45 |

|      |                                                                                                                                                                                                                                                            |    |
|------|------------------------------------------------------------------------------------------------------------------------------------------------------------------------------------------------------------------------------------------------------------|----|
| 4.2  | The peak position for the 1.173 MeV line of $\text{Co}^{60}$ . The individual data points have been fitted with $f_{PFLO}$ , the corresponding plot with $f_{PF}$ is shown in the appendix in figure C.2. . . . .                                          | 46 |
| 4.3  | The peak count rate for the 1.173 MeV line of $\text{Co}^{60}$ . The individual data points have been fitted with $f_{PFLO}$ , the corresponding plot with $f_{PF}$ is shown in the appendix in figure C.1. . . . .                                        | 46 |
| 4.4  | The $\text{Am}^{241}$ peak with its fit function. . . . .                                                                                                                                                                                                  | 48 |
| 4.5  | Left: The geometric sketch of the radiation source in relation to detector, which is used by the MCS. Right: Areal perspective of the geometry used by the MCS (by J.Hakenmüller). . . . .                                                                 | 48 |
| 4.6  | Left: The comparison between the MCS and the values from table 4.2, for the $\text{Co}^{60}$ - 1.173 MeV peak. Right: The comparison between the MCS and the values from table 4.2, for the $\text{Am}^{241}$ peak ratio.(by J.Hakenmüller) . . . . .      | 49 |
| 4.7  | Image taken during the initial construction of the CONUS shield. . . . .                                                                                                                                                                                   | 51 |
| 4.8  | Image taken once the shield and cage was fully set up. . . . .                                                                                                                                                                                             | 51 |
| 4.9  | The energy spectrum containing all the files listed in table 4.4, with the deactivated muonveto. . . . .                                                                                                                                                   | 53 |
| 4.10 | The energy spectrum containing all the files listed in table 4.4, with an active muonveto system. For better resolution it is split into two parts. The whole spectrum is shown in figure C.5. . . . .                                                     | 55 |
| 4.11 | The energy spectrum with the marked germanium lines. . . . .                                                                                                                                                                                               | 56 |
| 4.12 | Left: View into the innermost layer of the CONUS shield with two detectors CONRAD (left) and one CONUS detector (right). Right: An outside view onto the CONUS shield without the steel cage, instead foil was used as light and radon protection. . . . . | 58 |
| 4.13 | The energy spectrum containing all the files listed in table 4.9. Measurements were performed with deactivated muonveto. . . . .                                                                                                                           | 60 |
| 4.14 | The energy spectrum containing all the files listed in table 4.9. Measurements were performed with activated muonveto. For better resolution it is split into two parts. The whole spectrum is shown in figure C.6. . . . .                                | 61 |
| 4.15 | The energy spectrum for phase 2 with the marked germanium lines. . . . .                                                                                                                                                                                   | 62 |
| 4.16 | The compared energy spectra from the beginning and middle of phase 2. . . . .                                                                                                                                                                              | 64 |
| A.1  | The wiring diagram for the three discriminators used for the PMT signals. See table B.1 to resolve the name. . . . .                                                                                                                                       | 79 |
| B.1  | The individual PMT threshold measurements for PMT channels W1 - W10, the used threshold according to B.1 is marked. . . . .                                                                                                                                | 82 |
| B.2  | The individual PMT threshold measurements for PMT channels E1 - E10, the used threshold according to B.1 is marked. . . . .                                                                                                                                | 83 |
| B.3  | Energy spectrum for the CONRAD measurement form 05/07/2017 (duration 110h) with the deactivated muonveto system. . . . .                                                                                                                                   | 84 |

|     |                                                                                                                                                                                     |    |
|-----|-------------------------------------------------------------------------------------------------------------------------------------------------------------------------------------|----|
| B.4 | Energy spectrum for the CONRAD measurement from 30/06/2017 (duration 65h) with the activated muonveto system. . . . .                                                               | 84 |
| C.1 | The peak position for the 1.173 MeV line of $\text{Co}^{60}$ . The individual data points have been fitted with $f_{PF}$ . . . . .                                                  | 85 |
| C.2 | The peak position for the 1.173 MeV line of $\text{Co}^{60}$ . The individual data points have been fitted with $f_{PF}$ . . . . .                                                  | 85 |
| C.3 | The fitted peaks of a $\text{Th}^{228}$ calibration measurement from the 30/06/2017.                                                                                                | 87 |
| C.4 | The fitted peaks of a $\text{Th}^{228}$ calibration measurement from the 25/08/2017.                                                                                                | 87 |
| C.5 | The energy spectrum for phase 1 containing all the files listed in table 4.4, with the active muonveto. . . . .                                                                     | 88 |
| C.6 | The energy spectrum for phase 2 containing all the files listed in table 4.9, with the active muonveto. . . . .                                                                     | 89 |
| D.1 | The results for a 350h long stability measurement. The deadtime of the Lynx as well as the channel of the peak position for the measured $\text{Am}^{241}$ peak is plotted. . . . . | 90 |



# A Scintillator Plates

| Property                       | specified by the manufacturer |
|--------------------------------|-------------------------------|
| Scintillator Material          | EJ-200                        |
| Wavelength of Maximum Emission | 425 nm                        |
| Light Attenuation Length       | 380 cm                        |
| Density                        | 1.023 g/cm <sup>3</sup>       |
| Refraction Index               | 1.58                          |
| Temperature Range              | -20°C to 60°C                 |

**Table A.1:** The manufacturer's specifications for the used scintillator material [42].

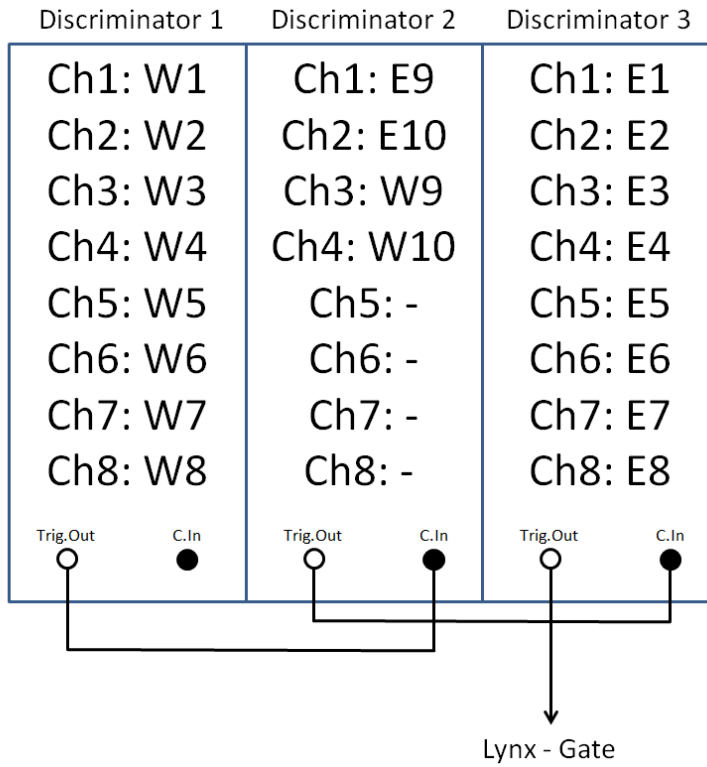


**Figure A.1:** The wiring diagram for the three discriminators used for the PMT signals. See table B.1 to resolve the name.

# PMTs

The used PMTs for the muonveto system [43].

## PHOTOMULTIPLIER TUBES AND PHOTOMULTIPLIER TUBE ASSEMBLIES R11265U SERIES / H11934 SERIES

### FEATURES

- Wide effective area: 23 mm x 23 mm
- High speed response
- Compact
- Light weight: Approx. 31 g (R11265U series)  
Approx. 74 g (H11934 series)
- R11265 series with divider circuit (H11934 series)

### APPLICATIONS

- High energy physics
- Scintillation counting
- Portable radiation monitor with nuclear identification



Left: R11265U series, Right: H11934 series

## PHOTOMULTIPLIER TUBES AND PHOTOMULTIPLIER TUBE ASSEMBLIES R11265U SERIES / H11934 SERIES

| Type No.      | Spectral response |                      | Photo-cathode material | Window material | Dynode stages | Maximum ratings | Cathode characteristics |      |          |         |         |    |     |
|---------------|-------------------|----------------------|------------------------|-----------------|---------------|-----------------|-------------------------|------|----------|---------|---------|----|-----|
|               | Range (nm)        | Peak wavelength (nm) |                        |                 |               |                 | Luminous                | Blue | Redshift | Quantum | Radiant |    |     |
| R11265U-100   | 300 to 650        | 400                  | SBA                    | K               | MC12          | 1000            | 0.1                     | 90   | 105      | 13.5    | —       | 35 | 110 |
| R11265U-200   | 300 to 650        | 400                  | UBA                    | K               | MC12          | 1000            | 0.1                     | 90   | 135      | 15.5    | —       | 43 | 130 |
| R11265U-300   | 300 to 700        | 420                  | EGBA                   | K               | MC12          | 1000            | 0.1                     | 120  | 160      | 14      | —       | 39 | 125 |
| R11265U-20    | 300 to 920        | 530                  | ERMA                   | K               | MC12          | 1000            | 0.1                     | 350  | 500      | —       | 0.4     | 19 | 78  |
| H11934-100    | 300 to 650        | 400                  | SBA                    | K               | MC12          | -1000           | 0.018                   | 90   | 105      | 13.5    | —       | 35 | 110 |
| H11934-200    | 300 to 650        | 400                  | UBA                    | K               | MC12          | -1000           | 0.018                   | 90   | 135      | 15.5    | —       | 43 | 130 |
| H11934-300    | 300 to 700        | 420                  | EGBA                   | K               | MC12          | -1000           | 0.018                   | 120  | 160      | 14      | —       | 39 | 125 |
| H11934-100-10 | 300 to 650        | 400                  | SBA                    | K               | MC12          | -1000           | 0.018                   | 90   | 105      | 13.5    | —       | 35 | 110 |
| H11934-200-10 | 300 to 650        | 400                  | UBA                    | K               | MC12          | -1000           | 0.018                   | 90   | 135      | 15.5    | —       | 43 | 130 |
| H11934-300-10 | 300 to 700        | 420                  | EGBA                   | K               | MC12          | -1000           | 0.018                   | 120  | 160      | 14      | —       | 39 | 125 |
| H11934-20     | 300 to 920        | 530                  | ERMA                   | K               | MC12          | -1000           | 0.018                   | 350  | 500      | —       | 0.4     | 19 | 78  |

**NOTE:** (A) SBA: Super bialkali, UBA: Ultra bialkali, EGBA: Extended green bialkali, ERMA: Extended red multialkali  
 (B) K: Borosilicate glass (K type is available)  
 (C) MC: Metal channel  
 (D) Quantum efficiency is measured at the peak sensitivity wavelength (100/200 series: 390 nm, 300 series: 380 nm, 20 series: 500 nm)  
 (E) Cathode radiant sensitivity is measured at the peak sensitivity wavelength (100/200 series: 400 nm, 300 series: 420 nm, 20 series: 530 nm).

Figure 1: Typical spectral response

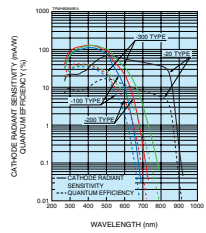


Figure 2: Typical gain

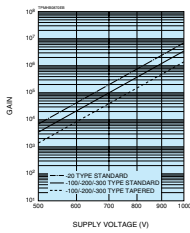


Figure 3: Time response (Example)

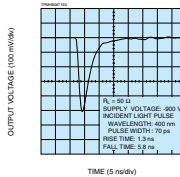


Figure 4: Single photon counting (Example)

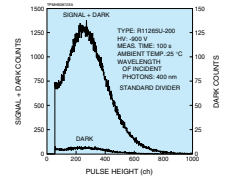
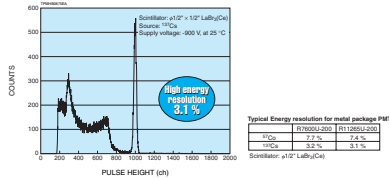


Figure 5: Energy resolution



© Hamamatsu Photonics K.K. 2021. All rights reserved. This document contains confidential and/or proprietary information of Hamamatsu Photonics K.K. The information is not to be disclosed, copied, or reproduced without the prior written consent of Hamamatsu Photonics K.K. The information is not to be used for any other purposes than those specified in this document. Specifications are subject to change without notice. No patent rights are granted by all of the circuits described herein. ©2021 Hamamatsu Photonics K.K.

## PHOTOMULTIPLIER TUBES AND PHOTOMULTIPLIER TUBE ASSEMBLIES R11265U SERIES / H11934 SERIES

## PHOTOMULTIPLIER TUBES AND PHOTOMULTIPLIER TUBE ASSEMBLIES R11265U SERIES / H11934 SERIES

| Anode to cathode supply voltage (V) | Luminous   |            |                          | Anode characteristics |                                       |           | Time response  |                   |             | Pulse linearity    |                    |            | Operating ambient temperature (°C) | Storage temperature (°C) | Type No.    |
|-------------------------------------|------------|------------|--------------------------|-----------------------|---------------------------------------|-----------|----------------|-------------------|-------------|--------------------|--------------------|------------|------------------------------------|--------------------------|-------------|
|                                     | Min. (A/m) | Typ. (A/m) | Max. (A/m)               | Gain                  | Dark current (After 30 min) Typ. (nA) | Max. (nA) | Rise time (ns) | Transit time (ns) | T.T.S. (ns) | -2% Deviation (mA) | +5% Deviation (mA) |            |                                    |                          |             |
| 900                                 | 150        | 150        | 120                      | 1.2 × 10 <sup>6</sup> | 2                                     | 20        | 0.27           | 20                | 60          | 0.30               | (300)              | (400)      | -30 to +50                         | +50                      | R11265U-100 |
| 900                                 | 250        | 250        | 150                      | 4.8 × 10 <sup>6</sup> | 2                                     | 20        | 0.27           | 20                | 60          | 0.30               | (300)              | (400)      | -30 to +50                         | +50                      | R11265U-200 |
| 900                                 | 250        | 250        | 150                      | 1.8 × 10 <sup>6</sup> | 2                                     | 20        | 0.27           | 20                | 60          | 0.30               | (300)              | (400)      | -30 to +50                         | +50                      | R11265U-300 |
| 900                                 | 250        | 1200       | 2.4 × 10 <sup>6</sup>    | 30                    | 200                                   | 1.3       | 5.8            | 0.27              | 20          | 60                 | 0.27               | 20         | 0 to +50                           | +15 to +50               | H11934-100  |
| -900                                | 25         | 126        | 1.2 × 10 <sup>6</sup>    | 2                     | 20                                    | 0.27      | 20             | 60                | 0.30        | (300)              | (400)              | -30 to +50 | +50                                | H11934-200               |             |
| -900                                | 25         | 182        | 1.2 × 10 <sup>6</sup>    | 2                     | 20                                    | 0.27      | 20             | 60                | 0.30        | (300)              | (400)              | -30 to +50 | +50                                | H11934-300               |             |
| -900                                | 50         | 192        | 1.2 × 10 <sup>6</sup>    | 2                     | 20                                    | 0.27      | 20             | 60                | 0.30        | (300)              | (400)              | -30 to +50 | +50                                | H11934-100-10            |             |
| -900                                | (25)       | (150)      | (4.8 × 10 <sup>6</sup> ) | 2                     | 20                                    | 0.27      | 20             | 60                | 0.30        | (300)              | (400)              | -30 to +50 | +50                                | H11934-200-10            |             |
| -900                                | (25)       | (65)       | (4.8 × 10 <sup>6</sup> ) | 2                     | 20                                    | 0.27      | 20             | 60                | 0.30        | (300)              | (400)              | -30 to +50 | +50                                | H11934-300-10            |             |
| -900                                | (25)       | (77)       | (4.8 × 10 <sup>6</sup> ) | 2                     | 20                                    | 0.27      | 20             | 60                | 0.30        | (300)              | (400)              | -30 to +50 | +50                                | H11934-20                |             |
| -900                                | 250        | 1200       | 2.4 × 10 <sup>6</sup>    | 30                    | 200                                   | 1.3       | 5.8            | 0.27              | 20          | 60                 | 0.27               | 20         | 0 to +50                           | +15 to +50               | H11934-20   |

( ): Measured with the special voltage distribution ratio (Tapered Divider) shown below.

### VOLTAGE DISTRIBUTION RATIO AND SUPPLY VOLTAGE

| Electrodes            | K   | Dy1 | Dy2 | Dy3 | Dy4 | Dy5 | Dy6 | Dy7 | Dy8 | Dy9 | Dy10 | Dy11 | Dy12 | P   |
|-----------------------|-----|-----|-----|-----|-----|-----|-----|-----|-----|-----|------|------|------|-----|
| Standard divider type | 2.5 | 1.2 | 0.8 | 0.8 | 1   | 1   | 1   | 1   | 1   | 1   | 1    | 1    | 1    | 0.5 |
| Tapered divider type  | 3.3 | 1.8 | 1   | 1   | 1   | 1   | 1   | 1   | 1   | 1   | 1    | 1    | 2.7  | 1.3 |

Supply voltage: 900 V, K: Cathode, Dy: Dynode, P: Anode

Figure 6: T.T.S. characteristic (Example)

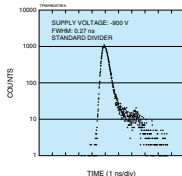


Figure 7: Effect of magnetic fields on anode output (Example)

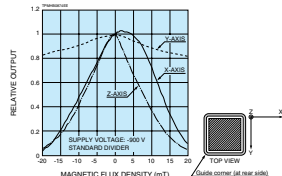


Figure 8: Dimensional outline and basing diagram (Unit: mm)

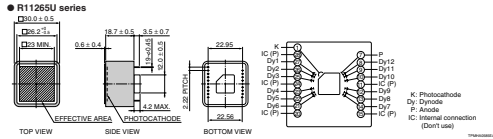
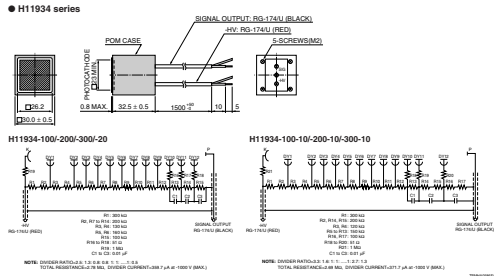
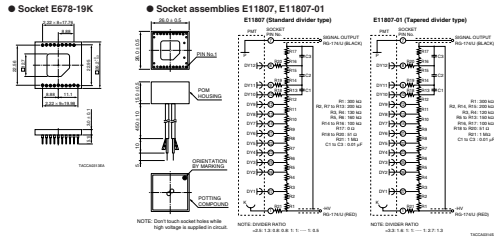


Figure 9: Dimensional outline and circuit diagram (Unit: mm)



### [ACCESSORIES] (Unit: mm) [SOLD SEPARATELY]



#### WARNING - High voltage -

The product is operated at high voltage potential. Further, the metal housing of the product is connected to the photocathode (potential) so that it becomes a high voltage potential when the product is operated at a negative high voltage (anode grounded).

**Important safety information:** Please refer to the instruction manual for the operator or the damage to other instruments.

\* CAS200 and CAS500-01 can be used for R11265U series / H11934 series.

# B Myonveto System for CONUS

## B.1 Thresholds

| HV -Box | Spannung [-V] | Kamin ID | PMT ID | Schwelle [mV]<br>30.06.2017 |
|---------|---------------|----------|--------|-----------------------------|
| HV1     | 780           | W2       | 1429   | -3                          |
|         |               | E8       | 1431   | -5                          |
|         |               | W7       | 1491   | -5                          |
|         |               | W3       | 1489   | -5                          |
| HV2     | 780           | E3       | 1417   | -3                          |
|         |               | E7       | 1453   | -3                          |
|         |               | E5       | 1475   | -3                          |
|         |               | E9       | 1496   | -3                          |
| HV3     | 780           | W5       | 1376   | -3                          |
|         |               | E10      | 1446   | -3                          |
|         |               | E2       | 1467   | -3                          |
|         |               | W8       | 1397   | -7                          |
| HV4     | 780V          | E4       | 1476   | -3                          |
|         |               | W10      | 1493   | -4                          |
|         |               | W4       | 1471   | -5                          |
|         |               | W9       | 1377   | -7                          |
| HV5     | 860           | E1       | 1487   | -5                          |
|         |               | E6       | 1455   | -5                          |
|         |               | W1       | 1442   | -5                          |
|         |               | W6       | 1466   | -3                          |

**Table B.1:** The used thresholds for the individual PMTs which were measured and set on the 30.06.2017.

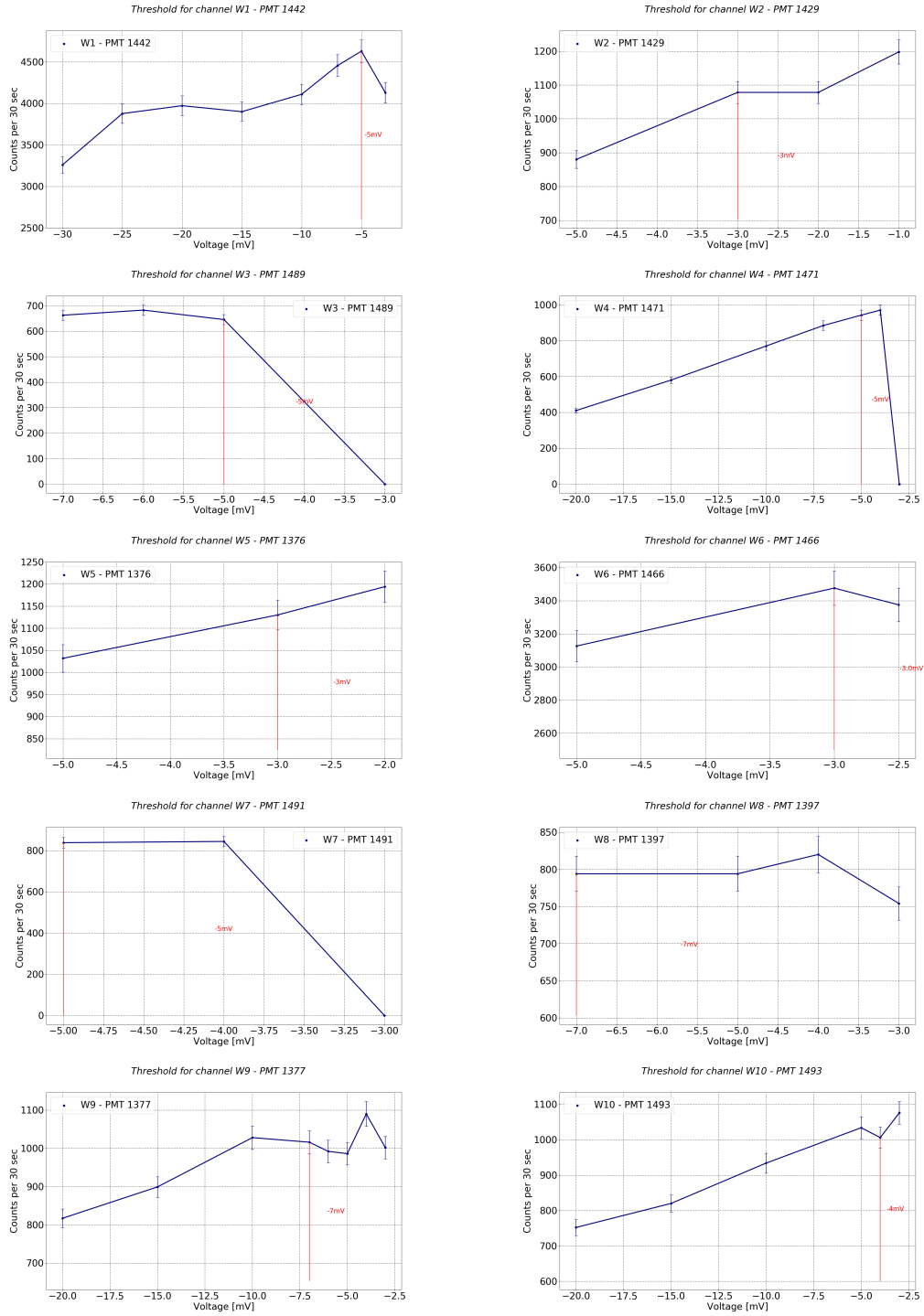


**Figure B.1:** The individual PMT threshold measurements for PMT channels W1 - W10, the used threshold according to B.1 is marked.



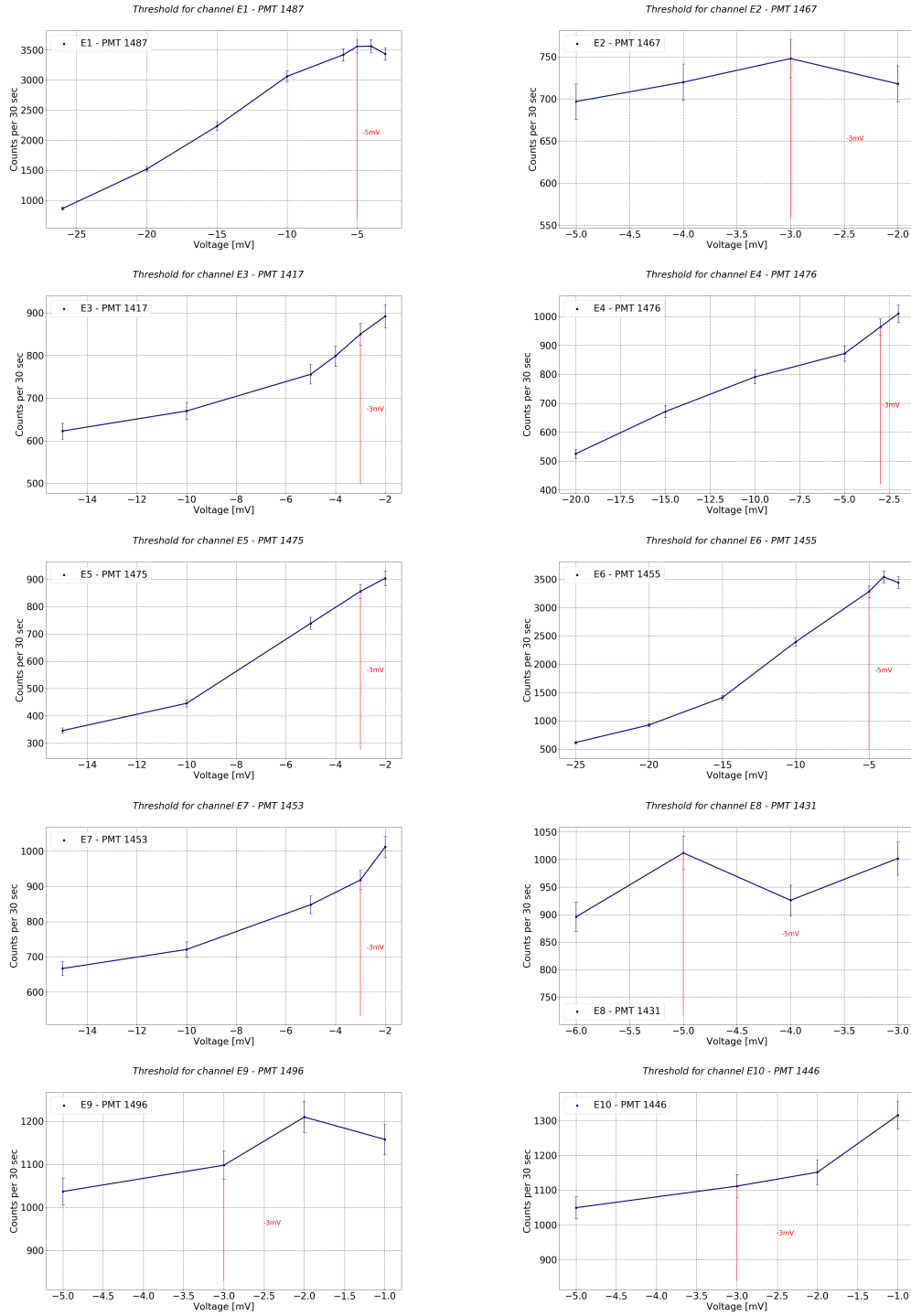


**Figure B.2:** The individual PMT threshold measurements for PMT channels E1 - E10, the used threshold according to B.1 is marked.

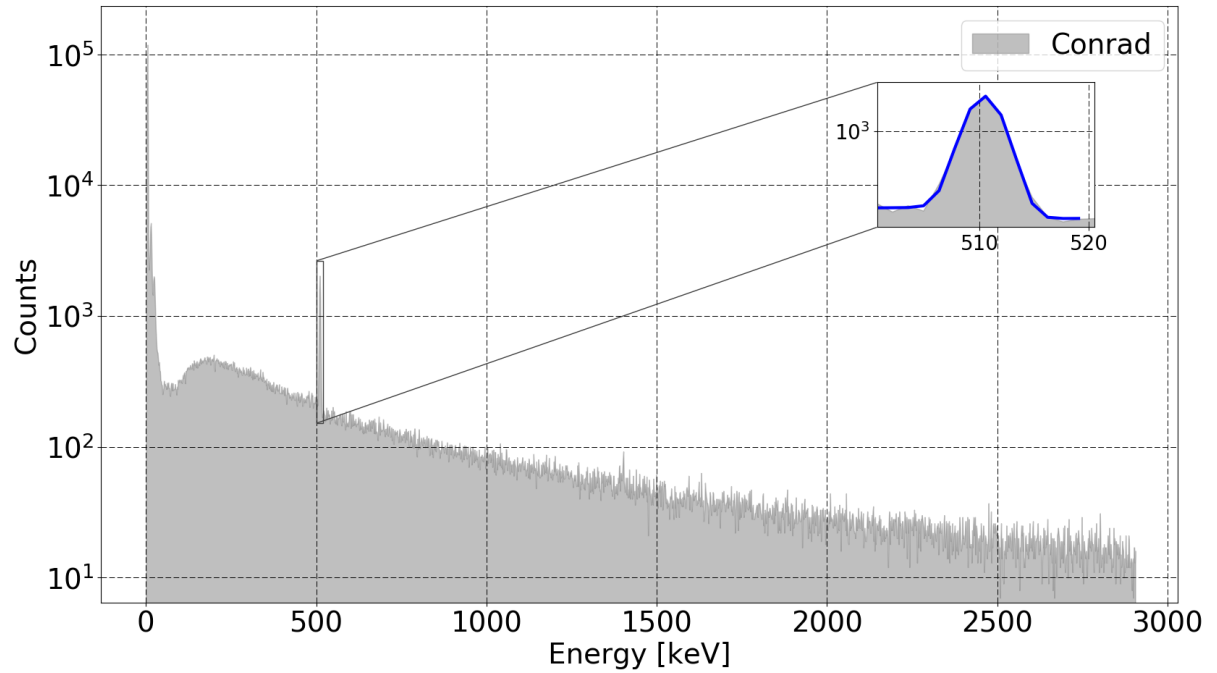


**Figure B.3:** Energy spectrum for the CONRAD measurement from 05/07/2017 (duration 110h) with the deactivated muonveto system.

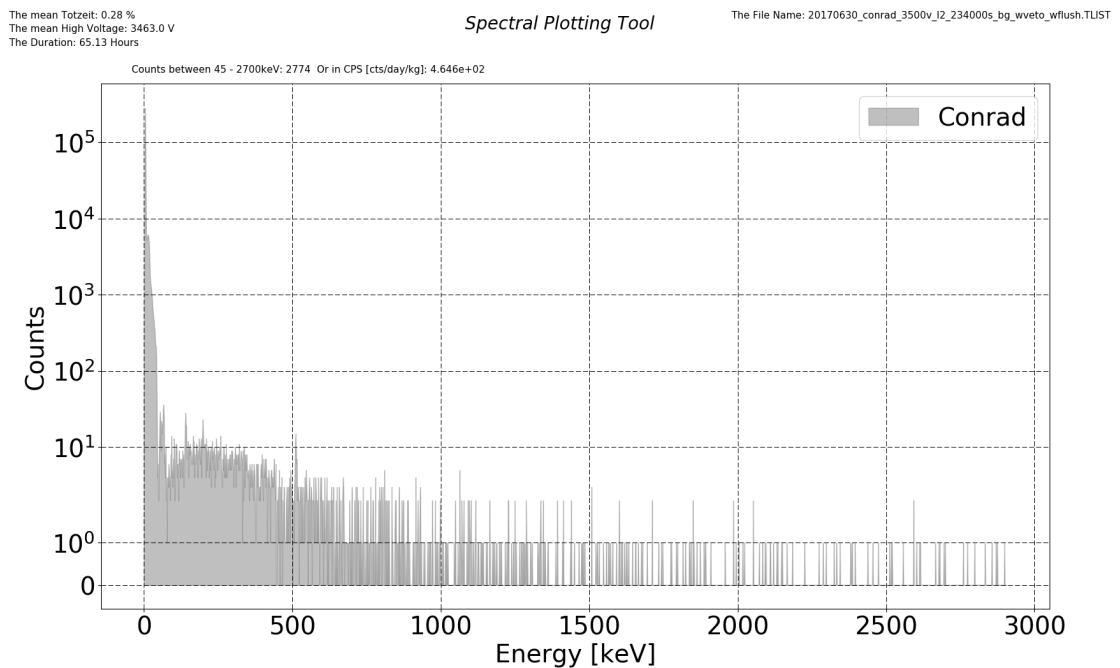


**Figure B.4:** Energy spectrum for the CONRAD measurement from 30/06/2017 (duration 65h) with the activated muonveto system.

# C Commissioning of the CONUS Shield

## C.1 HV - Scan

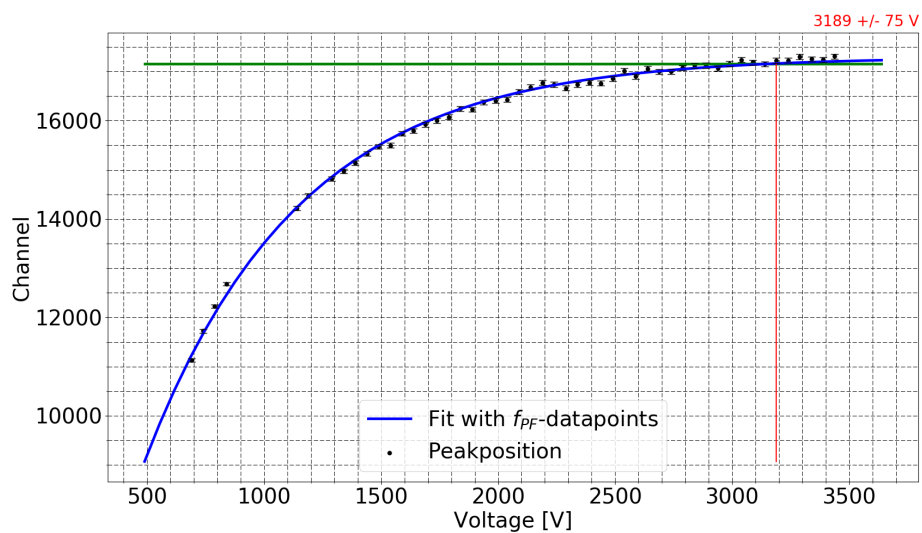


Figure C.1: The peak position for the 1.173 MeV line of  $\text{Co}^{60}$ . The individual data points have been fitted with  $f_{PF}$ .

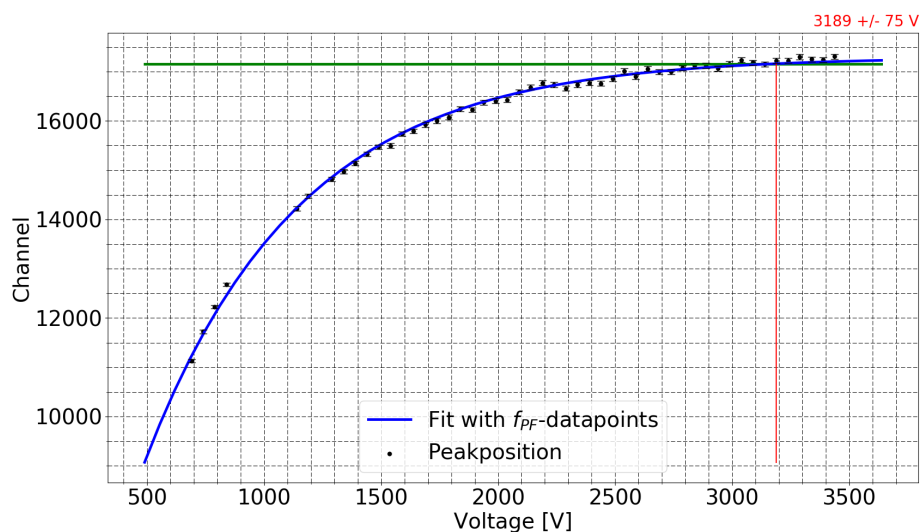


Figure C.2: The peak position for the 1.173 MeV line of  $\text{Co}^{60}$ . The individual data points have been fitted with  $f_{PF}$ .

## C.2 Phase 1 and 2

|                   |                     |                                                                                                                          |                               |
|-------------------|---------------------|--------------------------------------------------------------------------------------------------------------------------|-------------------------------|
| <b>CONRAD</b>     |                     |                                                                                                                          |                               |
| With Veto:        |                     |                                                                                                                          |                               |
| <b>05.07.2017</b> | <b>Window</b>       | <b>Data Description</b>                                                                                                  | <b>Reason</b>                 |
| 05.07.2017        | 16:05:19 – 18:05:19 | High Noise: >150[cts/kg/day] in 45-50keV, >998 [cts/kg/day] in 45-100keV, >2470[cts/kg/day] in 100-500keV                | Initial Noise                 |
| <b>10.07.2017</b> | <b>Window</b>       | <b>Data Description</b>                                                                                                  | <b>Reason</b>                 |
| 11.07.2017        | 10:44:17 – 12:44:11 | Very high countrate between 45-500keV (up to 45x larger than expected)                                                   | Unphysical                    |
| 11.07.2017        | 14:44:26 – 16:44:26 | Very high countrate throughout the spectrum (1000x larger in [45-50], rest ~50x larger)                                  | Unphysical                    |
| 12.07.2017        | 06:44:13 – 08:44:13 | Refilling of the Dewar                                                                                                   | Unphysical                    |
| 12.07.2017        | 08:44:11 – 10:44:11 | Refilling of the Dewar                                                                                                   | Unphysical                    |
| 12.07.2017        | 10:44:09 – 12:44:09 | Refilling of the Dewar                                                                                                   | Unphysical                    |
| 12.07.2017        | 12:44:10 – 14:44:10 | Very high countrate throughout the spectrum (25000x larger in [45-50], rest ~450x larger) (higher than Refilling counts) | Unphysical                    |
| 12.07.2017        | 14:44:11 – 16:44:11 | Almost twice the expected countrate between [520-2620]keV                                                                | Microphony due to Work in LLL |
| 13.07.2017        | 08:44:12 – 10:44:12 | High Noise: >60 [cts/kg/day] in 45-50keV, >220 [cts/kg/day] in 45-100keV                                                 | Microphony due to Work in LLL |
| 13.07.2017        | 10:44:10 – 12:44:10 | High Noise: >30 [cts/kg/day] in 45-50keV, >100 [cts/kg/day] in 45-100keV                                                 | Microphony due to Work in LLL |
| 13.07.2017        | 14:44:10 – 16:44:10 | High Noise: >130 [cts/kg/day] in 45-50keV, >670 [cts/kg/day] in 45-100keV                                                | Microphony due to Work in LLL |
| <b>14.07.2017</b> | <b>Window</b>       | <b>Data Description</b>                                                                                                  | <b>Reason</b>                 |
| 16.07.2017        | 12:36:05 – 14:36:05 | High Noise: >530 [cts/kg/day] in 45-100keV, >800 [cts/kg/day] in 100-500keV, >1440 [cts/kg/day] in 45-2700keV            | Unphysical                    |
| <b>17.07.2017</b> | <b>Window</b>       | <b>Data Description</b>                                                                                                  | <b>Reason</b>                 |
| 19.07.2017        | 06:06:49 – 08:06:49 | Very High Noise over all 45-2700keV: 48e6 counts/kg/day                                                                  | Unphysical                    |
| 19.07.2017        | 08:06:45 – 10:06:45 | Very High Noise over all 45-2700keV: 41e6 counts/kg/day                                                                  | Unphysical                    |
| 19.07.2017        | 10:06:49 – 12:06:49 | Very High Noise over all 45-2700keV: 88e3 counts/kg/day                                                                  | Unphysical                    |
| Without Veto:     |                     |                                                                                                                          |                               |
| <b>05.07.2017</b> | <b>Window</b>       | <b>Data Description</b>                                                                                                  | <b>Reason</b>                 |
| 05.07.2017        | 16:15:47 – 18:15:47 | Very High Noise 45-500keV (almost twice the expected rate)                                                               | Work in LLL                   |
| <b>10.07.2017</b> | <b>Window</b>       | <b>Data Description</b>                                                                                                  | <b>Reason</b>                 |
| 12.07.2017        | 06:55:29 – 08:55:29 | Refilling of the Dewar                                                                                                   | Unphysical                    |
| 12.07.2017        | 08:55:29 – 10:55:29 | Refilling of the Dewar                                                                                                   | Unphysical                    |
| 12.07.2017        | 10:55:28 – 12:55:28 | Refilling of the Dewar                                                                                                   | Unphysical                    |
| 12.07.2017        | 12:55:29 – 14:55:29 | Very high countrate throughout the spectrum ~10x larger than avg.                                                        | Unphysical                    |

Table C.1: The detailed list of the unused time windows for the final dataset of phase 1.

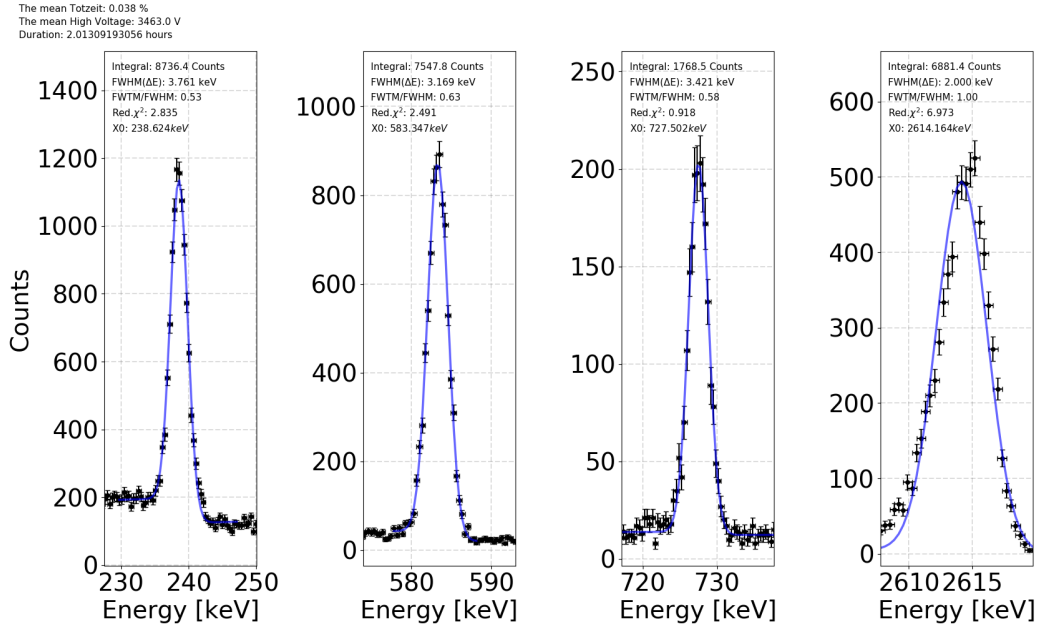


Figure C.3: The fitted peaks of a  $\text{Th}^{228}$  calibration measurement from the 30/06/2017.

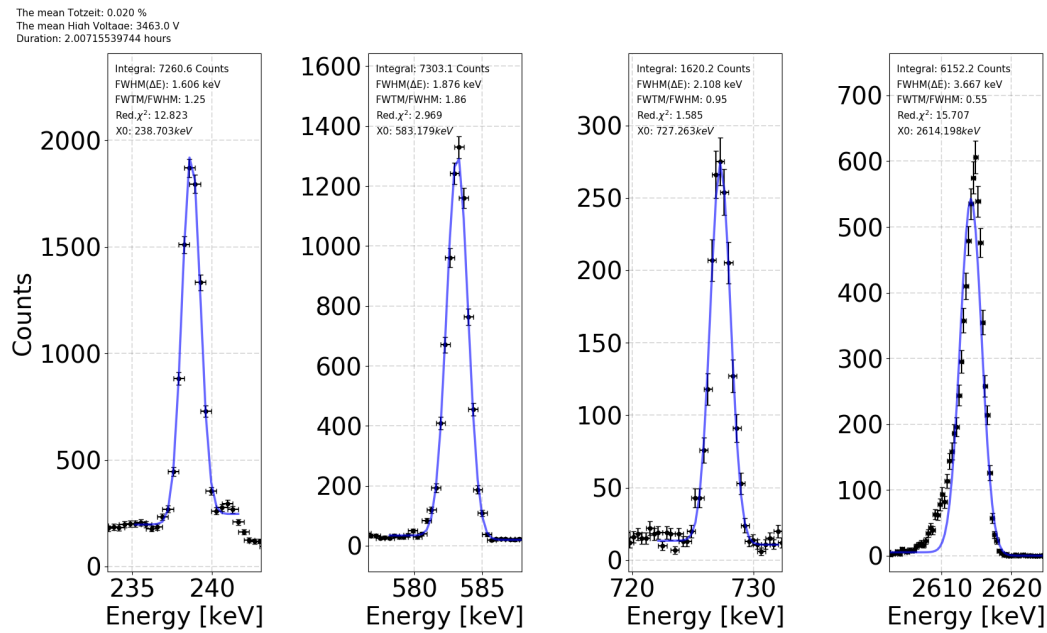
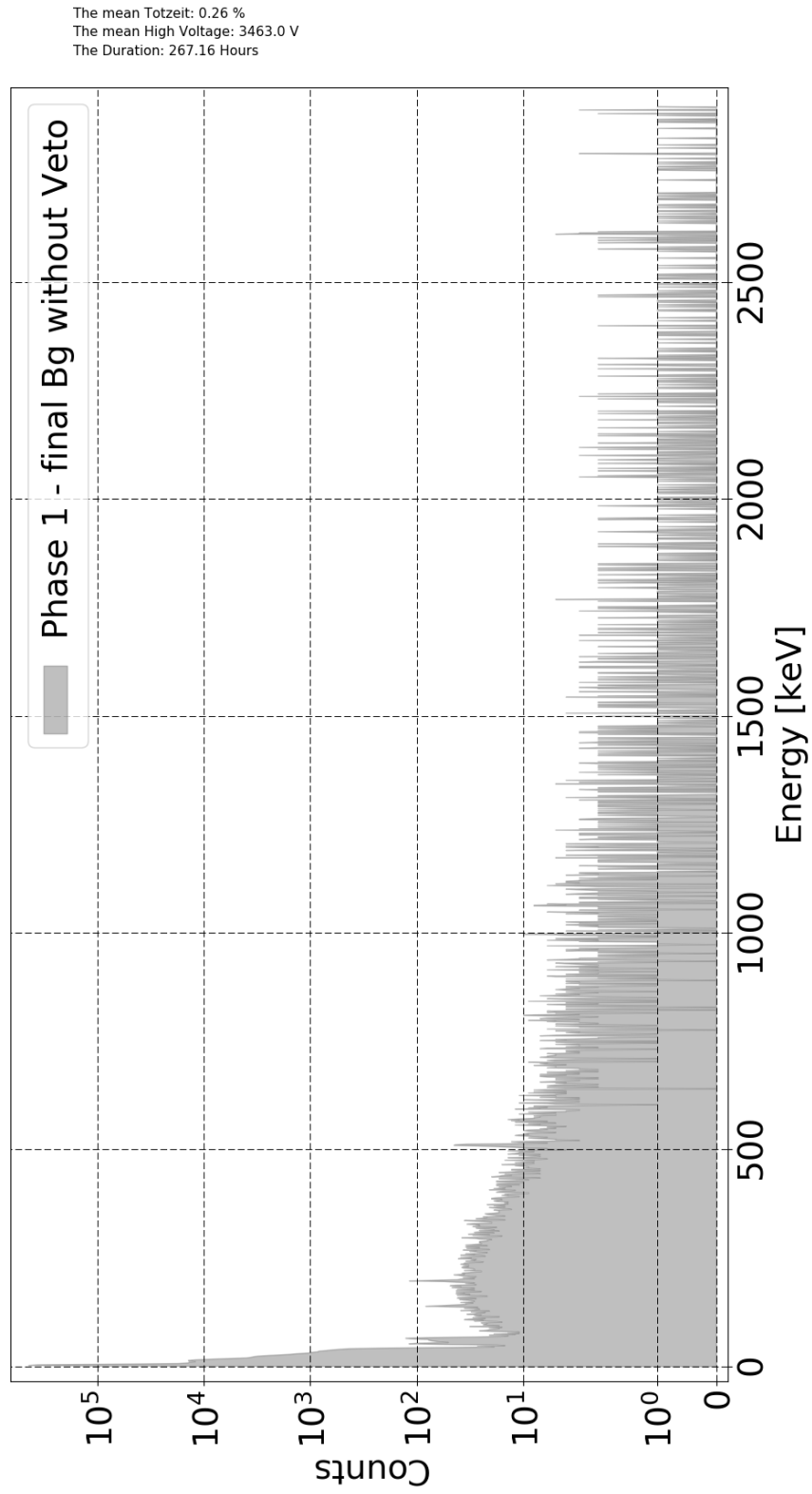
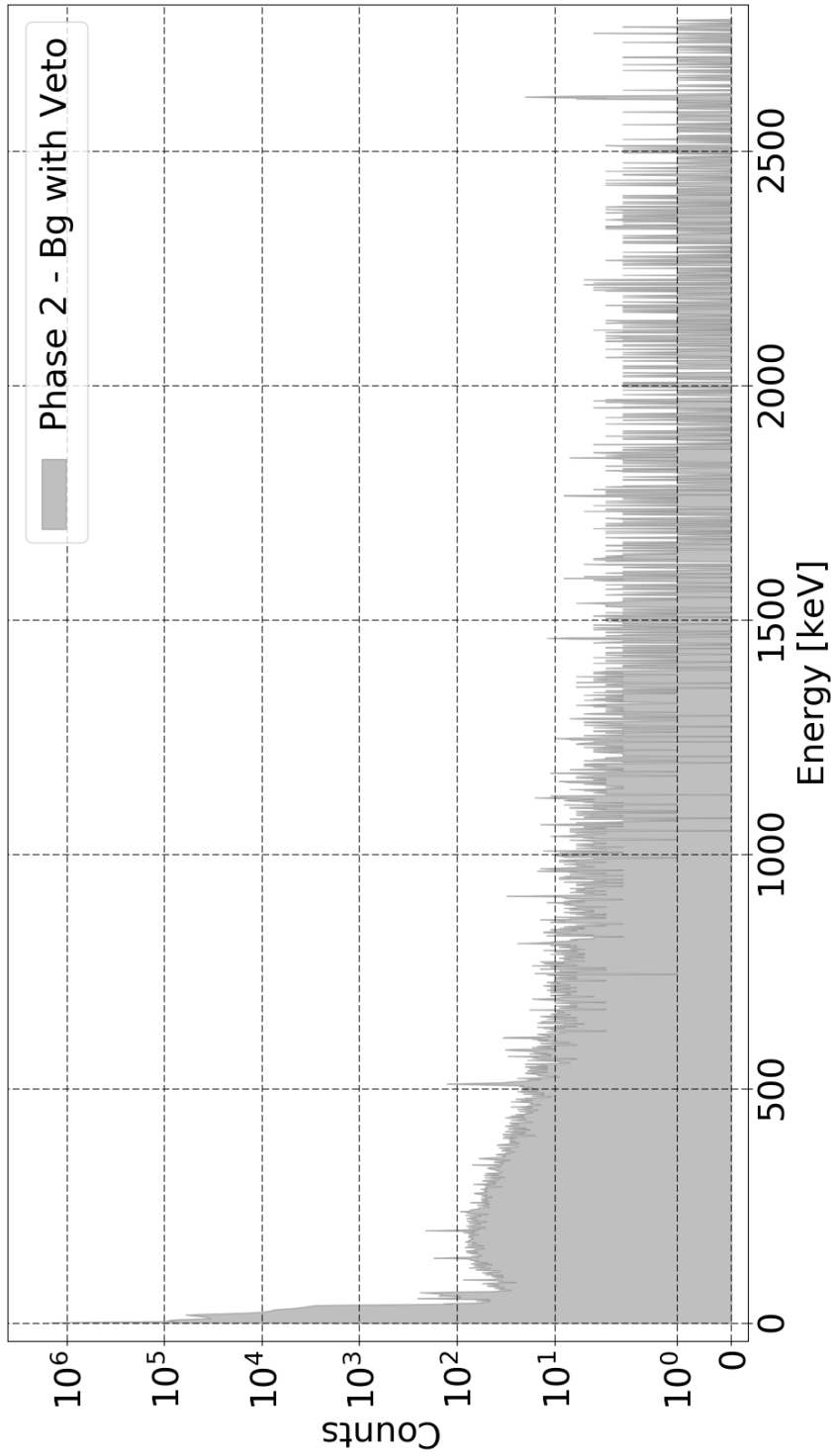


Figure C.4: The fitted peaks of a  $\text{Th}^{228}$  calibration measurement from the 25/08/2017.



**Figure C.5:** The energy spectrum for phase 1 containing all the files listed in table 4.4, with the active muonveto.

The mean Totzeit: 0.34 %  
The mean High Voltage: 3463.1 V  
The Duration: 458.41 Hours



**Figure C.6:** The energy spectrum for phase 2 containing all the files listed in table 4.9, with the active muonveto.

## D Lynx

Prior to the start of CONUS, a lot of developing efforts were done involving the Lynx DAQ, which included creating a save script for the Ge-screening detectors in the LLL at MPIK Heidelberg. Since this was done for a Windows environment, therefore the created software was developed in C++. This scripts were based around the Software Genie2000, which is provided by the company CANBERRA. Furthermore, the Lynx devices used in the CONUS experiment were tested in their general functions, which is not presented in the main chapter of this thesis. A short example of such tests is shown in the following. Furthermore, since a lot of time was used for creating the Lynx scripts using Python and creating a working measurement environment, section D.2 will give a brief introduction in how to use Python to control the Lynx DAQ.

### D.1 Stability Analysis

Prior to the commissioning phases of CONUS, the Lynx DAQ has been used in combination with another germanium detector (ASTERIX) to test the stability over time. Therefore a long term measurement was conducted with an  $\text{Am}^{241}$  as radiation source. The energy spectrum was only recording the 59 keV peak of  $\text{Am}^{241}$ . The analysed parameters were the peak position the Lynx showed as well as the calculated deadtime. The deadtime was very stable within its error, so was the peak position. The latter, only deviates one channel from the mean for a few times frames.

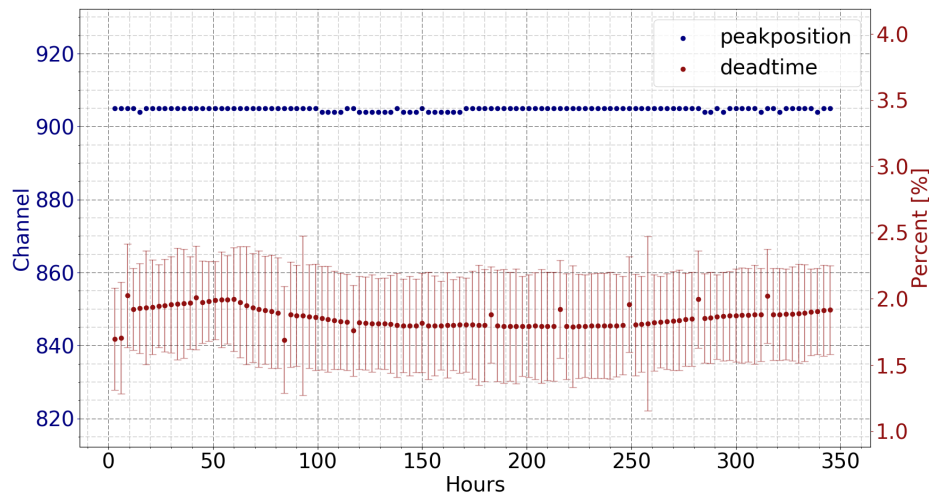


**Figure D.1:** The results for a 350h long stability measurement. The dead-time of the Lynx as well as the channel of the peak position for the measured  $\text{Am}^{241}$  peak is plotted.



## D.2 SDK Guide

This shall be a short guide for the Lynx SDK which assumes basic knowledge of at least one programming language (e.g. C, C++, Java, Python,...). The examples will be shown in Python due to the simplicity of this particular programming language. Furthermore, the Python implementation of the Lynx SDK offers a small access to the Lynx source files, where the other supported languages rely on the "Lynx Communications Libraries" documentation files distributed with the SDK.

### Connecting to the Lynx

The first step for connecting with a Lynx, is the physical connection with the Lynx (e.g. Ethernet, USB, RS-232). The simplest method is a network connection which is especially useful if multiple Lynx systems are in use. Initially each Lynx has the IP address "10.0.0.1", which can be changed via various ways (e.g. the web-interface see 2.3). Once the IP address is known, a connection can be established. First the environment for the Lynx has to be initialized. The Python command needed is:

```
#Necessary imports:
import Utilities
import DeviceFactory
import ParameterCodes
```

```
#Setup the Python env
Utilities.setup()
```

Once the environment is set up, a lynx variable (interface) has to be created. This then represents the Lynx, via which all the properties can be accessed.

```
#Create the interface
lynx = DeviceFactory.createInstance(DeviceFactory.DeviceInterface.
IDevice)
```

```
#Open a connection to the device
lynx.open("", "10.0.0.1")
```

The first parameter for the `open` method is the IP address of the client and the second one is the IP address of the Lynx. If the client address is empty like in the example above, the best network adapter available will be used, which should be the best option for most applications.

### Controlling the Lynx

The main options to control the Lynx are:

```
#control the Lynx via the CommandCodes (the example below resets
the memory for the current input):
```

```
lynx.control(CommandCodes.Clear, input)
```

```
#get and set parameters of the Lynx:
```

```
lynx_coarsegain = lynx.getParameter(ParameterCodes.Input_CoarseGain
, input)
```

```
lynx.setParameter(ParameterCodes.Input_FineGain, 1.2, input)
```

A list for all the available `CommandCodes` can only be found in the corresponding python source file, whereas the `ParameterCodes` can be found in the "Lynx Communications Libraries" documentation or the corresponding python source file.

## Measurements with the Lynx

To start a measurement, the `control` method of the Lynx is required.

```
#Start the acquisition
```

```
lynx.control(CommandCodes.Start, input)
```

Once the measurement is started, one has to handle the datastream. The example below shows how the measurement script could work for a measurement in LIST or TLIST mode.

```
while True:
```

```
    #Get the status
```

```
    status = lynx.getParameter(ParameterCodes.Input_Status, input)
```

```
    #Get the list data
```

```
    listB = lynx.getListData(input)
```

```
    #Checks whether measurement is LIST or TLIST mode and creates a
    #corresponding output
```

```
    if (isinstance(listB, ListData)):
```

```
        for event in listB.getEvents():
```

```
            print "Event: %d"%event
```

```
    else:
```

```
        Utilities.reconstructAndOutputTlistData(listB, listB.
```

```
        getTimebase(), False, f)
```

```
    #At the end of each loop, the status is checked
```

```
    if ((0 == (StatusBits.Busy & status)) and (0 == (StatusBits.
Waiting & status))):
```

```
        break
```

This example checks whether the current save format of the Lynx is either LIST (`ListData`) or TLIST (`TlistData`). The regular LIST data can be accessed rather simple, where the TLIST requires a bit more work. The TLIST reconstruction is shown in the section 2.3.3.

## High Voltage

The Lynx has a built in high voltage supply. The polarity and all other available options are selectable via the corresponding code

```
ParameterCode.Input_VoltagePolarity
```

To turn on the high voltage:

```
lynx.setParameter(ParameterCodes.Input_VoltageStatus, True, input)
```

is needed. This shows an inherent problem with the Lynx. The voltage can just be turned on rapidly, which for most detectors can be problematic. The Lynx itself does not offer any possibility to ramp up the voltage automatically. An example for setting the voltage safely:

```
while (voltage < 3000 ):
    lynx.setParameter(ParameterCodes.Input_Voltage, voltage, input)
    voltage = voltage + 50
    #Sleeps for 50 seconds
    time.sleep(50)
```

A script with this basic functionality should be used for turning on the high voltage for a detector to prevent it from any harm.



# Declaration

I assure that I created this thesis independently and only used the quoted sources and tools.

Ich versichere, dass ich diese Arbeit selbstständig verfasst und keine anderen als die angegebenen Quellen und Hilfsmittel benutzt habe.

Heidelberg, 1. September 2017